CrossMark

THE BLACK HOLE–BULGE MASS RELATION IN MEGAMASER HOST GALAXIES[*]

Ronald Läsker[1,2], Jenny E. Greene[3], Anil Seth[4], Glenn van de Ven[1], James A. Braatz[5], Christian Henkel[6,7], and K. Y. Lo[5]

[1] Max-Planck Institut für Astronomie, Königstuhl 17, D-69117, Heidelberg, Germany; laesker@mpia.de
[2] Finnish Centre for Astronomy with ESO (FINCA), University of Turku, Väisäläntie 20, FI-21500 Kaarina, Finland
[3] Department of Astrophysical Sciences, Princeton University, 4 Ivy Lane, Peyton Hall, Princeton, NJ 08544, USA
[4] Department of Physics & Astronomy, University of Utah, 201 James Fletcher Building, 115 South 1400 East, Salt Lake City, UT 84112, USA
[5] National Radio Astronomy Observatory, 520 Edgemont Road, Charlottesville, VA 22903, USA
[6] Max-Planck-Institut für Radioastronomie, Auf dem Hügel 69, D-31212 Bonn, Germany
[7] Astron. Dept., King Abdulaziz University, P.O. Box 80203, Jeddah 21589, Saudi Arabia

ABSTRACT

We present *Hubble Space Telescope* (*HST*) images for nine megamaser disk galaxies with the primary goal of studying photometric BH-galaxy scaling relations. The megamaser disks provide the highest-precision extragalactic BH mass measurements, while our high-resolution *HST* imaging affords us the opportunity to decompose the complex nuclei of their late-type hosts in detail. Based on the morphologies and shapes of the galaxy nuclei, we argue that most of these galaxies' central regions contain secularly evolving components (pseudo-bulges), and in many cases we photometrically identify co-existing "classical" bulge components as well. Using these decompositions, we draw the following conclusions. (1) The megamaser BH masses span two orders of magnitude (10^6–$10^8\,M_\odot$) while the stellar mass of their spiral host galaxies are all $\sim 10^{11}\,M_\odot$ within a factor of three. (2) The BH masses at a given bulge mass or total stellar mass in the megamaser host spiral galaxies tend to be lower than expected when compared to an extrapolation of the BH-bulge relation based on early-type galaxies. (3) The observed large intrinsic scatter of BH masses in the megamaser host galaxies raises the question of whether scaling relations exist in spiral galaxies.

Key words: galaxies: bulges – galaxies: photometry – galaxies: structure – methods: observational – techniques: photometric

1. INTRODUCTION

Supermassive black holes (BHs) play a special role in galaxy evolution. They are a ubiquitous component of massive galaxies (e.g., Kormendy & Ho 2013) and appear to comprise approximately a fixed fraction of the mass of the spheroidal component of the galaxy (e.g., McConnell & Ma 2013). Motivated by these scaling relations, theory invokes energy injection from actively accreting BHs to self-regulate BH growth (Debuhr et al. 2010), truncate star formation in massive galaxies (e.g., Silk & Rees 1998; Springel et al. 2005), and keep gas in clusters from cooling (e.g., Fabian 2012).

However, our understanding of BH demographics is far from complete. In particular, while we now have dynamical BH mass measurements for more than 50 galaxies, these galaxies convey a biased view of the galaxy population. They are skewed toward dense elliptical galaxies (van den Bosch et al. 2015). They are also biased toward massive systems, with a few exceptions (e.g., Seth et al. 2010, 2014). Spiral galaxies are particularly challenging; due to both the typically low BH masses and the presence of dust, star formation, and non-axisymmetric components (e.g., bars), stellar and gas dynamical modeling is far more challenging. These limitations hinder our ability to diagnose the underlying physical mechanisms driving the scaling relations.

There is one method that delivers high-precision, high-accuracy dynamical BH masses in spiral galaxy nuclei: fitting

the rotation curves of megamaser disks (e.g., Herrnstein et al. 2005; Kuo et al. 2011). In these special systems, we observe extremely luminous 22 GHz H_2O masers in an edge-on accretion disk on ~ 0.5 pc scales from a weakly accreting supermassive BH (see review by Lo 2005). The precision of the BH mass measurement is actually limited by our knowledge of the galaxy distances. As first demonstrated with the proto-typical megamaser disk galaxy NGC 4258 (Herrnstein et al. 1999), it is also possible to measure a geometric distance using very-long-baseline observations (VLBI) in combination with single-dish monitoring of the acceleration of the systemic megamasers in the disk. These geometric distance measurements are the primary goal of the Megamaser Cosmology Project (MCP; Reid et al. 2009; Braatz et al. 2010, and associated follow-up publications). Thus far, five galaxies have direct distance measurements (NGC 4258, NGC 5765b, NGC 6264, NGC 6323, and UGC 3789 in Herrnstein et al. 1999; Kuo et al. 2013, 2015; Reid et al. 2013; Gao et al. 2015). At least nine galaxies have reliable megamaser-based BH mass measurements: NGC 1194, NGC 2273, NGC 2960, NGC 4388, NGC 6264, and NGC 6323 (Kuo et al. 2011), as well as NGC 3993 (Kondratko et al. 2008), NGC 4258 (e.g., Miyoshi et al. 1995; Herrnstein et al. 2005; Humphreys et al. 2013), and UGC 3789 (Reid et al. 2009; Kuo et al. 2011).

The megamaser disk galaxies allow us to peer through the gas, dust, and star formation to directly measure BH masses in spiral galaxy nuclei as well as to get a handle on secular BH fueling mechanisms (Greene et al. 2013, 2014). In previous work, we studied the relationship between galaxy velocity dispersion σ^* and BH mass in megamaser disk galaxies (Greene et al. 2010). Here, we tackle the relationship between

---

Table 1
The Megamaser Sample

Galaxy	R.A.	decl.	D (Mpc)	Hubble Type	L_H ($10^{10} L_{\odot,H}$)	R_e (kpc)	t_{exp} (s)	Obs. Date	Wide-field Imaging
(1)	(2)	(3)	(4)	(5)	(6)	(7)	(8)	(9)	(10)
IC 2560	10:16:18.7	−33:33:50	41.8	(R)SB(r)b	13.2	4.0	422	2010 Oct 23	UVIS F814W, LCO DuPont/Tek-I
NGC 1194	03:03:49.1	−01:06:13	52.0	SA0+	5.75	2.8	422	2011 Nov 23	APO3.5 m/NIC-K
NGC 2273	06:50:08.6	+60:50:45	26.0	SB(r)a:	3.47	1.4	422	2011 Jan 31	APO3.5 m/NIC-K
NGC 2960	09:40:36.4	+03:34:37	71.0	Sa?	7.76	1.9	422	2011 Jun 14	APO3.5 m/NIC-K
NGC 3393	10:48:23.4	−25:09:43	53.6	(R)SB(rs)	9.33	2.5	422	2011 Nov 11	UVIS F814W
NGC 4388	12:25:46.7	−12:39:44	19.0	SA(s)b:	3.09	1.4	422	2011 Jun 08	APO3.5 m/NIC-K
NGC 6264	16:57:16.1	−27:50:59	136.0	S?	8.71	4.0	422	2011 Jul 30	APO3.5 m/NIC-K
NGC 6323	17:13:18.1	−43:46:57	105.0	Sab	8.71	2.5	422	2011 Sep 01	WIYN/WHIRC-K
UGC 03789	07:19:30.9	−59:21:18	50.0	(R)SA(r)ab	5.37	2.2	422	2011 Sep 06	APO3.5 m/NIC-K

Note. Columns (1)–(5) give the galaxy name, coordinates, distance in Mpc, and Hubble Type (RC3 catalog, de Vaucouleurs et al. 1991). Column (6) gives the galaxy (total) H-band luminosity in units of $10^{10} L_{\odot,H}$, and column (7) the galaxy effective radius in kiloparsecs. Both the L_H and R_e values result from our imaging data and multi-component fitting. The inner parts are imaged with HST/WFC3 in the F160W filter, with exposure times in seconds, and the dates are given in columns (8) and (9). In order to place constraints on the outer parts of the surface brightness that did not fit on the WFC3-IR FOV of $70\rlap{.}''4 \times 62\rlap{.}''6$, we also include data that we obtained on the telescopes and instruments given in column (10).

BH mass and bulge mass in these objects. Although a number of prior works have included bulge luminosities for many of these galaxies (e.g., Greene et al. 2010; Kormendy & Ho 2013; Graham & Scott 2015), in this paper, we demonstrate that there is significant substructure on sub-arcsecond scales, and that disentangling the bulge components from other nuclear components requires the highest possible spatial resolution provided by the HST.

This paper contains many technical sections. In Section 2, we describe the sample, our data sources, and the data processing. In Section 3, we decompose the two-dimensional surface brightness (SB) profiles, and in Section 4 we investigate the nature of the bulge components of the megamaser disk host galaxies. Those interested in the main results can go directly to Section 5 where we discuss the megamaser disks in the BH-galaxy mass plane, and then fit the scaling relations including the new measurements presented here. In Section 6, we summarize and discuss our results. The redshift distances to our targets are based on $H_0 = 70$ km s^{-1} Mpc^{-1}, a value that is consistent with all of the published values of H_0 based on geometric distance determinations of megamaser disk galaxies (see MCP references given above).

2. DATA

2.1. Sample

Our sample of megamaser disk galaxies with BH masses is taken from Greene et al. (2010), with most of the M_{BH} measurements provided by (Kuo et al. 2011, Table 1). We focus on these nine galaxies because they have Keplerian megamaser rotation curves and high-resolution imaging data, and thus well-determined M_{BH}. While the BH mass we adopt for IC 2560 ($10^{6.4\pm0.4} M_\odot$; Kuo et al. 2011) is based on single-dish data, published and preliminary reductions of VLBI data yield log $M_{BH}/M_\odot$ of 6.54 ± 0.06 (Yamauchi et al. 2012) and 6.64 ± 0.03 (J. Wagner et al. 2016, in preparation). If we were to adopt those values, then the results for the BH scaling relations (relation parameter and subsample offsets, see Section 5) would barely change (within a few percent of the uncertainties). Several of our targets are >50 Mpc away, and most of them were previously known or suspected to host

small-scale structures (nuclear rings, disks, or bars) in addition to the bulge. High-resolution imaging is thus essential for a robust analysis. We do not include Circinus, NGC 1068, or NGC 4945 in this work, since comparable high-resolution data are not readily available for them, but we will consider the first two as a secondary sample in Section 5.

2.2. HST Imaging

The high-resolution *Hubble Space Telescope* (*HST*) data (FWHM = $0\rlap{.}''15$ in the H band corresponding to 50 pc at the median sample distance of 70 Mpc) were taken between 2010 October and 2011 November (see Table 1). We obtained *HST*/WFC3-IR imaging with filters F110W and F160W (similar to the 2MASS J and H bands) for each galaxy. Within the same program, we also acquired WFC-UVIS exposures in the F336W, F438W, and F814W filters (roughly the U, B, and I bands). We base our bulge luminosities and derived masses on the H-band data in order to reduce the uncertainties associated with dust obscuration and variations in stellar population, as compared to the optical bands. Indeed, many of the late-type galaxies in our sample are quite dusty and have complicated color profiles. We use the color information contained in the UVIS bands for a refined luminosity–mass conversion.

All of our galaxies were imaged in four exposures with F160W using sub-pixel dithering and a total exposure time of 422 s. They were co-added and cleaned of cosmic rays using the PyFits MultiDrizzle pipeline.[8] In order to fit our five-band observations into two orbits, we utilize sub-arrays to avoid buffer dumps. The field of view (FOV) of the subarray is 70×62 arcsec, which is filled by the target in all cases. MultiDrizzle provides exposure time maps for the combined frame which we use to calculate the noise map needed for model fitting with GALFIT.

2.3. Ground-based K-band Imaging

Since our *HST* data do not cover the outskirts of our target galaxies, we obtained additional wide-field imaging data. Most of these were ground-based K-band images which were acquired

---

[8] PyFits is a product of the Space Telescope Science Institute, which is operated by AURA for NASA.

from 2010 to 2012 on the Apache Point Observatory (APO) and WIYN[9] 3.5 m telescopes, using the NICFPS and WHIRC instruments, respectively (http://nicfps.colorado.edu/; Smee et al. 2011). In two fields (IC 2560 and NGC 3993), sufficiently deep NIR images were not available; here, we used *HST* WFC3 F814W and Las Campanas Observatory (LCO) du Pont 100-inch SITe2K-CCD *I*-band images. For details of the instruments, exposure times, and observing dates, see Table 1. Aside from providing valuable constraints on the derived galaxy parameters, and thus allowing robust fits to the complex morphologies that we encounter, their FOV is also large enough to allow reliable background subtraction, unbiased by galaxy light. In ground-based *K*-band images, these advantages are tempered by a bright ($\sim$14 mag arcsec^{-2}) background that is variable both spatially and temporally. A carefully designed observing strategy and data reduction is therefore required to achieve reliable background subtraction.

In taking the data, we apply a large-scale dither pattern, with the target first imaged near the detector center and then moved toward the corners of the FOV in a clockwise pattern. Before and after every on-target exposure, we perform an off-target exposure, and the whole pattern is repeated several times. This results in $\sim$25 science frames and twice the number of sky frames. With this strategy, we obtain a reliable reconstruction of the background, since every part of the detector remains unoccupied by the relatively large target galaxy at least in a sizeable fraction of the exposures, and we can simultaneously monitor the evolution of the background level and the two-dimensional structure in the background.

Using the dark and twilight flat frames, we identify bad pixels and mask them in all subsequent exposures. After flatfielding the raw frames, a background pattern (see bottom-left panel in Figure 1) persists, as does a much weaker, near-random pattern that corresponds to the expected pattern from variable non-uniform sky (atmospheric) emission. We ascribe the time-invariant portion of the residual background pattern to a discrepancy between the twilight flatfield image and the response of the detector to night sky illumination. Therefore, we need to subtract the mean background pattern that persists after the frames have been flatfielded with the twilight flat. The standard alternative, i.e., dome flatfield images, provides a significantly poorer approximation to the nighttime sky (and flatfield) pattern. Alternatively, we addressed the residual time-invariant background pattern by flatfielding using a "superflat," which is a flatfield image constructed from the images taken over the course of the night. However, we found no improvement in the background subtraction using this method. To achieve the required signal-to-noise ratio (S/N) in the flat requires summing over most of the images over the course of the night, but there is sufficient change in the background pattern with time that residual patterns remain after flatfielding with the "superflat."

We construct an image of the mean residual background pattern as follows. We first normalize each frame by its mean background, and then take a pixel-by-pixel median over all of the normalized frames, including all sky frames and on-target frames when the target covers less then 40% of the FOV. By averaging so many frames, we can remove additional bad pixels and astronomical sources while retaining a high S/N in

the averaged sky image. For the masking of intervening objects, we use source detection by the SEXTRACTOR software, combined with by-hand masks for bright stars and extended objects (galaxies). The mask for measuring the mean must be a combination of the masks of all frames, in order to avoid level offsets caused by large masked objects covering different parts of the detector on an uneven background. We subsequently subtract from each frame this "sky structure" image, scaled by the frame's background level.

This procedure is very effective at removing the residual near-constant background pattern (see Figure 1, bottom right panel). However, it requires that every part of the detector be uncontaminated by celestial sources, which renders the on-target frames unusable in some galaxies. For those fields, the sky pattern can still be reconstructed using the interleaved sky exposures. Naturally, for a successful background subtraction, we also need to measure the average sky level, apart from its spatial structure. For this, we use on-target measurements rather than the pure sky frames because the mean sky level fluctuates by $\sim$1% ($\sim$16–17 mag arcsec^{-2}) even on timescales of a minute or less.

After subtracting the sky structure and level, we coadd our frames. To that end, we re-detect all astronomical sources using SEXTRACTOR, use the resulting source catalogs to compute a third-order polynomial astrometric solution of the field distortion and true pointings (different from the coordinates found in the headers by $\sim$1$''$ on average), and finally re-project and coadd the frames using SWARP.

After this first-pass sky subtraction and co-addition, we have an image that is much deeper than any individual frame, and hence offers a much better opportunity to mask faint sources (stars and small background galaxies) as well as low-level extended "wings" of bright stars and large galaxies. It also allows a better visual identification of large galaxies in the field. In fact, faint but previously unmasked source flux does sometimes leave visible imprints in the sky-subtracted frames which propagate to the first-pass stack. After obtaining the improved masks from the deep first-pass stack, we repeat the above procedure, but this time we use the deep mask projected onto the individual frames. This improves the sky structure model and removes remaining artifacts in the background.

2.4. Combining HST and Ground-based Data

We combine *HST* (*H* band) with ground-based images in order to provide sufficient constraints during the fitting process. We experimented and found that most of the real structures present in our galaxies cannot be analyzed reliably with GALFIT when either the ground-based or *HST* data are taken alone. For the medium-resolution (median FWHM $\sim$ 0$''$.8), ground-based data, the cause is clear: small-scale structures are not resolved and a basic bulge plus disk model is the only feasible model in most cases. However, the *HST* data alone are also insufficient: the lack of data at large scales prevents a convergence of more complex models. In SB profile modeling, the need for large-scale information on both the galaxy light distribution and the background has been discussed in Peng et al. (2010).

We combine each co-added *HST J*- or *H*-band image with ground-based *K*-band data by first scaling the former to the latter: we measure the radial SB profiles in both, and pick by eye the part of the profile in which both overlap and exhibit the same shape. The matched profiles (Figure 2) show that the *J*-and *H*-band profiles are very similar to the *K*-band profiles, except in the very center (active galactic nucleus (AGN) light and dust) and around

---
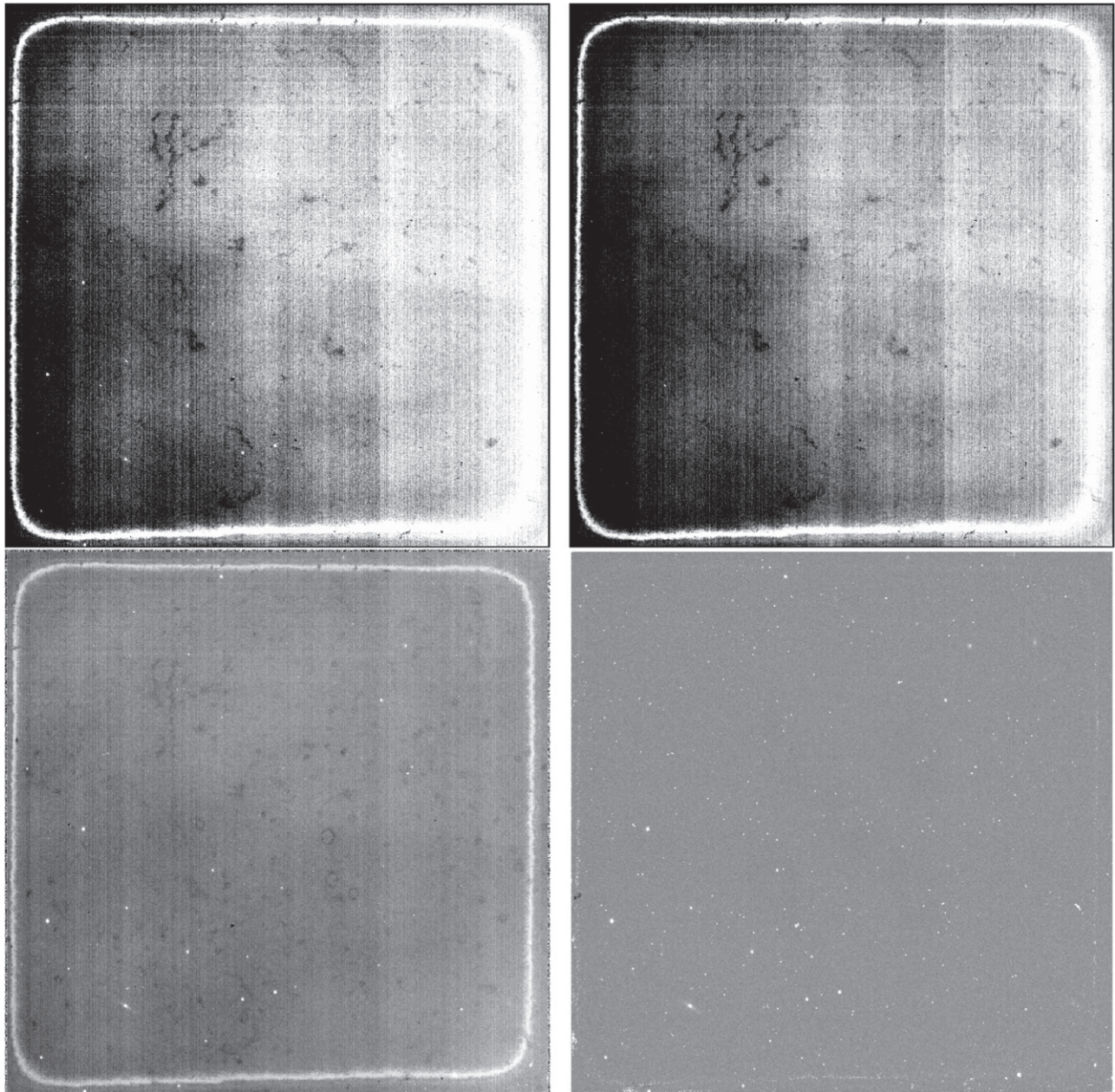
Figure 1. Example demonstrating the need for subtracting the residual common sky pattern after flatfielding, from APO data. Top left: raw exposure. Top right: twilight flatfield stack. The structure remaining after dividing by the flatfield image is evident (bottom left panel), as is the improvement after subtracting the mean sky pattern (the mean of all frames of the OB, after source masking, bottom right). Random temporal sky pattern variation is negligible and not visible at this contrast. The same relative grayscale was used in all panels ($\pm 10\%$ of the mean).

spiral arms (dust and young stellar populations), and the similarity of the profiles justifies our approach. After rescaling and background-subtracting the *HST* images using a linear fit to the profiles, $\langle HST \rangle = \langle \mathrm{bkg} \rangle + \langle \mathrm{scale} \rangle * \langle \mathrm{ground} \rangle$, we resample the ground-based image stack onto the *HST* WCS and replace *K*-band data with *HST* data where they exist. Similarly, we re-project, scale, and replace the noise and weight maps of *K*-band stacks with *HST* data where available.

3. IMAGE FITTING

3.1. Decomposition Philosophy

Although there is considerable interest in the correlations between BH mass and bulge luminosity or mass, there are few

works that examine bulge masses in spiral galaxies with dynamical BH masses (they include Gadotti 2008; Hu 2008; Sani et al. 2011; Kormendy & Ho 2013). Often, spiral galaxies are excluded due to the difficulties in identifying robust bulge parameters (e.g., McConnell & Ma 2013). For one thing, the nuclei of spiral galaxies contain gas, dust, and ongoing or recent star formation (e.g., Carollo et al. 1997). These alone complicate the task considerably, since it is difficult to determine the true bulge parameters or mass-to-light ratio. However, it is even more difficult to determine exactly what bulge means in the context of these galaxies.

All of our galaxies contain a large-scale disk, and all show a steepening of the profile toward the center—a "bulge" by the most general definition. These central light excesses, however,
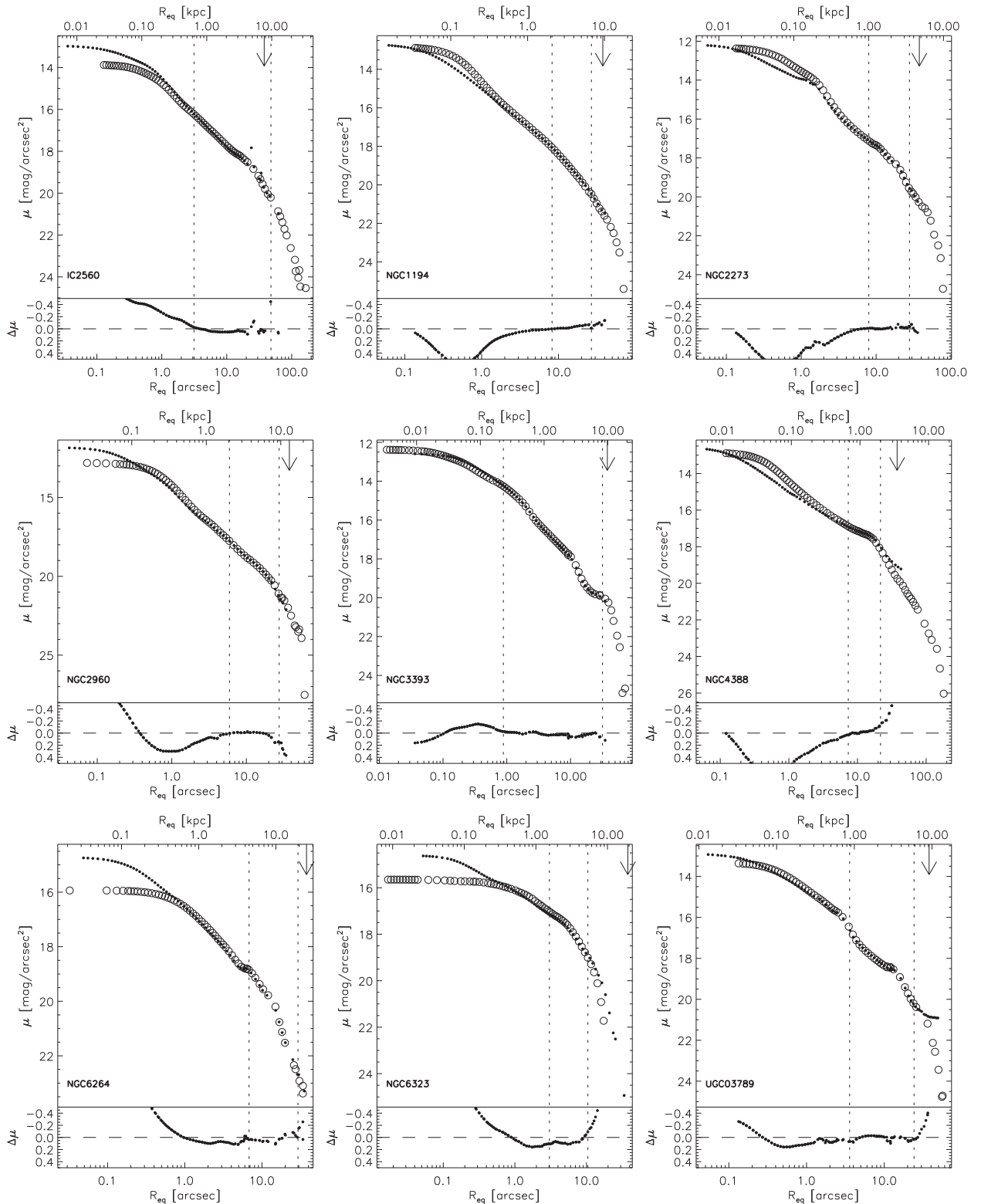
Figure 2. Comparison of wide-field (open circles) and *HST*/WFC3-F160W (filled dots) surface brightness profiles μ, plotted against equivalent circular radius, $R_{eq} = \sqrt{ab}$. The wide-field data are generally deep, ground-based *K*-band images, except in NGC 3393 (*HST*/WFC3-UVIS F814W). In IC 2560, the filled circles show F160W combined with *HST*/WFC3-UVIS F814W data, and open circles show ground-based, LCO-100 *I*-band data. The profiles were matched by a linear fit (*HST* background level and flux scaling) using a radial range chosen to minimize color gradients (dotted vertical lines). The arrow indicates the radius outside of which we replace *HST* with wide-field data. Residuals of *HST* minus wide-field data are plotted in the lower parts of the figures, exposing $H - K$ (or $H - I$) color variations and, in particular, how much better *HST* resolves the nuclear region.

show a wide range of physical properties, which are often more similar to disks than to classical bulges and elliptical galaxies: they are flattened like disks, tend to be fitted by an exponential profile (Andredakis & Sanders 1994) or Sérsic (1963) with low index (generally $n < 2$, see Fisher & Drory 2010), they show bars, dust, or spiral arms as disks do, and they have recent or

ongoing star formation like disks (Carollo et al. 1997, and the review in Kormendy & Kennicutt 2004).

Together, these attributes are interpreted as evidence that the central light excess or bulge region is being built up slowly by secular, gas-rich processes such as bar or spiral arm transport. To distinguish these components from kinematically hot systems without gas or young stars (e.g., elliptical galaxies), these systems have come to be known as "pseudo-bulges," while bulges that have the characteristics of ellipticals are called "classical bulges." Because the classification of a bulge depends on how it formed, it is certainly possible that some late-type galaxies contain both a pseudo- and classical bulge component, with the former having low mass-to-light ratios and thus dominating the light (Nowak et al. 2010; Erwin et al. 2015). Thus, we first decompose these different components (e.g., Weinzirl et al. 2009; Laurikainen et al. 2010; Läsker et al. 2014a), and then ask which are of interest in the context of BH-bulge scaling relations.

We adopt the following dual approach. First, we consider a "basic" model, comprised of only a bulge and a large-scale disk, plus a nuclear point source if it can be included.[10] In the basic fit, the small-scale components are mostly fit by the "bulge" component, and only to a small degree accounted for by the disk component. Therefore, the magnitude of this "basic bulge" represents an approximate upper limit to the true (classical) bulge magnitude.

With a basic model in hand, we construct a more complete model, including structures on small scales, which may help us to isolate a bulge component. We simultaneously model any central bars, rings, or disks, and look for an additional light component that is rounder and more centrally concentrated than the outer disk. If there is one, then we call this the "classical" bulge. In the future, we will improve these decompositions by combining spatially resolved kinematics (e.g., Greene et al. 2014) with our *HST* imaging.

3.2. Fitting

We now describe our two-dimensional parametric modeling in more detail to model the central components in each galaxy.

Working in two dimensions allows us to make full use of the information contained in the data to reduce degeneracy, and is an important advantage over one-dimensional modeling for the complex galaxy structures considered here. Each two-dimensional model component is corrected for the effects of the point-spread function (PSF), and then the parameters of the model are optimized using χ^2 minimization with the publicly available code GALFIT3 (Peng et al. 2010). At minimum (our "basic" model), the models include a bulge, a large-scale disk, and a central point-source model of the AGN and/or an unresolved nuclear star cluster in those cases where the bulge +disk model does not overestimate the central light already. In all of the megamaser host galaxies, more components are present. We identify these based on visual identification in the science image, the residual image of the basic model, and the radial profiles of SB, ellipticity (*e*), and position angle (PA).

An accurate PSF model is an important ingredient in the modeling. We construct a PSF model by combining a number of stars in our images, which gives us a model of the PSF that is local both in space and in time to the observations of the

galaxy. In the Appendix, we describe various PSF comparisons to show that we are accurately recovering the PSF (see Figure 27 in the Appendix). Similarly, the masking of intervening objects, background subtraction, the availability of a sufficiently large image area around the target galaxy, and an appropriate noise image impact the feasibility and accuracy of the fit results. We describe these ancillary data in the Appendix B.

We follow wide-spread convention in prescribing the radial SB profile of Sérsic form for the bulge, as well as an exponential profile for the large-scale disk. The Sérsic profile is defined as

$$I(R) = I_e \exp\{-b_n[(R/R_e)^{1/n} - 1]\},\qquad(1)$$

in terms of three independent parameters: the effective radius R_e along the semimajor axis (SMA), the SB I_e at R_e, and the Sérsic index n. The value of b_n is numerically determined such that the area inside of R_e contains half of the total flux. The large-scale disk is modeled with an exponential profile, which is equivalent to a Sérsic profile with $n \equiv 1$, and the scale radius (R_s) is related to $R_e = b_{n=1}R_s = 1.678R_s$. The two-dimensional SB profile follows from (1) by additionally specifying the center (x_0, y_0), axis ratio $(q = 1 - e)$, and PA of the elliptical isophotes. In GALFIT, I_e is replaced by the total magnitude of the profile, $m_{ser} = m_0 - 2.5\log F_{ser}$, where m_0 is the photometric zeropoint and F_{ser} is the total flux, which is calculated by

$$F_{ser} = 2\pi R_e^2 q I_e n b_n^{-2n} e^{b_n} \Gamma(2n)\qquad(2)$$

with $\Gamma(2n) = \int_0^\infty x^{2n-1}e^{-x}dx$ being the Gamma function.

The full image model is the sum of the fluxes from all of the included components. Apart from the two-dimensional PSF for the AGN, we exclusively employ profiles of Sérsic form, albeit with fixed Sérsic index if an exponential ($n \equiv 1$) or Gaussian ($n \equiv 0.5$) profile is desired. We sometimes use profile modifications, including Fourier modes, truncations, coordinate rotation, and bending modes. For more details on these perturbations, see Peng et al. (2010).

In Table 2, we list a selection of the resulting GALFIT parameters: component magnitudes, sizes (bulge R_e and disk R_s), and the bulge Sérsic index. Total apparent magnitudes are also listed (column 2).

3.3. Detailed Decompositions

It is not trivial to determine the number and type of components to fit to these many-component profiles in the face of possible profile mismatches and parameter degeneracies. We generally begin with a very simple two-component model, and then examine the fit residuals, the ellipticity, and the PA profile to see whether additional components are warranted. We also refit, adding components in a different order, to be sure that GALFIT robustly converges on the same fit. The most challenging task is to find the most probable and physically realistic model while retaining acceptable alternatives for the systematic uncertainty estimate. Compared to this systematic (modeling) uncertainty, the formal parameter uncertainties from the χ^2 derivatives are very small.

In the following subsections, we describe the most common subcomponents and how we identify them. Each is demonstrated graphically in Figure 3.

---

[10] That is, if the bulge+disk model (without the point source) does not already overestimate the central surface brightness.

Table 2
GALFIT Best-fit Parameters of Galaxy Image Models

Galaxy	Total		Bulge						Disk				Psf		Additional Components
	m_t		m_b		R_e ["]		n		m_d		R_s ["]		m_p		mag and Type
	(2)		(3)		(4)		(5)		(6)		(7)		(8)		(9)
	bas	bul	bas	bul	bas	bul	bas	bul	bas	bul	bas	bul	bas	bul	
IC 2560	8.83	8.62	10.71	11.50	0.99	0.59	2.9	1.5	9.04	9.65	6.2	5.6	⋯	16.33	13.44, 11.77, 11.72, 9.57 ND, XBul, SpRing, Env
NGC 1194	9.90	10.01	10.22	12.04	4.6	1.8	6.8	3.2	11.39	13.50	3.5	6.9	⋯	17.30	12.75, 10.32 Bar, Env
NGC 2273	9.13	9.04	10.96	10.81	0.25	0.33	1.0	2.0	9.36	9.75	1.4	2.2	14.84	15.24	12.85, 11.30, 11.31 NR, Bar, Spir
NGC 2960	10.36	10.35	11.24	11.01	0.68	15.8	4.0	1.0	12.02	10.89	3.1	2.1	⋯	14.84	12.44 ND
NGC 3393	9.46	9.55	10.19	11.20	1.6	0.62	3.5	2.3	10.24	10.77	5.5	1.6	17.63	15.94	13.65, 13.01, 10.57 Bar, SpRing, Env
NGC 4388	8.59	8.49	10.57	10.28	0.9	1.2	3.8	2.2	8.79	9.72	2.4	1.7	14.78	14.80	13.00, 10.43, 9.80 ND, SpRing, Env
NGC 6264	11.64	11.64	12.97	14.44	3.2	0.65	3.1	1.3	12.02	12.67	5.6	5.1	18.48	18.04	13.59, 12.72 Bar, SpRing
NGC 6323	11.08	11.08	14.05	14.14	0.75	0.66	1.2	1.1	11.16	11.82	4.2	3.4	17.45	17.40	13.05, 12.49 Ring, Spir
UGC 03789	9.98	10.00	11.47	11.50	0.51	0.8	1.5	3.3	10.31	11.07	3.1	2.3	15.89	16.63	13.25, 13.66, 12.58, 11.76 Bar, NR, Ring, Env

Note. In columns (2)–(8), we list H-band galaxy total magnitude, bulge magnitude, effective radius and Sérsic index, disk magnitude and scale radius, and the magnitude of the central point source. Each of those columns contains two values: the first one ("bas") derived from the basic decomposition (bulge, disk, and the central point source if it could be fitted), followed by the results of the full model ("bul"), which includes significant additional components and yields our best estimate of the "classical" bulge parameters by virtue of separating the non-bulge and pseudobulge components. The additional components' magnitudes of the full model are given in column (9), along with their morphology in abbreviated form: "NR" for nuclear ring, "ND" for nuclear disk, "IDisk" for inner disk, "XBul" for X-shaped/boxy bulge, "Bar," "Ring" for medium-large-scale ring, "Spir" for spiral modified by rotation, "SpRing" for spiral arms that nearly form a ring (no coordinate rotation fitted), and "Env" for envelope. See Table 3 for a short, and Section 3.3 for a detailed, presentation of those morphologies and classification criteria.

Table 3
Morphological Types of Non-standard Components

Abbreviation	Type	Description and Criteria
NR	nuclear ring	ring (see below) of ≲500 pc size, similar to nuclear disk with inner truncation
ND	nuclear disk	$R_e \lesssim 500$ pc Sérsic profile with $n \lesssim 1$, often not aligned with galaxy major axis
IDisk	inner disk	flattened as the main disk but smaller (~1 kpc); only in NGC 2960 where it exhibits spiral arm substructure
XBul	X-shaped/boxy bulge	Sérsic with $1 \lesssim n \lesssim 2$, $q \approx q_{disk}$ and $R_e \sim 1$ kpc; identified in IC 2560
Bar	bar	Sérsic $n < 1$, generally elongated and often misaligned from major axis, in NGC 1194 probably seen down its long axis
Ring	ring	Sérsic with inner truncation and $n = 0.5$, fixed intermediate and large ≳1 kpc scales
SpRing	spiral/ring	shows up in the profile as a ring but also spiral structure (tight winding) in the image, n fixed to 0.5 or 1.0
Spir	spiral	Sérsic profile with coordinate rotation to emulate spiral arms, sometimes fixed $n = 0.5$ or $n = 1$
Env	envelope	extended disk and/or a halo depending on ellipticity ϵ, accounts for flux excess above the main disk at large radii (≳5 kpc), Sérsic n either fixed or free

Note. We list here the abbreviations and morphologies of non-standard (beyond bulge, disk and PSF) components we used while fitting GALFIT models to our galaxy images. Detailed descriptions of the morphological types, and the criteria we used to identify/classify them, are presented in Section 3.3.

3.3.1. Nuclear Disks

Nuclear disks have a scale of ≲100 pc. They are intrinsically flattened, which is evident when they are observed nearly edge-on, and may be misaligned with the large-scale disk (e.g., NGC 4388). There is kinematic evidence for a nuclear disk that we also recognize photometrically in the case of both NGC 2273 (e.g., Barbosa et al. 2006) and NGC 4388 (Greene et al. 2014). Even when seen nearly face on, nuclear disks are distinguished by their relatively sharp boundaries and occasionally inset spiral arms (e.g., IC 2560). Since they occur in the central regions of the galaxy and have high SB, they tend to bias larger-scale components to higher n and smaller size if not modeled separately. We model nuclear disks using a Sérsic profile, typically with $n \leqslant 1$. These disks are sometimes delineated by star-forming regions arranged in a ring (NGC 2273, UGC 3789) and we model them accordingly (see Section 3.3.3). We include a nuclear disk or ring in five of the nine target galaxies (IC 2560, Figure 9; NGC 2273, Figure 13; NGC 2960, Figure 15; NGC 4388, Figure 19; UGC 3789, Figure 25).

3.3.2. Bars

A bar is present in the images of NGC 2273 (Figure 14), NGC 3393 (Figure 18), and UGC 3789 (Figure 26). The classic signatures of a bar are a simultaneous increase in ellipticity and flat PA over the radial range where the bar dominates over the light (e.g., Menéndez-Delmestre et al. 2007), followed by a sharp drop in ellipticity at the outer radius where the bar ends. In certain cases, if the galaxy is at high inclination or the bar is
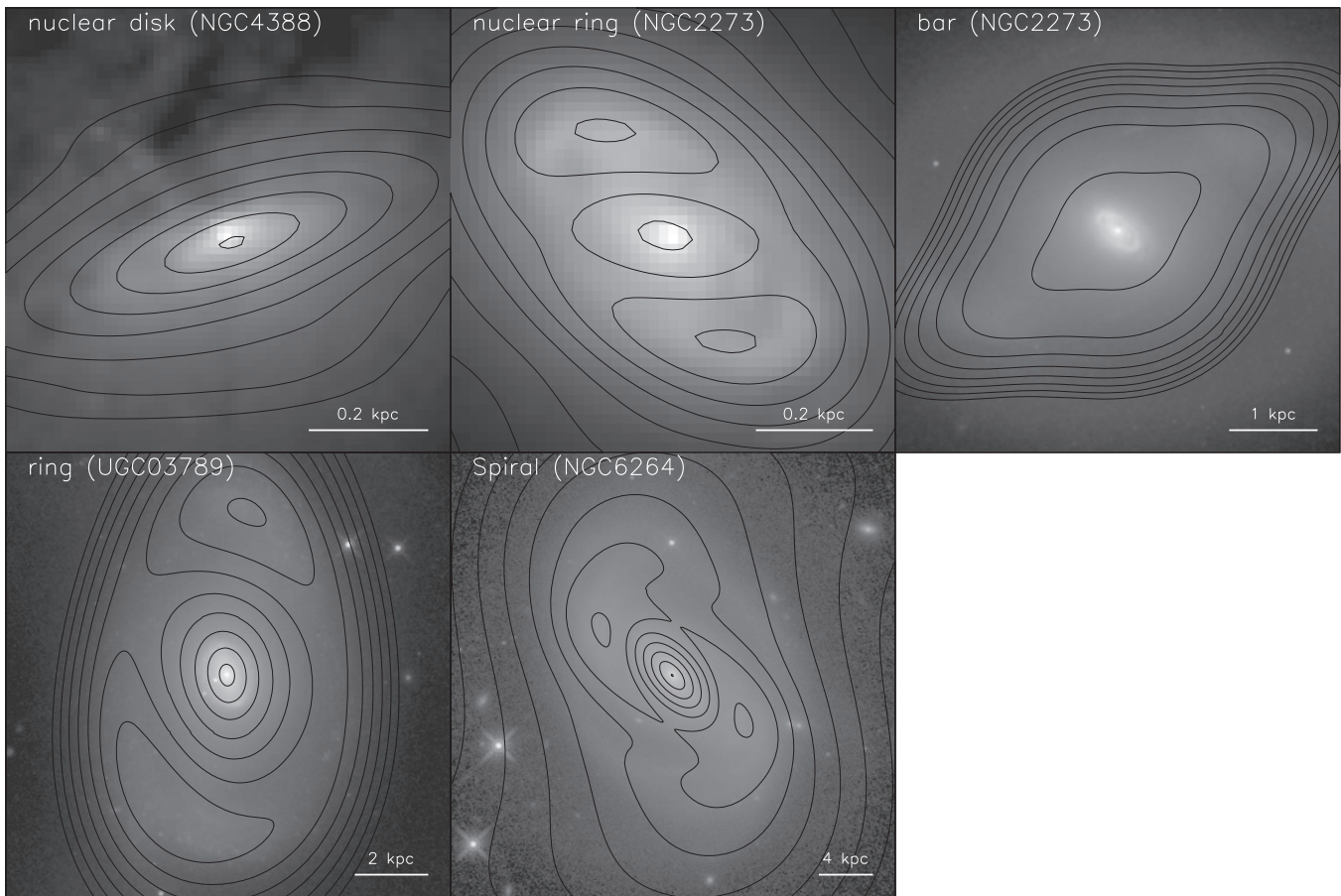
Figure 3. Examples of observed and GALFIT-modeled morphological components in our sample. Shown are *HST*/WFP3-F160W image cutouts with the contours of their model counterparts overlaid. For detailed descriptions of the component types and the fitting process, see Section 3.3 and the Appendix. The offset of the model contours with respect to the brightest point in the image seen in the small-scale nuclear disk and nuclear ring examples is a result of constraining all of the model component center coordinates, except those of the central point source, to a common value during the fit.

pointing toward us, then it is more challenging to uncover, yielding an ambiguity in the final decomposition (see, for instance, NGC 1194, Figure 11). Nuclear bars, similar to nuclear disks or rings, in particular can bias the light profile of any underlying classical bulge component. Because bars form only in disk structures, we exclude them from any classical bulge estimate.

We model all bars as a Sérsic profile with free n, and find them all to have $n \lesssim 1$ as expected. GALFIT offers the (modified) Ferrer profile, which becomes zero outside of the truncation radius and is an alternative profile suited for bars due to its flat center and steep outer profile (Peng et al. 2010). It does not provide an improvement to the fit over Sérsic profiles in our data. We do allow a fourth-order Fourier mode to fit the boxiness of the isophotes of the bar.

3.3.3. Rings

A ring is prominent in NGC 3393 (Figure 17) and NGC 6323 (Figure 23). Three rings are present in NGC 2273 (see Figure 13, and Erwin & Sparke 2003) and UGC 3789 (Figure 25). The inner rings in each galaxy are associated with a nuclear disk (see Section 3.3.1). In NGC 2273, we refrain from modeling the outermost ring due to its low SB. Nuclear rings generally bias the parameters for other nuclear components (e.g., bars and bulges) to fainter and more compact (lower n) profiles if not accounted for (UGC 3789 is an

example). At larger scales, omitting rings (or spiral arms) usually biases the disk to higher flux or larger R_s. We generally model rings as an inner truncation multiplied by a Sérsic profile with fixed $n = 0.5$ (a Gaussian profile). The compactness of this profile is suitable to model the steep decline of the profile. We also test using an exponential profile ($n = 1$), but find that it does not improve the fit. Finally, we never fit a nuclear disk and nuclear ring component simultaneously, as they are degenerate.

3.3.4. Spiral Arms

We detect and fit spiral arms in six out of our nine targets. Spiral arms can be modeled in GALFIT using coordinate rotation, which changes the PA as a function of radius. Fitting spiral arms is not merely a cosmetic measure, but also impacts the best-fit parameters of the large-scale disk. Spiral arms often span a limited radial range in the disk, and thus we use an inner truncation to limit their profile toward small radii. In four cases (IC 2560, Figure 9; NGC 2273, Figure 13; NGC 3393, Figure 17; and NGC 4388, Figure 19), the arms are tightly wound or partially dust obscured. These prove difficult to model with a free-parameter rotation function, and so we model them as a ring. This leaves only two galaxies (NGC 6264, Figure 21; NGC 6323, Figure 23) where we used a rotation function for the spiral component. The remaining three galaxies have no significant spiral structure that could impact our fits. The Sérsic index of the arm model is fixed during the fit due to

degeneracy with the parameters of the required inner trunca-
tion. We tested values of $n = 0.5$, 1.0, and 1.5, and pick the
value that leads to the smallest residuals.

3.3.5. Envelopes

Some of our targets (IC 2560, Figure 9; NGC 1194,
Figure 11; NGC 4388, Figure 19; and UGC 3789, Figure 25)
show a profile extension above the large-scale disk that sets in
at $\gtrsim 5$ kpc scales (see Figure 1). These envelopes are
identifiable visually on the image and are accompanied by a
change in axis ratio $q = b/a$ coincident with a break in the SB
profile, as seen in so-called type III upbending or anti-truncated
disks (e.g., Erwin et al. 2005, 2008; Pohlen & Trujillo 2006).
They are sometimes rounder than the disk, like an outer halo,
but are often flattened and best fit by an exponential profile.
Inclusion of the envelope typically impacts the bulge
parameters only weakly due to the large difference in scale.
However, it may significantly contribute to the total galaxy
magnitude (IC 2560, NGC 4388).

3.4. Systematic Uncertainties

The uncertainty in our fitting is dominated not by
measurement error, but rather by systematic uncertainty. In
general, degeneracy or deficiency in our modeling dominates
the uncertainty, but the background level can also play a
significant role in some cases (e.g., NGC 4388).

3.4.1. Modeling Uncertainty

In the previous subsection and the Appendix, we describe
our general approach to finding the most suitable model for a
given galaxy image. Even given the high spatial resolution and
depth of our data, and the complexity of our models, the true
structure of the galaxy may not be fully represented. Thus, our
choice of number of components and boundary conditions
leaves a systematic uncertainty in the parameters we are
interested in. This systematic parameter uncertainty originating
in the choice of model is separate from the random
uncertainties that originate in pixel noise. The latter are directly
provided by GALFIT and are completely subdominant to the
systematic modeling uncertainties.[11]

We adopt a pragmatic approach and employ a handful
(usually 2–4) of alternative models to our chosen best-fit model
that we consider acceptable. This way, we obtain several
alternative values for the resulting bulge parameter of interest
(chiefly the magnitude) and take their standard deviation as a
systematic uncertainty estimate. These values are presented in
Table 4. Typical systematic uncertainty estimates are a few
tenths of a magnitude. We use these uncertainties with the other
systematic uncertainties added in quadrature to represent the
measurement error in the derived bulge mass (L_{bul} and M_{bul})
when investigating the $M_{BH}-M_{bul}$ scaling relation in Section 5.

3.4.2. PSF Uncertainty

We use a PSF image that is the weighted average of 14
individual star cutouts, as we find them on the model-
subtracted WFC3/IR F160W images. Using this averaged
image instead of any particular (fixed) individual star cutout
reduces random noise, finite sampling, and centering errors, as

---

[11] That is, by one to several orders of magnitude.

well as (correlated) background residuals which propagate to
model parameter errors. We estimate the PSF-related uncer-
tainty of any parameter p when fitted by a single PSF image to
be $\sigma_{p,\mathrm{PSF}}^{(i)} = \sqrt{\frac{1}{N-1}\sum_{i=1}^{N}(p_i - \bar{p})^2}$, where p_i is the fit result
when using the ith of N available individual PSF images. Then,
the uncertainty in p when fitting with the combined PSF image
is approximately $\sigma_{p,\mathrm{PSF}} = \frac{1}{\sqrt{N}}\sigma_{p,\mathrm{PSF}}^{(i)}$, which is akin to the
uncertainty of individual measurements propagated to the
uncertainty of the mean of measurements.

3.4.3. Background Uncertainty

The background uncertainties in our combined *HST*
+ground-based images largely stem from the matching of the
HST data to the ground-based data. In the former, the sky is not
well known because the galaxy fills the field of view. In
contrast, the ground-based images have a wide FOV and a
well-defined background.

Due to color gradients across the galaxy, the fitting of the
sky offset and relative flux scaling of the *HST* data generally
depends on the radial range of the SB profile chosen to
constrain the fit. We chose the fiducial range to minimize the
color gradients, but even in the optimal range, fluctuations from
measurement noise or actual variations within the profile add
uncertainty in the fitted sky offset and relative flux scaling. In
order to estimate the resulting uncertainty to the sky offset of
the *HST* data, we employ a "Jackknife" resampling method. In
each realization, one of the N SB measurements within the
fiducial range is omitted, which results in N sample realizations
of the fitted offset, a_i. Then, the uncertainty in the *HST* sky
level a is $\sigma_a = \sqrt{\frac{N-1}{N}\sum_{i=1}^{N}(a_i - \bar{a})}$. These background
errors are listed in Table 4 in columns labeled "rsc."

3.5. Colors and Conversion to Stellar Mass

In order to facilitate direct comparison with early-type
galaxies, we attempt to mitigate the variability in the mass-to-
light ratio $\Upsilon \equiv M_\star/L$ by using the galaxy color. Since the
variation in Υ with population properties and dust column
density is decreased at NIR wavelengths, we choose F160W
(nearly H band) to measure the luminosity, and derive
$\Upsilon_H \equiv M_\star/L_H$ based on optical colors. We use the color–Υ
relation from Bell et al. (2003), which determines conversions
between a single galaxy color and the galaxy Υ based on stellar
population synthesis models and an assumed dust model. We
also experimented with the two-color relations from Zibetti
et al. (2009), but found that these conversions yielded
unrealistically low Υ values for some of the most massive
ellipticals in our comparison sample, for whom the color is
very red (Section 3.6). We note that many systematic
uncertainties remain in stellar population synthesis modeling,
particularly regarding the contribution to the near-infrared light
from asymptotic giant branch stars (e.g., Maraston 2005;
Conroy et al. 2009; Kriek et al. 2010; Zibetti et al. 2013). It is
possible that the Bell et al. (2003) mass-to-light ratios are
overestimates for the blue $g - i$ color because their models do
not treat these later stages of stellar evolution (e.g., Roediger &
Courteau 2015).

Since we have measured the F435W (roughly B-band) and
F814W (roughly I-band) magnitudes, we are closest in color to
the $g - i$ conversions to Υ_H from Bell et al. (2003). We derive a

Table 4
Systematic Uncertainties

| Galaxy | Bulge | | | | | | | | Disk | | PSF | |
| | m_b | | | | $\log(R_e/\,\mathrm{kpc})$ | | $\log n$ | | m_d | | m_p | |
	psf	rsc	mod	tot	mod	tot	mod	tot	mod	tot	mod	tot
IC 2560	0.00	0.02	0.30	0.30	0.10	0.10	0.17	0.18	0.75	0.75	0.13	0.17
NGC 1194	0.06	0.08	0.54	0.54	0.40	0.42	0.11	0.11	0.19	0.45	8.37	8.37
NGC 2273	0.00	0.04	0.34	0.34	0.19	0.19	0.16	0.17	0.14	0.30	0.39	0.40
NGC 2960	0.11	0.02	0.08	0.14	0.06	0.08	0.14	0.17	0.02	0.05	0.29	0.31
NGC 3393	0.00	0.06	0.11	0.13	0.10	0.12	0.13	0.16	1.07	1.07	0.23	0.28
NGC 4388	0.00	0.31	0.51	0.60	0.11	0.32	0.06	0.24	0.45	0.79	0.12	0.19
NGC 6264	0.02	0.43	0.93	1.03	0.35	0.43	0.15	0.16	0.28	0.30	0.17	0.24
NGC 6323	0.01	0.51	0.52	0.73	0.23	0.55	0.21	0.47	0.32	4.02	0.47	0.54
UGC 03789	0.03	0.12	0.41	0.43	0.18	0.23	0.06	0.08	0.21	0.22	0.14	0.20

Note. Systematic uncertainties for five parameters of the full decompositions: the bulge magnitude, logarithmic effective radius, and Sérsic index (m_b, $\log(R_e/\,\mathrm{kpc})$, and $\log n$), as well as the disk magnitude (m_d) and magnitude of the central point source (m_p). Each total ("tot") systematic error is the sum of the errors resulting from PSF model ("psf"), background and flux scaling ("rsc"), and model ("mod") systematic uncertainties, added in quadrature. In general, the modeling uncertainty (number and profiles of the model components, see Section 3.4.1) dominates the total systematic error, which is why PSF- and background/scaling-related errors (Sections 3.4.2 and 3.4.3) are shown only for the most important parameter in our study, m_b.

conversion between the *HST* colors and the Sloan Digital Sky Survey (SDSS; York et al. 2000) $g - i$ system using simple stellar population models from the Padova group (Marigo et al. 2008), including extinction in each band in the A_V range 0–3. A tight linear relation is found (scatter of 0.05 mag) between the $g - i$ and F438W − F814W color of

$$g - i = -0.443 + 0.738\,(\mathrm{F438W} - \mathrm{F814W}). \qquad (3)$$

Note that the F438W, F814W, F160W, and *H*-band magnitudes here are all in the Vega system, while the SDSS magnitudes are given in the AB system (Oke & Gunn 1983; Fukugita et al. 1996).

For both the basic and classical bulges, we measure the bulge color by defining a radial range over which the given component dominates the total flux. By using the same aperture on both bands, we can derive a color without performing full fits to each band. We ensure that PSF and AGN corrections are negligible by imposing a lower limit of $\gtrsim 2$ pix ($0.''26$) on the SMA of the aperture, which corresponds to ~ 50 pc at the typical distance of 50 Mpc. The magnitudes for the entire galaxy (total) are measured from the total *H*-band magnitude within the WFC3-IR sky-subtracted image. We note that a more precise method for determining component colors would involve the simultaneous fitting of images in multiple bands, but this analysis is outside the scope of our study and will be left to future work.

The inferred colors are listed in Table 5, along with the inner and outer radii of the annuli in which bulge colors were measured, both for the basic and classical bulges. Table 6 shows the $\Upsilon_H(g - i)$ that are derived from the Bell et al. (2003) models. The resulting $\log M_\star = \log L_H + \log \Upsilon_H$ are given in Table 7 and used in Section 5 regarding their correlation with M_{BH}.

3.6. Galaxies from the Literature

The primary sample of megamaser disk galaxies that we have fit comprises nine disk galaxies of similar total stellar mass ($\sim 10^{11}\,M_\odot$). We wish to compare the results for our megamaser sample with a larger sample of galaxies spanning a range of masses, morphologies, and M_{BH}. Many works have performed two-dimensional image decomposition of the hosts of galaxies with dynamical BH mass measurements (e.g.,

Marconi & Hunt 2003; Sani et al. 2011; Beifiori et al. 2012; Vika et al. 2012). Here, we rely on the M_{BH}–L_{bul} data of Läsker et al. (2014b, L14 hereafter) because, of all of the available previous work, their image analysis and quality are closest to our current study. We will discuss the comparison with other literature data in Section 6. The Läsker et al. (2014b) sample comprises 35 galaxies of all Hubble types (4 spiral, 11 lenticular, and 20 elliptical galaxies) selected based on the availability of a reliable BH mass at the time the imaging data were taken. As in this paper, L14 provide the total photometry, results based on basic bulge+disk models, and detailed decompositions, all based on homogeneous deep sub-arcse-cond-resolution *K*-band photometry. One of the galaxies in L14, NGC 4258, is the prototypical megamaser disk galaxy. In the following, we will include NGC 4258 in our sample of maser galaxies.

The sample from L14 is not identical to that of Kormendy & Ho (2013, KH13 hereafter). L14 include the gas emission-based M_{BH} measurements of PGC 49940 and Cygnus A, as well as those of NGC 2778, NGC 4261, NGC 6251, and NGC 7052, which were omitted by KH13 due to doubts about their M_{BH} reliability. Conversely, several M_{BH} measurements are included in KH13 that became available after the photometry for L14 was completed.

We again use the Bell et al. (2003) color conversions to calculate the stellar masses of the L14 sample. In this case, we do not have uniform *HST* color imaging for the objects. Instead, we use the SDSS photometry provided by the NASA-SDSS Atlas[12] (NSA hereafter; see, e.g., Blanton et al. 2011). Eighteen of the L14 galaxies have SDSS photometry. For these, we use the NSA single-component Sérsic fits for the optical galaxy magnitudes. We correct for galactic extinction (Schlafly & Finkbeiner 2011, retrieved using the NED[13]) and calculate a $g - i$ color. For those galaxies which are not in the NSA catalog, we use the mean $g - i$ color corresponding to the appropriate Hubble type: 1.17 mag (E), 1.15 mag (S0), and 1.0 mag (S).

---

[12] http://www.nsatlas.org/
[13] http://ned.ipac.caltech.edu/

Table 5
Bulge and Total Colors

Galaxy	$a_1['']$ bul	$a_2['']$ bul	$a_1['']$ bas	$a_2['']$ bas	$F435 - 814W$ bul	$F435 - 814W$ bas	$F435 - 814W$ tot	$F814 - 160W$ bul	$F814 - 160W$ bas	$F814 - 160W$ tot	$g - i$ bul	$g - i$ bas	$g - i$ tot	$i - H$ bul	$i - H$ bas	$i - H$ tot	$H - K$
IC 2560	0.28	5.89	0.28	7.85	2.83	2.79	2.14	1.70	1.67	1.58	1.65	1.62	1.14	2.46	2.42	2.31	0.26
NGC 1194	0.28	9.49	0.28	9.49	2.91	2.92	2.38	1.64	1.65	1.55	1.70	1.71	1.31	2.38	2.40	2.27	0.38
NGC 2273	0.28	5.89	0.28	4.03	2.38	2.25	2.33	1.78	1.80	1.57	1.31	1.22	1.28	2.56	2.58	2.30	0.29
NGC 2960	0.28	1.88	0.28	6.48	2.44	2.28	1.99	1.58	1.62	1.42	1.36	1.24	1.03	2.31	2.36	2.11	0.35
NGC 3393	0.28	3.33	0.28	9.49	2.09	2.21	2.06	1.62	1.59	1.59	1.10	1.19	1.08	2.36	2.32	2.32	0.28
NGC 4388	2.27	5.89	0.28	3.33	1.90	2.29	1.87	1.99	2.30	1.90	0.96	1.25	0.94	2.81	3.19	2.70	0.28
NGC 6264	0.28	1.41	0.28	4.87	2.32	2.49	1.79	1.61	1.62	1.56	1.27	1.39	0.88	2.35	2.36	2.29	0.33
NGC 6323	0.28	1.41	0.28	0.96	2.95	2.91	1.73	1.83	1.91	1.60	1.73	1.70	0.83	2.62	2.71	2.34	0.33
UGC 03789	0.27	4.67	0.28	4.43	2.03	2.01	1.94	1.69	1.67	1.47	1.06	1.04	0.99	2.45	2.42	2.18	0.27

Note. Bulge colors were measured in elliptical annuli bounded by a_1 and a_2 where the respective bulge component dominates, for the classical bulge ("bul") in our detailed decomposition and the Sérsic component in the basic Sérsic +exponential ("bas") decomposition. Meanwhile, total colors ("tot") were measured across the entire WFC3-IR FOV. Colors in the *HST*/WFC3 F435W, F814W, and F160W (similar to Johnson *B*, *I*, and 2MASS *H*) bands were converted to $g - i$ and $i - H$ as described in Section 3.5. The $H - K$ color is taken from the 2MASS catalog and measured within the 20 mag arcsec^{-2} isophote.

Table 6
Bulge and Total Mass-to-light Ratios

Galaxy	$\log \Upsilon_H (g - i)$ bul	$\log \Upsilon_H (g - i)$ bas	$\log \Upsilon_H (g - i)$ tot
IC 2560	0.11	0.10	0.02
NGC 1194	0.12	0.05	0.05
NGC 2273	0.05	0.03	0.04
NGC 2960	0.06	0.04	−0.00
NGC 3393	0.01	0.03	0.01
NGC 4388	−0.01	0.04	−0.02
NGC 6264	0.04	0.06	−0.03
NGC 6323	0.12	0.12	−0.04
UGC 03789	0.00	0.00	−0.01

Note. Logarithmic *H*-band mass-to-light ratios ($\log \Upsilon_H (g - i)$) based on the Bell et al. (2003) prescription. The colors and decompositions on which these are based are listed in Table 5.

The resulting *H*-band mass-to-light ratio $\Upsilon_H (g - i)$ ranges from 0.99 to 1.06, and thus any assumptions made based on color likely have minor effects on the galaxy mass estimates. We calculate L_H from the L14 *K*-band magnitudes assuming the extinction-corrected 20 mag arcsec^{-2} -isophotal $H - K$ color of the 2MASS database. We find good agreement between the masses derived in this manner and the empirical relation of Cappellari (2013), which fit a relation between the dynamical mass and M_K. The dynamical estimates are 0.2 dex higher on average and related to our color-based masses by a correlation with slope 0.9 but with negligible scatter. The higher dynamical masses are consistent with the presence of dark matter within R_e increasing with increasing galaxy mass. Similarly, our color-based masses are consistent with the values given in KH13, which are only 0.06 dex more massive on average with a scatter of only 0.15 dex. The least certain masses are for the spirals where, again, the stellar population modeling harbors the most uncertainties. As one additional sanity check, we consider the five megamaser galaxies in the NSA catalog; deriving a stellar mass for them using the Bell et al. (2003) color relations and L_i, we find agreement at the 0.2 dex level, indicating that our stellar masses are all on the same relative scale.

In Section 5, we also consider three additional late-type galaxies: the Milky Way, Circinus, and NGC 1068 (the megamaser host NGC 4258 is already included in the L14 sample). In the first case, the BH mass is known more precisely than any other (e.g., Ghez et al. 2008; Gillessen et al. 2009) but the bulge mass is quite difficult to determine. In the other two systems, the BH masses are based on megamaser disk modeling, but the fidelity of M_{BH} has been questioned. In the case of NGC 1068, the rotation curve presented by Greenhill et al. (1996) is sub-Keplerian, perhaps because of a massive self-gravitating disk (Lodato & Bertin 2003). Circinus (Greenhill et al. 2003) may have an uncertain inclination (Ferrarese & Ford 2005).

The M_{bul} of the MW is taken from Kormendy & Ho (2013). The bulge magnitudes and masses for Circinus and NGC 1068 are based on the work of Sani et al. (2011). We convert their apparent [3.6 μm] mag to $M_\star$ using their formula (5) in conjunction with σ_v (dynamical mass), or their Equation (6) (empirical $M_\star$–$L_{3.6}$). For NGC 1068, both $M_\star$ values of the bulge are nearly identical; for Circinus, they differ by 0.5 dex, and so we use their mean ($\log M_{bul}/ M_\odot = 10.00$).

4. RESULTS: BULGE CLASSIFICATION

In this section, we investigate the general properties (luminosities, sizes, stellar masses) of the megamaser disk host galaxies. First, we discuss whether or not our galaxies contain pseudo-bulges, and then we attempt to determine whether or not they contain classical bulges. The nature of these components was discussed above in Section 3.1.

4.1. Presence of Pseudobulges

In Section 3, we described in detail the different physical components that are required to fully model the central regions of our megamaser disk galaxies. Because pseudo-bulges are defined by their formation history, and not by their appearance, we are forced to consider what properties might indicate a pseudobulge. Here, we primarily mean that we have identified structural components (nuclear rings or disks, as well as X-shaped/boxy bulges) that are associated with secular evolution. In the past, it has been shown that Sérsic indices $n < 2$ correlate with the presence of pseudo-bulges (e.g., Kormendy & Kennicutt 2004; Fisher & Drory 2010) as well as with low effective surface brightnesses at a given size (Gadotti 2009), and so we will also consider these specific criteria.

Table 7
Luminosities, Masses, and Sizes

Galaxy	$\log(M_{BH}/M_\odot)$		$\log(L_H/L_{\odot,H})$			$(B/T)_L$		$\log(M_\star/M_\odot)$				$(B/T)_{M\star}$		$\log(R_e/\mathrm{kpc})$		
	val	err	bas	bul	tot	bas	bul	bas	bul	err	tot	bas	bul	bas	bul	tot
IC 2560	6.40	0.40	10.29	9.97	11.12	0.18	0.07	10.40	10.08	0.14	11.14	0.22	0.09	−0.14	−0.33	0.60
NGC 1194	7.82	0.05	10.67	9.94	10.76	0.74	0.15	10.72	10.39	0.20	10.81	0.74	0.38	0.58	−0.34	0.44
NGC 2273	6.88	0.05	9.77	9.83	10.54	0.19	0.19	9.82	9.88	0.12	10.58	0.19	0.20	−0.70	−0.56	0.15
NGC 2960	7.05	0.05	10.53	10.63	10.89	0.44	0.55	10.59	10.21	0.22	10.89	0.50	0.21	−0.28	0.73	0.29
NGC 3393	7.49	0.12	10.71	10.30	10.97	0.51	0.21	10.72	10.31	0.05	10.98	0.51	0.21	0.14	−0.21	0.40
NGC 4388	6.93	0.05	9.66	9.78	10.49	0.16	0.19	9.65	9.77	0.22	10.47	0.17	0.20	−0.11	−0.00	0.15
NGC 6264	7.45	0.05	10.41	9.82	10.94	0.30	0.08	10.45	9.86	0.41	10.91	0.35	0.09	0.33	−0.26	0.60
NGC 6323	6.96	0.05	9.75	9.72	10.94	0.06	0.06	9.87	9.84	0.27	10.90	0.09	0.09	−0.20	−0.24	0.40
UGC 03789	7.05	0.05	10.14	10.13	10.73	0.26	0.25	10.14	10.13	0.15	10.72	0.26	0.26	−0.36	-0.12	0.34

Note. BH masses (log M_{BH}/ $M_\odot$) and their errors, bulge and total *H*-band luminosities (log $L_H/L_{\odot,H}$), the ratio of bulge-to-total luminosity [$(B/T)_L$], stellar masses (log $M_\star$/ $M_\odot$), and effective *H*-band radii [log(R_e/ kpc)] of our sample based on our GALFIT models. "Bas" indicates values based on basic bulge+disk(+point-source) models, while "bul" indicates those of the classical bulge parameters based on the full models. Bulge mass errors are based on the combined calibration, point-source, and modeling uncertainties (see Table 4). Luminosities were converted to masses via the color-based $\Upsilon_H(g-i)$ (Bell et al. 2003) with colors measured on our *HST*/ WFC3 F435W, F814W, and F160W images inside the appropriate apertures (bulge-dominated regions, see Section 4.4). The low B/T of the classical bulges conform to the late Hubble types of most of our targets. Alternative values for the log M_{BH} of IC 2560 (6.54 ± 0.06, Yamauchi et al. 2012; and 6.643 ± 0.025, J. Wagner et al. 2016, in preparation) based on VLBI data instead of the single-dish based M_{BH} adopted here have no appreciable effect on the scaling relations (Section 5).

Below, we will go through the classification of each galaxy in detail (Section 4.4). Here, we simply summarize our main finding: all but one of the galaxies show unambiguous signatures of secular evolution. We find sub-kiloparsec disks, bars, or spirals in all galaxies with Hubble Type Sa or later (Table 1). We only identify one case (the lenticular galaxy NGC 1194) where there is no evidence for a pseudobulge. Thus, we are fairly confident that the large majority of these galaxies do contain a pseudobulge component.

As emphasized by Erwin et al. (2015), among others, the presence of pseudobulge components does not preclude the presence of a rounder, older, kinematically hot classical bulge. From the point of view of BH scaling relations, it may well be that this classical bulge component matters most (Nowak et al. 2010). Thus, we have attempted to use our photometric fitting to identify such components. In the next section, we characterize these putative classical bulge components using color, shape, and structural information.

4.2. Bulge Luminosities, Sizes, and Colors

We derive galactic-extinction-corrected luminosities and linear sizes from the apparent magnitudes and sizes presented in Table 2, assuming $M_{\odot,H} = 3.32$. As a reminder, the "basic" bulge is derived from a fit that includes just two or three components: disk, bulge, and central point source where it can be fit. The point source may arise from the contribution of an AGN or be stellar in nature (e.g., NGC 3384; Ravindranath et al. 2001; Graham & Driver 2007). Basic fits are indicated with the subscript "bas" in tables and figures. The "classical" bulge component is the roundest and highest *n* component in the multi-component fit. Classical bulge components are indicated with the subscript "bul" in figures and tables. Finally, the "total" magnitude and size are calculated as the sum of all of the components in our best-fit multi-component model. We list the resulting parameters in Table 7, along with the bulge-to-total ratios (B/T) for the classical and basic bulge measurements.

In general, the basic bulges are both more extended (mean effective radius 0.8 kpc, ranging from 0.2 to 3.8 kpc) and more luminous (0.5–5.1 × $10^{10} L_{\odot,H}$) while the classical bulges, as they comprise only a single component of the galaxy central

region, tend to be smaller (mean effective radius of 0.7 kpc, ranging from 0.3 to 5.4 kpc) and slightly fainter (0.5–4.3 × $10^{10} L_{\odot,H}$). Likewise, the median B/T drops slightly from the basic bulge (30%) to the classical bulge (20%). Generally, these B/T values are completely consistent with our expectations for early-type spirals (e.g., Simien & de Vaucouleurs 1986; Laurikainen et al. 2010).
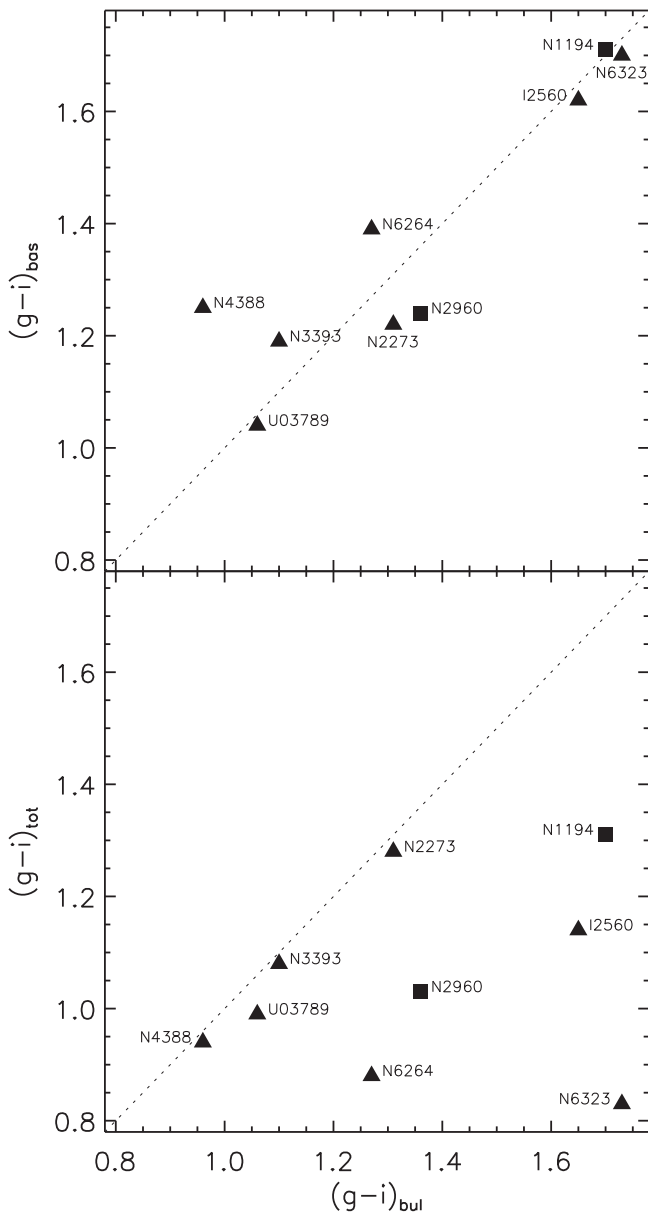
The $g - i$ colors of the bulge and total galaxy are compared in Figure 4. As expected, the total color is always bluer than the bulge color, which avoids light from the large-scale disk component. We also check whether our detailed decompositions result in redder bulges than the basic decompositions. The latter tend to include central disks and rings, which are presumably younger and bluer. With our aperture measurements, however, classical bulges are not appreciably redder than the basic bulges. This similarity suggests that any color differences are too subtle for our crude method to discern, or that dust obscuration offsets real differences in the population.

4.3. Bulge Shapes and Profiles

As discussed in Section 3, we model a putative classical bulge component in addition to the exponential kiloparsec-scale disk and any other identifiable morphological components, such as bars and nuclear disks. We attempt to understand the nature of the putative classical bulge components by examining their intrinsic flattening, Sérsic indices, and photometric scaling relations. Recall that in figures and tables, the classical bulge component is denoted as "bul."

4.3.1. Flattening

As one determining factor, we consider the flattening of the classical bulge component. A true classical bulge should be rounder than the disk. In contrast, if the light is dominated by a disky component, then we expect to see a wide distribution of flattening $q = b/a$. The q of the disk and pseudobulge component should be similar, since secular evolution is supposed to bring material into the bulge from the disk. In practice, all of our classical bulge candidates have a higher projected axis ratio than the main disk with the difference in bulge-disk q ranging from 0.2 to 0.5.

Figure 4. Comparison of the $g - i$ color of the basic bulge ("bas"; top panel) and total galaxy ("tot"; bottom panel) with the classical bulge ("bul"; full decomposition) for our megamaser sample, as drawn from Table 5. S0 galaxies are indicated with squares while spiral galaxies are triangles. All colors are measured in (annular) apertures: the region where the respective bulge component dominates in the GALFIT model, while total color is measured within the HST/WFC3-IR field of view. The colors of basic and classical bulge differ only marginally, but all bulge colors are redder than the total color, as expected.

4.3.2. Sérsic n and the n–L Relation

The basic bulges are best fit by Sérsic indices ranging from 1.0 to 6.8 (Table 2). The presence of compact, disk-like central components (e.g., rings, disks, or bars) tends to drive up the value of n for the basic bulge components. When we perform more detailed decompositions, the effect of the nuclear components is mitigated, which generally leads to lower n. For example, in the galaxy NGC 4388, n drops from 3.8 to 2.2 when the highly inclined nuclear disk is modeled separately from the bulge. These classical bulge components have Sérsic $n \in [1.0, 4.4]$, with four of the nine classical bulge candidates having $n < 2$ (IC 2560, NGC 2960, NGC 6264, NGC 6323).

The classical bulges in Erwin et al. (2015) also tend to have $n < 2$, which suggests that a high Sérsic index is not a hard requirement for low-mass classical bulges using our photometric definition of a rounder, extra-light component (Section 3.1).

Most of the classical bulge Sérsic indices in our late-type galaxies follow the relation with $L_{\rm bulge}$ in early-type bulges (Figure 5, left panels). However, the $n < 2$ bulges have lower n for their luminosity than classical bulges in general. NGC 2960 is an interesting outlier. As suggested by Kormendy & Ho (2013), this galaxy may be a merger remnant. We find a kiloparsec-scale disk in NGC 2960 plus a nuclear disk with a steep profile, neither of which is easily interpreted as a classical bulge. If we instead consider its basic bulge (bottom left panel of Figure 5), then it falls in line with the general trend.

4.3.3. The μ_e–R_e Relation

We also investigate a projection of the Fundamental Plane (Djorgovski & Davis 1987; Dressler et al. 1987) to see whether we have isolated components that scale like elliptical galaxies. We use the Kormendy (1977) relation between the effective radius and the SB measured within the effective radius (μ_e). Based on morphology, we have asserted that most of our galaxies harbor pseudo-bulges. Structural studies find that pseudo-bulges tend to have lower effective SB at a given size than classical bulges and elliptical galaxies (Carollo 1999; MacArthur et al. 2003; Gadotti 2009; Fisher & Drory 2010; Laurikainen et al. 2010). Thus, we turn to this projection to test whether our bulge candidates have the structure of pseudo-bulges.

In Figure 5 (top right), we show the Kormendy relation for our basic bulges. They reside marginally below the relation for ellipticals and early-type bulges, but have relatively high effective SB compared with the pseudobulge selection advocated by Gadotti (2009). Interestingly, Laurikainen et al. (2010) also find that μ_e decreases in later-type spirals. Since our objects are nearly all S0-Sab galaxies, perhaps we should not be surprised that they do not fall far below the elliptical galaxy relation.

Nevertheless, we find clear evidence for pseudobulge components in the bulge morphologies. Why do these not translate into considerably lower μ_e at a given size as we might expect? We conclude that while nuclear bars, disks, and rings are readily apparent in our HST images, they do not carry a substantial fraction of the central mass. This is why we find only very small changes in mass and size when going from the "basic" to the "classical" bulge component. We can then investigate the nature of the dominant bulge components in these galaxies. From photometry alone, it is difficult to characterize these classical bulge components. In two cases, NGC 2273 and NGC 4388, we have additional kinematic information. Here, we know that there is a nuclear disk on <200 pc scales, followed by $V/\sigma < 1$ further out in the bulge, showing that the stars outside of the nuclear disk are supported predominantly by random motions. In the case of these two galaxies, some of the stars are also part of the known kiloparsec-scale bar (Veilleux et al. 1999; Falcón-Barroso et al. 2006; Greene et al. 2014). For the rest of our galaxies, we do not yet know the kinematics of the stars in our putative classical bulges.
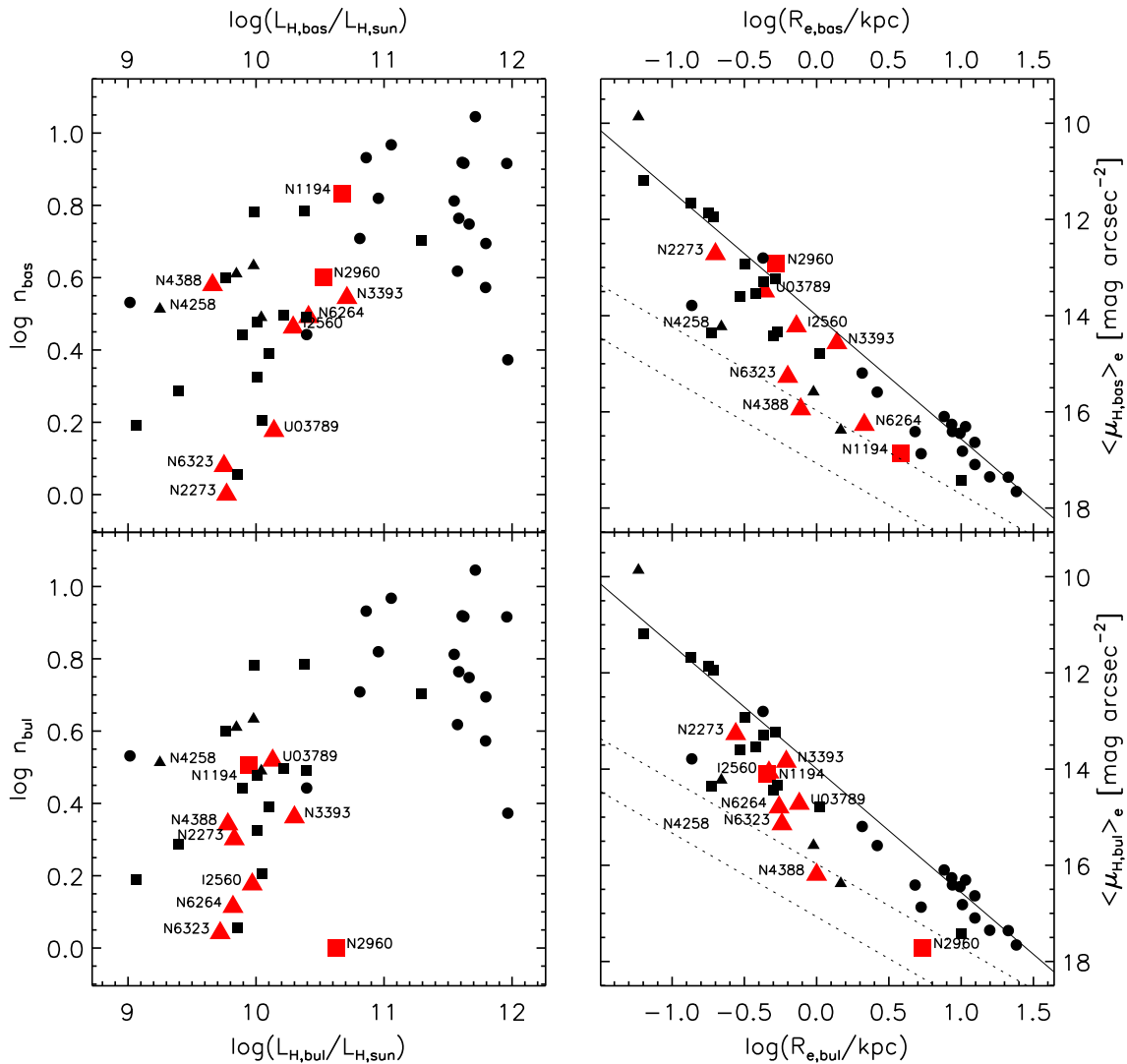
Figure 5. Correlations of photometric bulge parameters. The large red symbols represent the bulges of the present study, with "basic" bulges from bulge+disk decompositions shown in the top panels (subscript "bas") and classical bulges from full decompositions in the bottom panels (subscript "bul"). The bulges of L14 are overplotted as small black symbols, and the only megamaser-based M_{BH} from L14 (NGC 4258) labeled along with the rest of the maser hosts. Circles indicate elliptical, squares lenticular, and triangles spiral galaxies. Left panels: relation between bulge Sérsic index n and H-band bulge luminosity. Our measurements (bulges in mostly spiral galaxies) broadly match the L14 relation (mostly ellipticals and bulges in early-types), but the n–L_H correlation is generally weak. Right panels: H-band surface brightness inside R_e (μ_e) vs. R_e (Kormendy 1977). Overplotted in solid is the fit for early-type galaxies by Khosroshahi et al. (2000), transformed from K to H band using an average $H - K = 0.3$ mag and distances corrected from their $H_0 = 50$ km s^{-1} Mpc^{-1} to our $H_0 = 70$ km s^{-1} Mpc^{-1}. Dotted lines mark the upper limit for pseudobulge brightness recommended by Gadotti (2009), assuming $i - H = 2.1$ and $i - H = 3.2$ (the bluest and reddest bulge colors, respectively, in our sample): the classical bulge measurements for the megamaser hosts are only slightly below the early-type relation and avoid the region of pseudo-bulges, suggesting we indeed excluded the latter and recovered the classical bulge component. However, this applies to the basic bulge measurements as well, which have on average larger size and lower surface brightness than the classical bulges from full decompositions.

4.4. Final Bulge Classification

For each galaxy, we will summarize the evidence demonstrating that we have a pseudobulge, a classical bulge, or both. We established that in nearly all cases, megamaser disk host galaxies show unambiguous pseudobulge signatures in the form of nuclear rings, nuclear or inner ($\lesssim$1 kpc) disks, central dust, and spiral structures. The presence of these components is our criterion for classifying a galaxy as containing a pseudobulge.

We have also attempted to isolate classical bulges. As criteria for classical bulge determination, we use the folloiwng: (1) shape: they should be rounder than the large-scale disk; (2) SB in relation to the effective radius: they should be close to the relation between μ_e and R_e defined by elliptical galaxies; and (3) Sérsic index: they should have high ($n > 2$) values. In our view, the Sérsic index is the least reliable discriminator of classical bulges

due to the large scatter in the n–L plane. We determine that a galaxy contains a classical bulge if it satisfies two of these three criteria. For each galaxy, we assign a P to indicate a likely pseudobulge and a C to indicate a likely classical bulge.

IC 2560: IC 2560 is a relatively strongly inclined galaxy with a readily apparent X-shaped bar/bulge, which provides clear evidence for a pseudobulge component. We do identify a small classical bulge candidate that is rounder than the disk ($q = 0.6$ versus $q = 0.4$). The position in the μ_e–R_e diagram, which is close to the relation of early-type galaxies, likewise points toward a classical bulge, while the Sérsic index is somewhat low ($n = 1.5$). However, despite the above classical bulge indicators, given the dust and complexity of IC 2560 in the central regions, we cannot confirm that this small component is indeed a classical bulge. (P)

NGC 1194: This edge-on, bulge-dominated galaxy is difficult to fit robustly due to significant dust contamination and a likely bar. The basic and classical bulge fits are round and both have a high Sérsic index. The effective SB is not as high as in massive ellipticals, but is higher than expected for a pseudobulge based on the work of Gadotti (2009). Overall, we determine that NGC 1194 contains a classical bulge. We do not find any pseudobulge component. (C)

NGC 2273: While the μ_e–R_e position is consistent with expectations for classical bulges, the axis ratio of the putative classical bulge component matches that of the disk. The Sérsic index is intermediate with $n = 2$. The superposition of the candidate bulge component with the strong bar complicates significant detection of a classical bulge, and given the generally complex inner structure, we conclude that there is not sufficiently compelling evidence for a classical bulge component. NGC 2273 unambiguously contains pseudobulge components. From photometry, it has long been known to contain multiple rings and a nuclear disk (Erwin et al. 2003). More recently, kinematic evidence has confirmed that the central ∼200 pc is dominated by a disk (Barbosa et al. 2006; Falcón-Barroso et al. 2006). There is also a kiloparsec-scale bar component. (P)

NGC 2960: Apart from a large-scale smooth and round component, this galaxy contains two central disks: one nuclear and one ∼1 kpc sized with inset spiral structure. It is particularly challenging in this case to determine what component comprises the bulge. Treating the nuclear disk component as the classical bulge yields a very low Sérsic index but a high central SB. The other option was suggested by KH13; the galaxy may be an elliptical that just swallowed a spiral galaxy. In that case, the classical bulge may be the outer component and the inner (1 kpc) disk a recently acquired addition. The outer component is round, and the observed low μ_e is likely an artifact of the distortion to the center caused by the merger. Although this component technically does not satisfy our classical bulge requirements, we treat it as a classical bulge distorted by a merger. Since we detect an inner disk, it has a clear pseudobulge component. (CP)

UGC 3789: This galaxy is relatively face on, and so using the shape is challenging. However, given the high Sérsic index $n = 3.3$ and relatively high μ_e, we identify a classical bulge component. We see clear signs for pseudobulge components in the nuclear and larger-scale rings. (CP)

NGC 3393: Similar to UGC 3789, this galaxy is close to face on. The classical bulge candidate is round and has a Sérsic index $n = 2.3$. Because the galaxy is face on, we cannot infer much about the intrinsic shape of the component. The high effective SB, combined with $n > 2$, argues for a classical bulge. NGC 3393 contains multiple rings and a bar. The evidence for pseudobulge components is clear. (CP)

NGC 4388: The classical bulge fit to this galaxy is rounder than the disk by a factor of two. However, given the low μ_e of the putative classical bulge, $n \approx 2$, and the significant dust extinction toward the galaxy center, we do not find a convincing classical bulge component. This well-known galaxy has a kiloparsec-scale bar that has been studied kinematically (Veilleux et al. 1999). On the smallest scales, we have identified a nuclear disk both from *HST* photometry and our NIR spectroscopy (Greene et al. 2014), which all points to a pseudobulge component. (P)

NGC 6264: One of the most distant galaxies in the sample, this galaxy clearly contains a kiloparsec-scale bar, and thus a pseudobulge component. The galaxy is close to face on, and so the axis ratio is not very constraining. The Sérsic index is low ($n \approx 1$), but μ_e is relatively high. Given the lack of consensus between the different indicators and the distance of the galaxy leading to extra degeneracy with the bar, we do not robustly identify a classical bulge. (P)

NGC 6323: We fit a very round central component as a classical bulge candidate. The combination of the low Sérsic index of $n \approx 1$ and the low SB suggest that we have not isolated a classical bulge component. In contrast, the structural properties of the bulge and the inner kiloparsec-scale disk/ring lead us to conclude that NGC 6323 harbors a pseudobulge (P).

Armed with these bulge classifications, luminosities, and stellar masses for our different stellar components, we now turn to the primary goal of this paper, i.e., the BH scaling relations.

5. RESULTS: BH SCALING RELATIONS

Our goal is to learn about the origin of the BH-galaxy scaling relations by studying their slope, zeropoint, and scatter over as wide a dynamic range as possible. Before this work, there were very few dynamical BH masses in late-type galaxies. We add nine new systems with structural measurements.

5.1. The Special Role of Megamaser Disk Galaxies

In this subsection, we focus on the megamaser disk galaxies taken alone (including NGC 4258 from L14). Megamasers play two important roles. First and foremost, VLBI allows us to resolve much smaller spheres of influence than optical or NIR stellar- or gas-dynamical methods, and the usually near-perfect Keplerian rotation curves traced by the masers provide the most precise and accurate extragalactic BH mass measurements. Nuclear megamasers probe the full range of BH mass at a given galaxy property in a way that no other current technique can. Second, as a corollary, they allow us to probe BH mass in spiral galaxies where gas, dust, and typically small spheres of influence all conspire to make stellar or gas-dynamical techniques especially challenging.

The megamaser disk galaxies span a stellar mass range of $\log M_*/M_\odot = 10.5\text{–}11.1$ (only a factor of four), and yet the BH masses span a range of $\log(M_{BH}/M_\odot) \approx 6.4 - 7.8$, that is, a factor of 25. If we take the scaling relations measured for predominantly early-type galaxies from L14, then for the measured BH masses we expect a range in bulge mass of $10^8\text{–}10^{10} M_\odot$, which corresponds to a range in bulge-to-total light (B/T) of 10^{-3} (for IC 2560) to 0.2 (NGC 1194), with a median value of 0.03. In contrast, galaxies of these Hubble types (S0-Sb) typically have B/T $\approx 0.1 - 0.2$ (Simien & de Vaucouleurs 1986; Laurikainen et al. 2010). It is already clear before we perform any fitting that these BHs would need to have very small classical bulge components if they were to obey the scaling relations seen in early-type galaxies. A similar conclusion was reached for the $M_{BH}\text{–}\sigma_*$ relation by Greene et al. (2010; see also KH13 for other references).

The maser galaxies occupy a range of bulge masses of $\log M_*/M_\odot = 9.5 - 11$. The wide distribution in BH mass in a narrow range of galaxy properties[14] shows us that there is not a tight correlation between M_{BH} and galaxy or bulge mass for

---

[14] Within this range, two galaxies in the L14 sample have $M_{BH} > 10^8 M_\odot$, increasing the total range of M_{BH} yet further (Figure 6).

galaxies with $M_* \lesssim 10^{11} M_\odot$. Instead, the measured correlation found for early-type galaxies defines an upper envelope for the BH mass with many of the megamaser galaxies scattering below this relation. As we will quantify in the following subsections, this broad tail toward low M_{BH} appears to hold even when we consider bulge rather than total galaxy mass.

This tail to low BH mass, which is most clearly apparent in the megamaser disk galaxies, raises a more basic question about the scaling relations. We have to wonder whether the scaling relations reflect the true distribution in nature, or whether they reflect our inability to measure low-mass BHs in high-mass galaxies (Batcheldor 2010). Gültekin et al. (2011) explore the possibility that the $M_{BH} - \sigma$ relation is only an upper envelope, since galaxies with unresolved gravitational spheres of influence may be preferentially missing. At high galaxy mass, $\sigma_* > 250$ km s^{-1} (corresponding roughly to $\sim 10^{11} M_\odot$; e.g., Häring & Rix 2004), Gültekin et al. (2011) show that the existing dynamical BH mass sample is large enough to rule out a long tail to low M_{BH}.[15] However, at lower stellar velocity dispersion, a large range in M_{BH} at fixed galaxy property is what we observe. We discuss the possibility of bias in the low-mass galaxy sample, along with the possibility of bias in the megamaser disk galaxies, in Section 6.1. First, we quantitatively fit the relationships between M_{BH} and measured galaxy properties.

5.2. Fitting Method

We use the IDL implementation of the Bayesian inference-based LINMIX_ERR (Kelly 2007) for fitting our BH scaling relations between M_{BH} and the galaxy properties. This routine naturally implements intrinsic scatter in the y-coordinate as part of the model, i.e., the relation is modeled as a probability distribution in (x, y) space. It renders a Markov Chain Monte Carlo (MCMC) realization of the posterior distribution of the linear relation parameters, which are the zeropoint (α), slope (β), and dispersion of the Gaussian intrinsic scatter (ϵ). We thus fit relations of the form

$$y = \alpha + \beta(x - x_0) + \mathcal{G}(\epsilon), \qquad (4)$$

where $y = \log(M_{BH}/M_\odot)$, x are logarithmic luminosities or masses, i.e., $x = \log(L_H/L_{\odot,H})$ or $x = \log(M/M_\odot)$, and $G(\epsilon)$ symbolizes a Gaussian probability distribution with dispersion ϵ. The x-offset x_0 is calculated before fitting as the mean of the x-coordinates of the data in order to reduce covariance between α and β. The linear relation (4) implies a power law between M_{BH} and L_H or M^*, and $\beta = 1$ corresponds to a linear relation between M_{BH} and the galaxy property. Some recent papers have suggested a broken power-law fit to BH scaling relations with bulge luminosity or mass (e.g., Graham & Scott 2015). This is an interesting possibility, but we do not have a sufficient sample size in this paper to address that possibility rigorously. The values quoted in Table 8 are the mean values of the parameters in the Markov Chain, and the given intervals delineate the 68% confidence interval of the drawn samples relative to the mean.

---

[15] That is, barring dramatic problems with the BH masses, such as very steep IMF gradients (McConnell et al. 2013; Martín-Navarro et al. 2015).

5.3. Subsamples

When we combine the megamaser disk galaxies with L14, we obtain a large enough sample to split galaxies based on various properties and then ask where they fall in the BH-bulge mass plane. We will focus exclusively on the 44 galaxies (L14 and ours) that have dynamical BH mass measurements as described in Section 4.

We consider the following subsamples. We investigate the scaling of the 10 megamaser galaxies, which includes NGC 4258 from the L14 sample. We also group all late-type galaxies. Many works (Greene et al. 2008, 2010; Hu 2008; Gadotti 2009; Kormendy et al. 2011) have suggested that late-type galaxies with pseudo-bulges may obey different scaling relations than classical bulges, since secular evolution may not efficiently fuel BH growth. In practice, because there is considerable overlap between the late-type and pseudobulge samples (7/9 of our megamaser sample), we will only consider one late-type subsample comprising the eight non-S0 mega-masers and the three additional spiral galaxies from L14. Finally, we consider a low-mass sample, since if the scaling relations arise from hierarchical merging via the central limit theorem (e.g., Peng 2007; Jahnke & Macciò 2011), then the scaling relations would break down at low mass. For this subsample, we simply take the 22 lowest-mass or lowest-luminosity galaxies.

We calculate the offset of each subsample from the "primary relation," which is the relation fit to the data excluding the respective subsample. For each Monte Carlo realization of the primary relation, the offset Δa (Table 8) is the weighted-mean ($y = \log M_{BH}$)-offset of the subsample from the primary relation. The weights are the y- and projected x-measurement errors, plus the intrinsic scatter in the relation, added in quadrature. We take into account the uncertainty in Δa by drawing it from its (Gaussian) error distribution around the weighted-mean offset. We subsequently determine the intrinsic scatter of the subsample (ϵ) by iteratively varying its value, and adding it in quadrature to the measurement errors until $\chi^2 = 1$ for the given primary relation slope and subsample offset. We thus calculate Δa and ϵ for each element of the Markov chain, and the resulting Δa and ϵ distributions are evaluated for their mean and 1σ uncertainty. The offset for the maser sample is referred to as Δa_{mega}, while that for the late-type galaxies is Δa_{late}, and the low-mass sample is Δa_{low}.

There is another sample of spiral galaxies with indirect BH masses, based on reverberation mapping. A subsample of the reverberation-mapped AGNs have *HST* imaging that allows detailed bulge-disk decompositions (Bentz et al. 2009a). These fall in an inferred M_{BH} range of 10^7–$10^9 M_\odot$ that overlaps with the megamaser disks at the low-mass end. Many of the hosts are also disk galaxies. Bentz et al. (2009b) find that M_{BH} is quite tightly correlated with L_{bul} (even with no conversion to mass) and they do not observe the long tail to low M_{BH} that is seen with the megamaser galaxies. Interestingly, the scatter seen between M_{BH} and σ_* is also smaller at $M_{BH} \approx 10^7 M_\odot$ for the reverberation-mapped sources than the megamaser disk galaxies (e.g., Greene et al. 2010; Woo et al. 2010). We discuss this difference in Section 6.1.

We also note that there are two other prominent outliers in the BH-bulge scaling relations (S0 galaxies NGC 4342 and NGC 3998) that have apparently high M_{BH} for their stellar mass. In both galaxies, the bulge luminosity is strongly dependent on the adopted decomposition (for details, see

Table 8
Scaling Relation Parameters $\log(M_{BH})-\log(x)$ with Galaxy Properties and Galaxy Subsamples

x	x_0	α		β		ϵ		Δa_{mega}		ϵ_{mega}		Δa_{late}		ϵ_{late}		Δa_{low}		ϵ_{low}	
		val	err	val	err	val	err	val	err	val	err	val	err	val	err	val	err	val	err
L_{bul}	10.56	8.13	0.09	0.87	0.11	0.56	0.07	−0.63	0.21	0.90	0.11	−0.51	0.24	0.73	0.12	0.09	0.39	0.72	0.14
L_{bas}	10.64	8.12	0.09	0.99	0.13	0.57	0.07	−0.80	0.22	0.93	0.13	−0.58	0.24	0.76	0.13	0.04	0.37	0.76	0.13
L_{tot}	10.93	8.12	0.11	0.99	0.19	0.71	0.09	−1.13	0.21	1.35	0.11	−1.03	0.22	1.23	0.12	0.47	0.40	1.04	0.25
M_{bul}	10.66	8.12	0.08	0.88	0.10	0.52	0.06	−0.58	0.21	0.79	0.12	−0.49	0.22	0.70	0.12	−0.22	0.31	0.71	0.12
M_{bas}	10.74	8.13	0.09	0.98	0.12	0.56	0.07	−0.76	0.22	0.89	0.13	−0.57	0.24	0.74	0.14	0.05	0.34	0.74	0.11
M_{tot}	11.01	8.13	0.10	1.04	0.17	0.68	0.08	−1.05	0.20	1.25	0.11	−0.98	0.21	1.16	0.12	−0.04	0.36	0.84	0.12

Note. The first column identifies the quantity x that is, respectively, fitted by a relation $\log(M_{BH}/M_\odot) = \alpha + \beta(\log(x/x_\odot) - x_0) + G(\epsilon)$ (Equation (4) in Section 5.2), where $x_\odot$ is $L_{\odot,H}$ or $M_\odot$, and $G(\epsilon)$ denotes a Gaussian distribution with dispersion ϵ. Given in the second column is the offset x_0 (the inverse variance-weighted mean of all x), which is subtracted from the x before fitting in order to reduce covariance between α and β. All other parameters are fit to the data using LINMIX_ERR and the resulting Markov Chain Monte Carlo (MCMC) sample, which is evaluated for the mean ("val") and the standard deviation ("err," i.e., the size of the 68%-confidence interval). These parameters are as follows: the relation zeropoint (α), logarithmic slope (β), and log-scatter in the $y = \log(M_{BH}/M_\odot)$-direction (ϵ) for the fit to the entire sample of 44 objects, as well as the respective offset and intrinsic scatter of three subsamples: megamasers ("mega"), spiral galaxies ("late"), and low-mass galaxies ("low"). Low-mass galaxies always constitute half of the sample, i.e., those 22 galaxies for each relation with the lowest x values. The subsamples' offsets are relative to a relation fit to the data minus the subsample; the parameters of these relations are not shown here. The subsample scatter ϵ is relative to the offset relation with the same β as the main relation.

Läsker et al. 2014a). However, even taking the total luminosity as an upper limit on L_{bul} still puts their M_{BH} above the M_{BH}–L_{bul} relation. In the case of NGC 3998, M_{BH} would be five times lower if the gas-dynamical measurement was adopted instead of the stellar-dynamical model, which is true for many galaxies with both stellar and gas dynamical measurements (see Walsh et al. 2012). The BH mass measurement in NGC 4342 is based on stellar dynamics. Here, the large M_{BH} for its (bulge) luminosity is similar to an emerging class of S0 galaxies that appear to have overly massive BHs for their stellar bulge mass (van den Bosch et al. 2012; Walsh et al. 2015, 2016). These galaxies tend to be very compact with large central velocity dispersions and fast rotation on large scales, live in rich environments, and may have very different formation histories than the megamaser galaxies studied here. However, they contribute to our overall conclusion that there is very significant scatter in M_{BH} for bulge masses $<5 \times 10^{10} M_\odot$.

5.4. The M_{BH}–M_{bas} Relation for Basic Bulges

We begin by examining the "basic" bulge fit, in which we assume that the galaxy can be well fit by the combination of a bulge, disk, and possible point source (Figure 6, left). These fits represent an upper limit on the bulge component, and are also a good analog to fits in the literature to the SDSS (e.g., Lackner & Gunn 2012) and to higher-redshift galaxies (Bell et al. 2012). The expected range of H-band bulge luminosities for the megamaser disks, based on the scaling relations, is 10^8–$10^{10} L_\odot$. The observed range, in contrast, is much narrower (3×10^9–$4 \times 10^{10} L_\odot$). If we measure the average offset in M_{BH} between the megamaser disks and the best-fit L14 relation (Δa_{mega} in Table 8, row 2), then we find a mean offset of -0.8 ± 0.2 dex in BH mass from the best-fit relation.

These galaxies tend to have recent or ongoing star formation in their nuclei, which biases the observed bulge luminosities to high values compared with the predominantly old stellar populations that dominate early-type galaxies. We attempt to mitigate these differences by transforming to stellar mass. We try to place both the literature and megamaser galaxies on the same stellar mass scale to facilitate direct comparison (Section 3.6). When considering stellar mass rather than luminosity (Figure 6, right; Δa_{mega} in Table 8, row 5), we still see that the megamaser disks remain offset to smaller BH masses at a given bulge mass (-0.8 ± 0.2 dex).

If we instead examine the offset between the best-fit L14 relation and the spiral galaxy subset, rather than the megamaser subset, then the net offset in M_{BH} declines a bit, $\Delta a_{late} = -0.6 \pm 0.2$ dex. The fact that the measured offset Δa_{late} is smaller than Δa_{mega} is interesting, and indicates a possible difference between the distribution of M_{BH} for megamaser disks and galaxies with stellar/gas-dynamical BH mass measurements.

In summary, when we consider the most general concept of a "bulge" as the centrally concentrated component that constitutes a light excess above the large-scale disk, we find a wide range of BH mass at fixed bulge mass and a significant offset from the early-type M_{BH}–M_{bul} relation for the megamaser disks and late-type galaxies in general. A qualitatively similar result has been seen before in late-type galaxies for the subset of pseudobulge galaxies (Greene et al. 2008; Hu 2008; Sani et al. 2011; Kormendy & Ho 2013).

5.5. The M_{BH}–M_{bulge} Relation for "Classical" Bulge Components

In Section 4, we described in detail our attempt to isolate a classical bulge component in the maser disk galaxies. Considering the colors, shapes, and structures of the putative "classical" bulge components, we identified a classical bulge in four cases (NGC 1194, NGC 2960, NGC 3393, and UGC 3789).

We compare the BH and stellar mass for the confirmed classical bulges (solid symbols) in Figure 7. Obviously, these classical bulge components will, by construction, contain less stellar mass than the basic bulges (typically by ~ 0.2 dex), nominally improving the agreement with the elliptical galaxy M_{BH}–M_{bul} relation. Indeed, we see better agreement overall when plotting M_{BH} against classical rather than basic bulge measurement: the offset in M_{BH} is $\Delta a_{late} = -0.6 \pm 0.2$ dex. However, if we focus only on those galaxies where we believe there is a secure classical bulge component (filled symbols in Figure 7), then we see that there is still a net offset toward lower M_{BH} at a given bulge mass. Thus, we tentatively conclude that simply identifying more robust classical bulges in these galaxies will not eradicate the trend toward higher scatter and lower M_{BH} at a given bulge mass. As noted by Sani et al. (2011) and Läsker et al. (2014a), it is still difficult to definitively rule out that observational issues (e.g., hidden nuclear star clusters or other small-scale components) are contaminating our measurements, but as the number of galaxies with HST data and high-fidelity dynamical BH masses increases, it becomes more and more clear that there is simply a very wide range of M_{BH} in these low-mass galaxies.

5.6. M_{BH}–M_{tot} Relation

There has been considerable interest in recent years in the relation between total stellar mass and M_{BH}, with various claims that total stellar mass should also show a relationship with M_{BH} (Peng 2007), possibly even tighter than bulge mass (Jahnke & Macciò 2011), and one that does not evolve with redshift (Jahnke et al. 2009; Bennert et al. 2010, 2011; Cisternas et al. 2011). We examine the M_{BH}–M_{tot} relation using the L14 and our megamaser samples in Figure 8. Focusing on the stellar mass range where the megamasers are found, we see the most striking mismatch between the range in M_{BH} (2.5 dex) and the range in stellar mass (0.4 dex). Thus, at a fixed stellar mass, galaxies may contain BHs with a wide range of mass. We do not see strong evidence that the total stellar mass to M_{BH} relation is tighter than others in the literature, and we see virtually no correlation at all below $M_* \approx 10^{11} M_\odot$. Regardless, $\epsilon (M_{BH}$–$M_{tot})$ is still marginally consistent with $\epsilon (M_{BH}$–$M_{bul})$ (see Läsker et al. 2014b). We measure an offset between the megamasers and the best-fit L14 relation of $\Delta a = -0.8 \pm 0.2$ dex, which is similar to the apparent offset between active and quiescent BHs observed by Reines & Volonteri (2015).

6. DISCUSSION AND SUMMARY

With the megamaser disk galaxies, we have a sample of $\sim L^*$ spiral galaxies with very precise BH mass measurements. The masers allow us to explore BH demographics in spiral galaxies more robustly than with any other dynamical method.
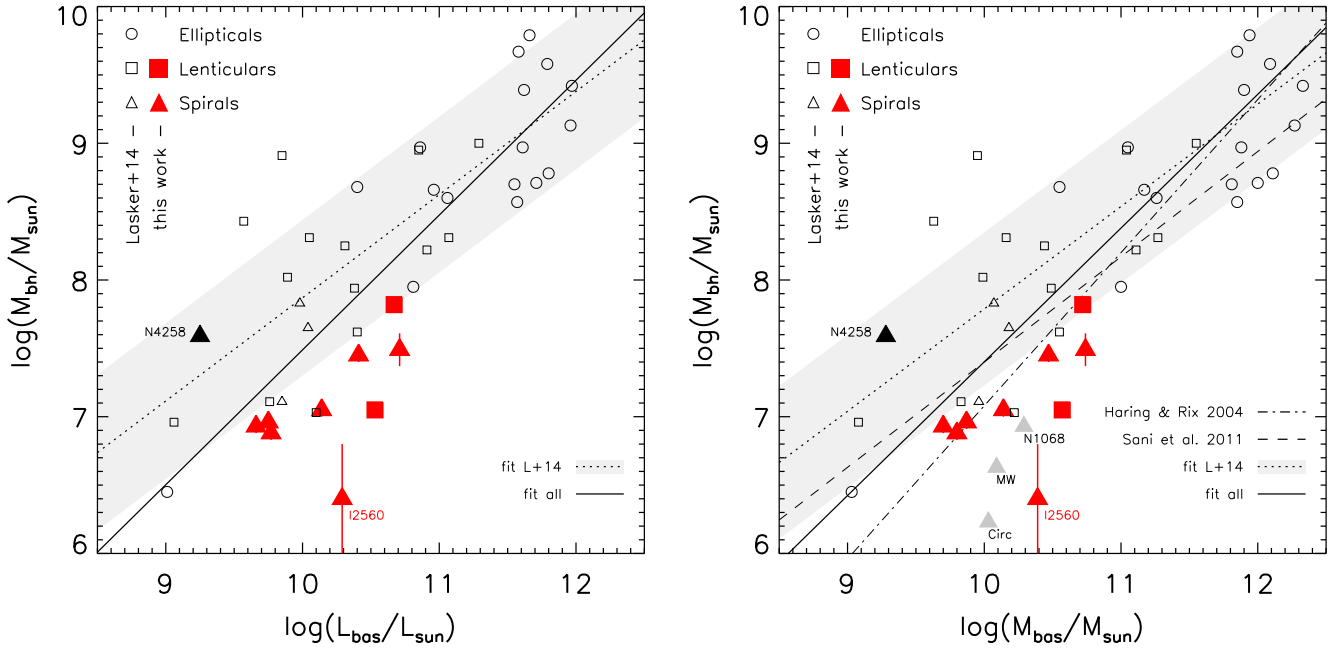
Figure 6. Correlation of $\log M_{BH}$ with "basic" bulge based on simple bulge+disk(+point-source) decompositions of our megamaser BH hosts. We show $\log L_{H,bas}$ (left) and $\log M_{bas}$ (right panel). The maser disks analyzed in this paper based on *HST*/WFC3 imaging are indicated by large filled red symbols with error bars. The errors on the bulge magnitudes are small, as we have not estimated systematic errors for these basic fits. The filled black symbol (NGC 4258, which also has a megamaser-based M_{BH}), and small open symbols (with error bars suppressed for clarity) are values from Läsker et al. (2014a), with their "spheroid" *K*-band luminosity converted to L_H and M as described in Section 3.5. Circles indicate elliptical, squares S0, and triangles spiral galaxies. The solid line represents the fit to the combined sample of L14 and the present study. The dotted line shows the relation fit when restricted to the L14 sample, i.e., with all megamasers except NGC 4258 omitted, and the gray area indicates the 1σ intrinsic scatter (ϵ). For comparison, the M_{BH}–M_{bul} relations of Sani et al. (2011) and Häring & Rix (2004) are overplotted as dashed and dotted–dashed lines, respectively, in the right panel. For illustration, the gray labeled triangles in the right panel show three more BH hosts with M_{bul} taken from the literature. These, however, are excluded from our fit because the Milky Way (MW) bulge mass is highly uncertain while the megamaser-based M_{BH} (Circinus, NGC 1068) are in question.
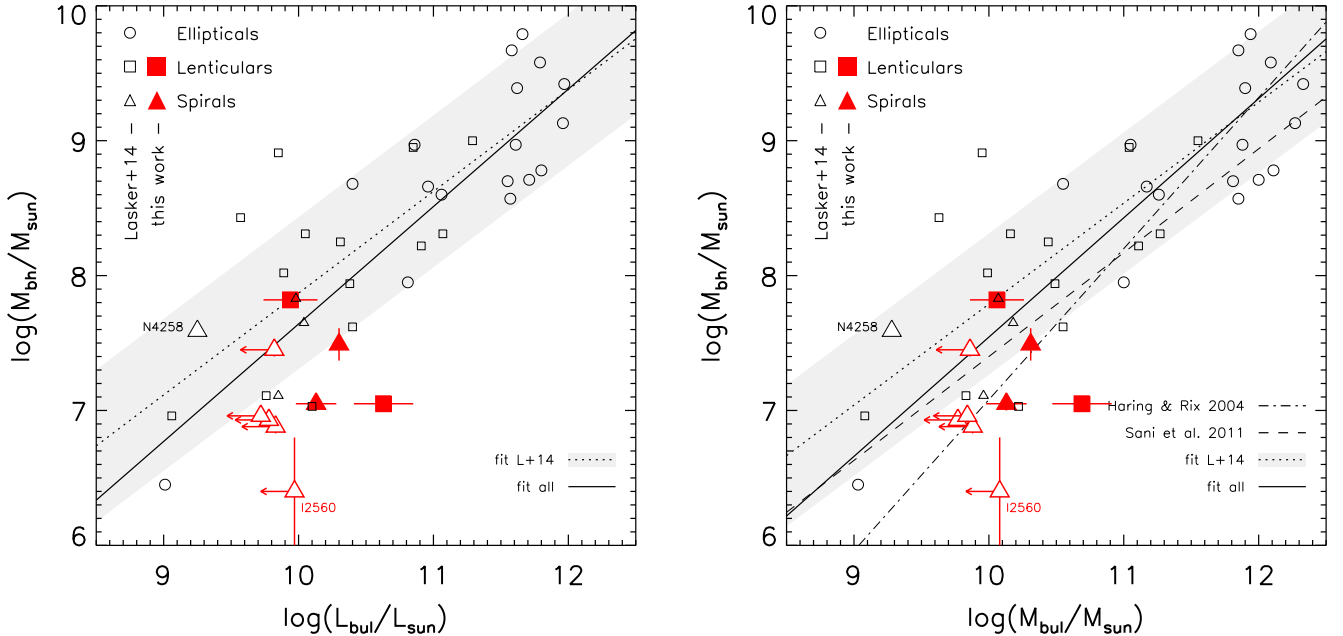
Figure 7. Same as Figure 6, but using the classical bulge parameters from our adopted multi-component decompositions for the megamaser hosts (filled red symbols with error bars). In cases where we do not identify a classical bulge, we plot an open symbol. The megamaser disk galaxy NGC 4258 is indicated as an open triangle. The fits and the literature sample (Läsker et al. 2014a) are the same as in Figure 6. Using the more detailed decompositions moves the megamasers closer to the relation of the L14 sample, but only slightly so. Similarly, the conversion to mass reduces the scatter marginally. The megamaser galaxies also appear to have lower M_{BH} at a given L_{bul} or M_{bul} than the general BH host population, while their scatter is similar to other galaxies in the low-mass regime they occupy.

First, we can spatially resolve the spheres of influence of much lower-mass BHs, allowing us to probe the full range of M_{BH} at fixed galaxy property. Second, the maser disks are not impacted by the dust and mixed stellar populations that challenge stellar and gas-dynamical techniques (although see also den Brok et al. 2015).
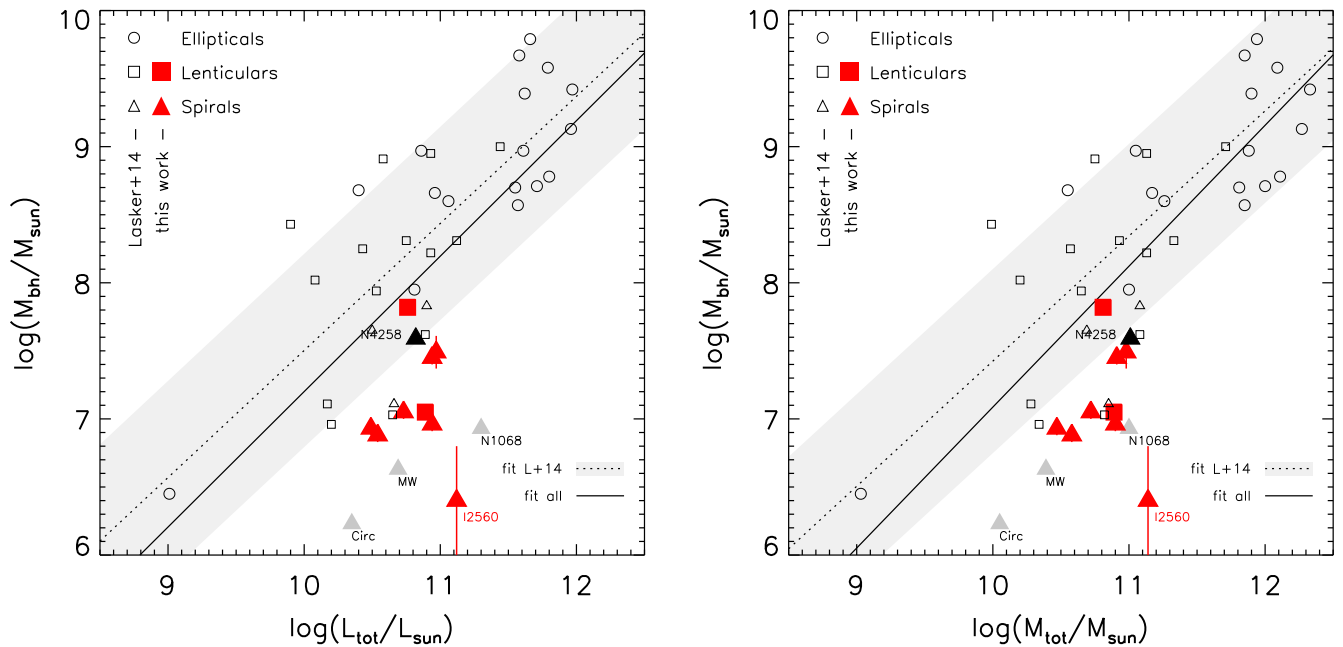
Figure 8. Correlation of $\log M_{BH}$ with total $\log L_{H,tot}$ (left panel) and $\log M_{tot}$ (right panel), for the megamaser BH hosts (large filled symbols, red for this study, NGC 4258 in black) and for the L14 sample of BH hosts with M_{BH} from stellar or gas kinematics (small symbols). Symbols shapes (Hubble type) and lines (relation fits) are defined as in Figures 6 and 7. As for the relation with bulges, the megamaser hosts reside at lower M_{BH} than predicted by the fit (dotted line) to the predominantly early-type BH host galaxy sample (open symbols) of Läsker et al. (2014a).

6.1. The Role of Bias in Different BH Samples

The megamaser disk galaxies span 1.5 dex in BH mass but only 0.6 dex in galaxy mass. Furthermore, the ratio of M_{BH}/M_* is, on average, considerably lower than what is seen in more massive elliptical and S0 galaxies. This long tail to low M_{BH} at fixed stellar mass is seen most conclusively in the maser disk samples, likely due to the difficulties of resolving the gravitational sphere of influence for low-mass BHs (Batcheldor 2010; Gültekin et al. 2011; van den Bosch et al. 2015). In the stellar mass range probed by the maser disks ($M_* < 10^{11}\, M_\odot$), in this paper we see a hint that stellar-dynamical, gas-dynamical, and reverberation-mapped samples do not truly sample the full range of M_{BH} at a given M_*. In particular, only the megamaser disk galaxies extend to the lowest M_{BH} probed at a fixed galaxy mass. In the case of the stellar and gas-dynamical measurements, it is not surprising that the BHs do not sample the low-mass regime, since we cannot resolve their sphere of influence. Thus, we argue that only the megamaser disks reveal the true distribution of M_{BH} at a given galaxy property.

It is more difficult to pin down the origin of the difference between the maser and the reverberation-mapped sources. One possibility is a bias in the reverberation-based BH masses, which after all have been calibrated to follow the inactive M_{BH}–σ relation. Alternatively, the reverberation sources may also have a bias toward higher M_{BH} at a given galaxy mass, due to the preferential selection of the most luminous sources with correspondingly high-mass BHs. Until we come to a full understanding of this issue, it will be difficult to fully compare the scaling relations for single-epoch virial BH masses with dynamical BH masses (e.g., Graham & Scott 2015; Reines & Volonteri 2015).

Alternatively, the megamaser disk sample could have a bias toward lower M_{BH} at fixed galaxy property due to their selection as active galaxies if, for some reason, the megamaser

disks pick out galaxies that are preferentially still growing toward the end state of the M_{BH}–σ relation. The megamaser disks are nearly the only active galaxies with dynamical BH masses, and so it is worth considering the possibility that masers select a non-representative sample. We argue against that possibility, repeating the arguments in Greene et al. (2010). The galaxies are found, on average, a factor of four below the relation between M_{BH} and L_{bulge}. To erase this offset, at their current Eddington ratios of $\sim$10% (Greene et al. 2010), would require $\sim$1 Gyr of steady BH growth. On the other hand, the typical lifetimes of AGNs are likely shorter than this (Martini & Weinberg 2001) while pseudobulge growth times are much longer (Kormendy & Kennicutt 2004), and so how the megamaser disks would know to grow at this particular moment is difficult to understand. Furthermore, if such a bias impacted the maser galaxies, then we would expect to see the same effect in the reverberation-mapped sources, which we do not.

In principle, it is also possible that megamaser disk galaxies are biased against the most massive BHs (Reines & Volonteri 2015; van den Bosch et al. 2016). However, if there were a large sample of spiral galaxies with very massive BHs ($\gtrsim 10^8\, M_\odot$), then we would likely know about them already from stellar- or gas-dynamical M_{BH} measurements.

### 6.2. Differences in Scaling Relations

Barring such biases, megamaser disks enable us to probe the underlying distribution of BH mass for spiral galaxies. The observations presented here apply (at minimum) to all BHs in spiral galaxies with $M_* < 10^{11}\, M_\odot$. That is, at a fixed galaxy property, there is a large range of M_{BH}, extending systematically below the relations defined by the early-type, massive galaxies.

We consider two explanations for the differences in scaling relations between the masers and early-type galaxies. One is
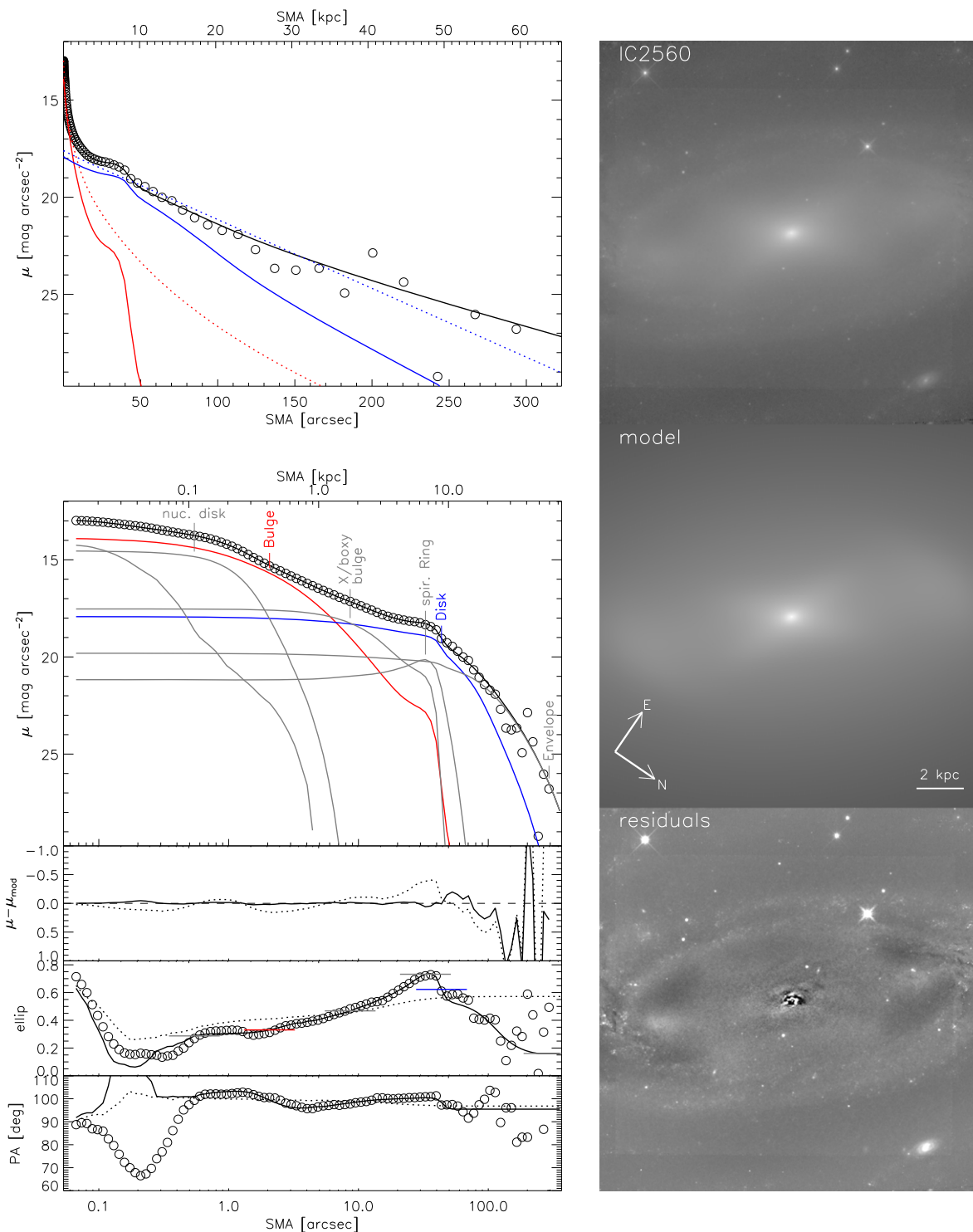
Figure 9. IC 2560 photometric data and model. Left panels: semimajor-axis (SMA) profiles of H-band surface brightness (μ), data-model residuals ($\mu - \mu_{\mathrm{mod}}$), ellipticity (ellip), and east-of-north position angle (PA). Open circles show the observed data, and solid lines the full model (thick black), its bulge (red), main exponential disk (blue), and all other model components (thin gray lines). For comparison with our best-fit model, shown by the dashed lines are total (black), bulge (red) and disk (blue) profiles of the "basic model," which includes only a bulge and disk (for IC 2560, the point source could not be fitted in the basic model as the best-fit bulge+disk model over-predicts the central flux). The top-left panel plots mu against linear SMA and shows the basic model bulge and disk, while the lower panels use a logarithmic SMA scaling and omit the basic model components for better visibility of the full model's multiple components. See Figure 10, for the basic model components' μ–log(SMA) profiles. The names and ellipticities (horizontal bars) of the full model's components are indicated at the SMA distances where the components' contribution to the total flux is maximal. In IC 2560's full model, the envelope accounts for the strongly increased flattening at $\gtrsim$20 kpc, the spiral arms are tightly wound and hence modeled by a ring with inner truncation, and the X-shaped pseudobulge by a Sérsic with best-fit index $n = 0.5$ and a 4th-order isophote harmonic. Right panels, from top to bottom: the image data and full model on a logarithmic grayscale, and full model residuals on a linear grayscale. Evident is a residual spiral structure in the innermost regions, presumably from an unmodeled nuclear disk.
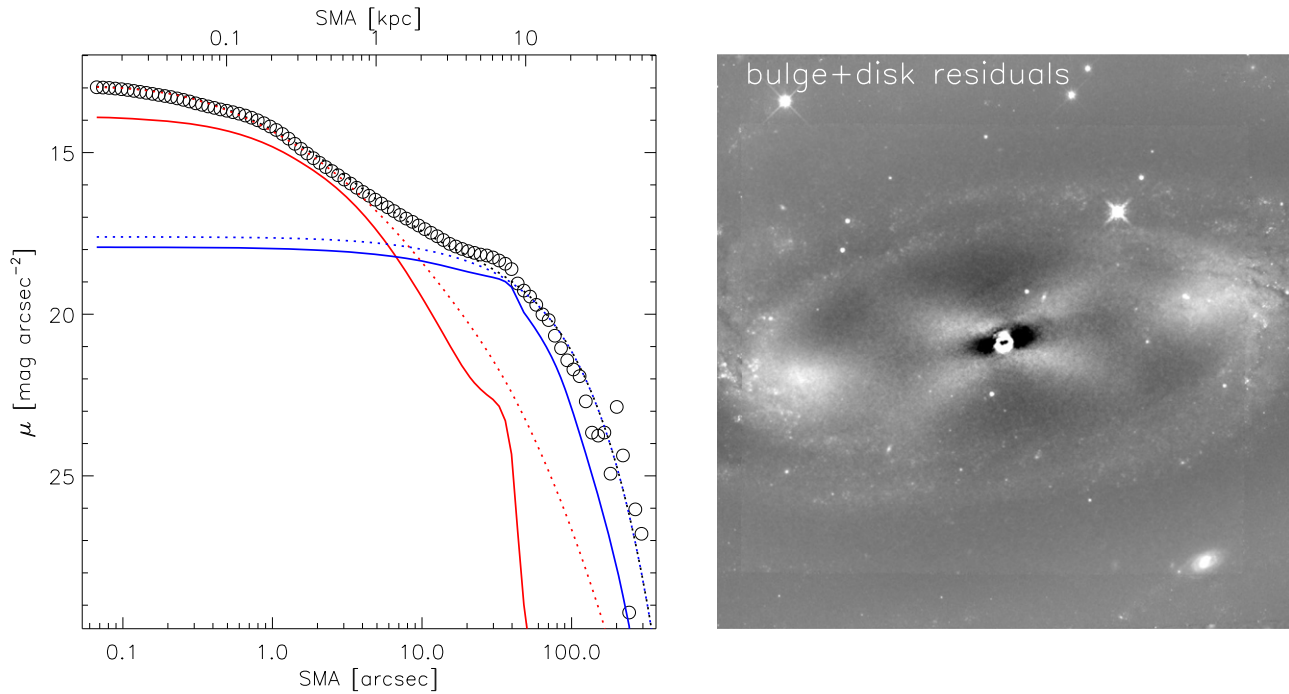
Figure 10. IC 2560 photometric data and model, continued from Figure 9. Left panel: logarithmic semimajor-axis (SMA) *H*-band surface brightness (μ) of the data (open circles), full model (solid lines) and basic bulge+disk model (dashed). The black lines represent the total model μ, red the bulge, and blue the disk contribution. The other components of the full model are not shown (but see Figure 9. Right panel: data-model residuals of the basic (bulge+disk) model. The bright onset of the spiral arms is unaccounted for, as well as the X-shaped pseudobulge. The central brightness is overpredicted by the basic model, and therefore the point source cannot be fitted before the mentioned components are included in a full model.

that the scaling relations vary with galaxy morphology. In this picture, the formation history of the galaxy (e.g., the formation of a massive bulge) is tied to the fueling and feedback processes of the growing BH. For instance, galaxies that build their central bulges primarily with secular processes may never efficiently fuel their BHs (e.g., Gadotti 2008; Greene et al. 2008; Hu 2008). This would result in the observed offset to lower masses, along with significant scatter, preferentially among spirals. To test these possibilities, we urgently need BH mass measurements in more bulge-dominated, low-mass galaxies like M32. We also note the intruiging possibility raised by Saglia et al. (2016) that, at high enough mass density, the BHs in pseudo-bulges obey the same scaling relations

The other possibility is that the BH scaling relations are driven by merging via the central limit theorem, as advocated by Peng (2007) and Jahnke & Macciò (2011). In this picture, galaxies with fewer mergers do not converge to a tight scaling relation, leading to a strong dependence of scatter on the galaxy (or halo) mass. If we could measure the scatter in the scaling relations as a function of mass and morphology over the full range of M_{BH}, then we could determine which of these scenarios is preferred. Unfortunately, we still have very few measurements at low mass, and vanishingly few in low-mass, early-type galaxies (M32, van den Bosch & de Zeeuw 2010; NGC 404, Seth et al. 2010, D. D. Nguyen et al. 2016, in preparation; NGC 4395, den Brok et al. 2015). It remains very challenging to distinguish these two possibilities.

Finally, there is the possibility that the scaling relations are completely artificial and actually just define an upper envelope that arises due to problems with the stellar and gas-dynamical methods. Others have considered this possibility (Batchel-dor 2010; Gültekin et al. 2011; van den Bosch et al. 2015). In

the coming decade, ALMA (Davis 2014) and 30m-class telescopes (Do et al. 2014) will provide an order of magnitude increase in angular resolution, allowing us to test this possibility. What we really need are megamaser disks in early-type galaxies. Searches thus far have not been successful (van den Bosch et al. 2016), but they are worth continuing.

Despite significantly increasing the sample of L^* spiral galaxies with dynamical M_{BH} measurements, our samples at low mass and late-type morphology remain small. Thus, our conclusions are not yet definitive. While we did our best to identify classical bulges with photometric indicators, a combination of photometry and kinematics would undoubtedly work better (e.g., Erwin et al. 2015). Luckily, there are additional megamaser disk galaxies with Keplerian rotation curves and secure M_{BH} being observed with *HST* in Cycle 22 (P.I. Greene). We are also securing AO-assisted integral-field observations of the stellar and gas kinematics in five of these objects with SINFONI on the VLT (P.I. Greene). The combination of these two data sets should prove powerful in setting our results on firmer ground.
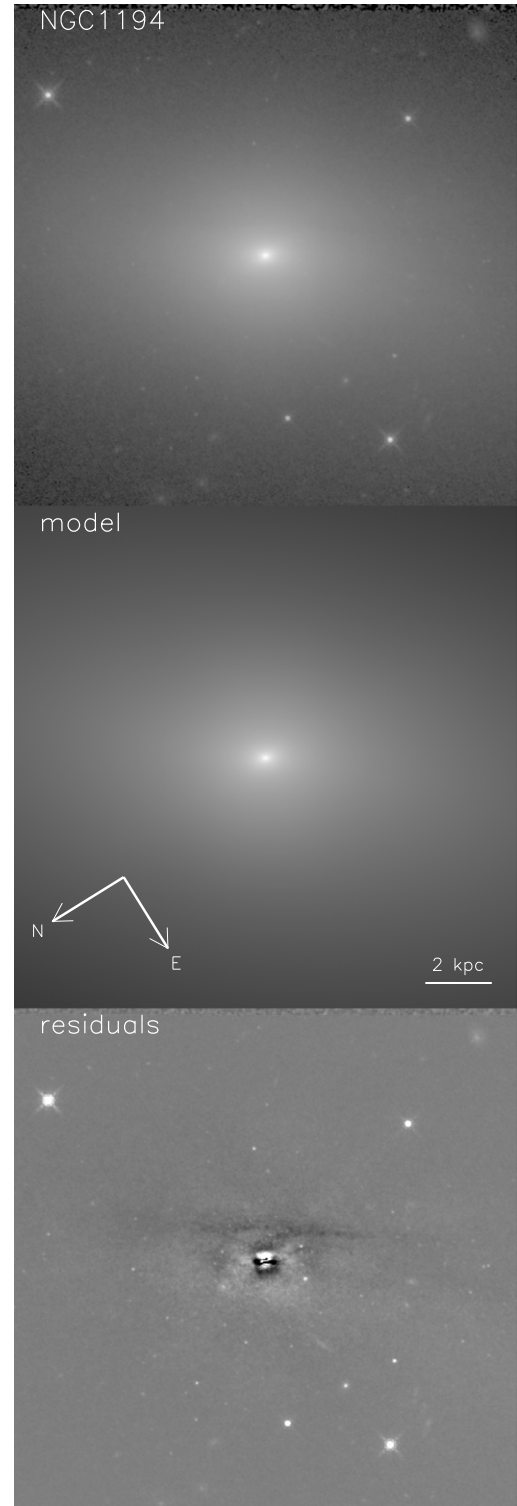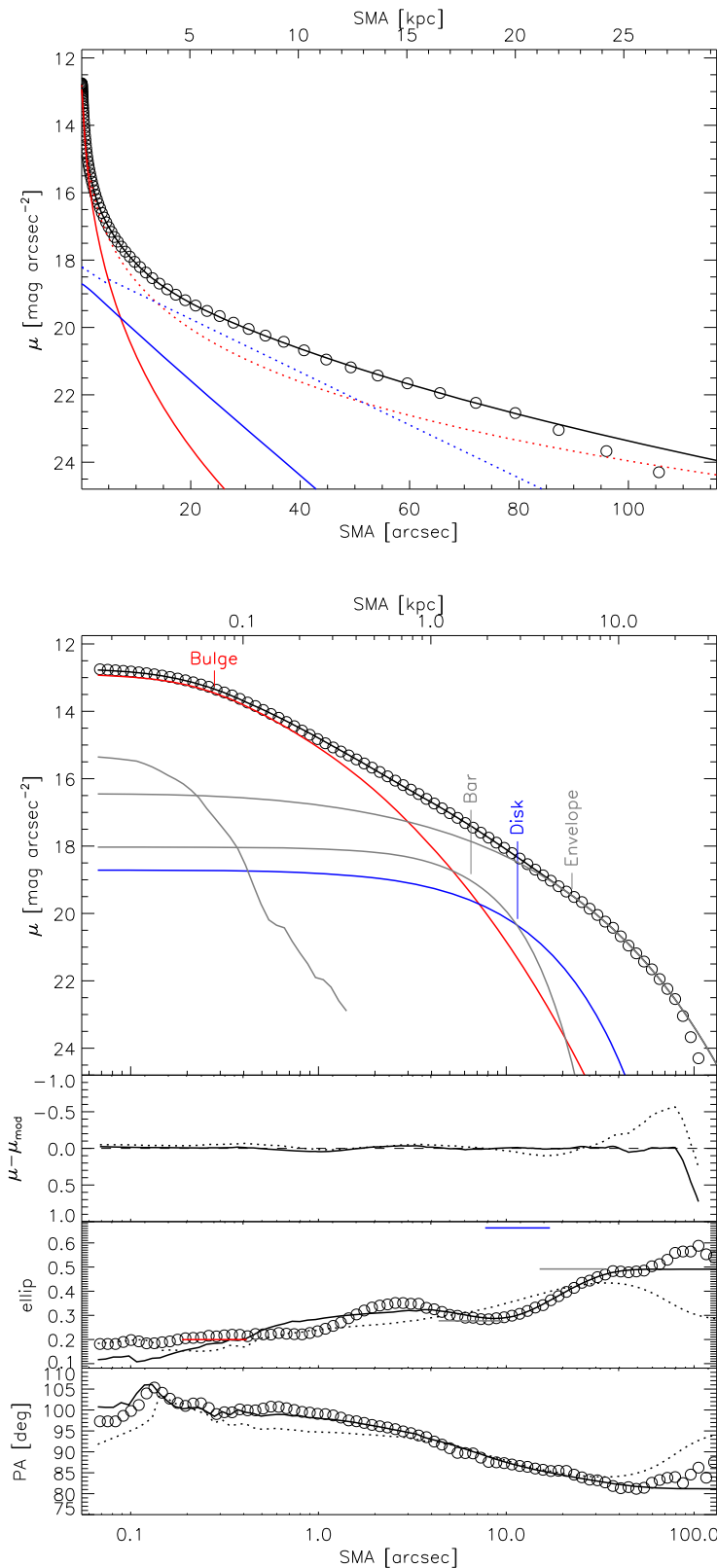
Figure 11. NGC 1194 photometric data and model, with layout as in Figure 9. Left panels: semimajor-axis (SMA) profiles of H-band surface brightness (μ), data-model residuals ($\mu-\mu_{mod}$), ellipticity (ellip), and east-of-north position angle (PA). Open circles: data, solid lines: full model, dashed lines: basic (bulge+disk) model. Thick black: total model image profiles, red: bulge, blue: disk, and thin gray: all other components. Only select profiles are shown in the $\mu-$SMA (top panel) and $\mu-\log$ SMA (second from top) plots (see also Figure 12). Ellipticities of individual components are indicated by horizontal bars. Right panels: images of the data, model and residuals. In the full model, the envelope component is required to allow the point source to be fitted; otherwise, the bulge is too bright in the center with a comparatively high ($n \sim 7$) Sérsic index. It also provides the higher flattening in the outer parts compared to the bulge, which otherwise (in the basic model) dominates the light at $\gtrsim 10$ kpc. The intermediate-scale (~ 2 kpc) component is tentatively termed "bar" here for its compact profile (Sérsic $n \sim 0.8$) and $\sim 90°$ PA offset from the disk major axis. It is strong enough to be required for fitting the disk and envelope separately.
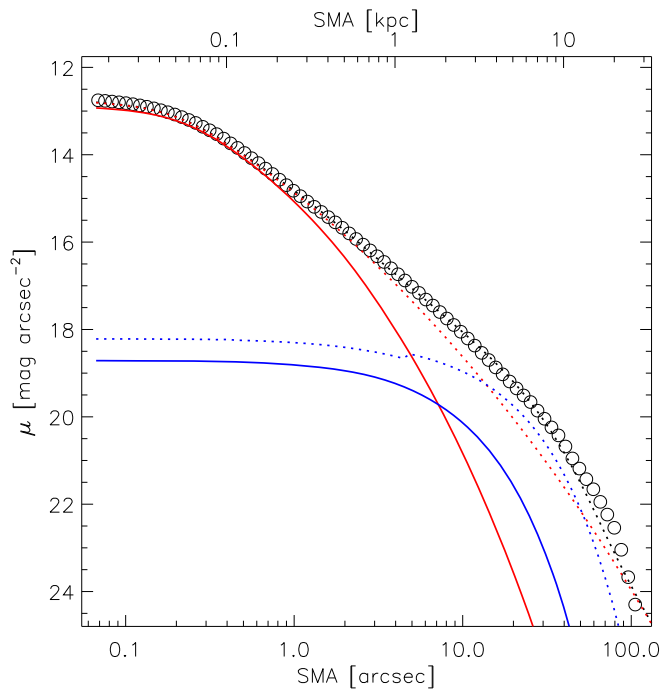
Figure 12. NGC 1194 photometric data and model, continued from Figure 11. Left panel: SMA surface brightness (μ) of the data (open circles), full model (solid lines) and basic bulge+disk model (dashed), separately for total light (black), bulge (red) and disk (blue). Right panel: image of the basic model residuals. In this basic model, which in particular does not include the envelope component, the bulge outer profile is too extended and does not follow the downturn ("knee") at $\sim 80''$ (~ 20 kpc). The excess brightness of the compact "bar," which is slightly elongated along the minor axis (here: vertical orientation) can also clearly be spotted in the basic model residuals, as well as the dust lane parallel to the major axis.

APPENDIX A
DETAILED NOTES ON GALAXY DECOMPOSITIONS

A.1. IC 2560

IC 2560 (Figures 9 and 10) contains a large-scale disk with well-defined spiral arms at intermediate radii. The disk is detectable out to $\sim 150''$ (30 kpc) along the major axis (with PA $= -50°$) and has an axis ratio of ~ 0.6; it grows rounder at larger radii. The tightly wound spiral arms range from 6 to 12 kpc ($30''$–$60''$) and broadly resemble a ring. The central X-shaped bulge/bar dominates the light inside $\sim 10''$ (2 kpc). Finally, the SB profile exhibits a "knee" at $1''$ (0.2 kpc) that corresponds to a nuclear disk.

The spiral ring and X-shaped bulge/bar are apparent in the residuals to the basic bulge+disk model (Figure 10). Thus, in our more complex fit, we introduce one component for the ring and one for the X-shaped bar/bulge. We also include a large-scale (extended) envelope, with a best-fit exponential scale radius of $47''$ (9.5 kpc) to accommodate the obviously rounder outer component. Our best-fit model (Figure 9) also includes a faint nuclear disk that is exposed in the residual image and indicated by profile inflections around $1''$. Although the formal χ^2 improves only marginally when the disk is added, we see spiral structure associated with the nuclear disk in the residual image, and the disk model perfectly fits the apparent knee in the μ-profile at SMA $\sim 1''$ (0.2 kpc). The bulge component changes when the nuclear disk is included, growing by $1''$ (a factor of two) and 0.34 mag, as it is no longer trying to fit the very compact nuclear disk.

In the best-fit model, we fix the Sérsic index of the ring, envelope and nuclear disk to 1, 1, and 0.5, respectively. The ring is modified by an inner truncation. The X-shape is modeled by a fourth-order Fourier mode. Our estimate for the systematic (modeling) error of the classical bulge magnitude is 0.4 mag, which we derive by considering the difference between the best-fit values from our reference model and several alternative models: allowing a free Sérsic index for first the envelope (bulge magnitude unchanged, $n_{env} \to 0.6$), then the nuclear disk ($+0.3$ mag, $n_{nuc.disk} \to 0.8$), and finally the main disk (-0.4 mag, $n_d \to 0.2$). We also construct alternative models by omitting from the model the nuclear disk (bulge $+0.3$ mag), or we omit the X-shaped pseudobulge (-0.6 mag).

Our high-resolution data allows us to cleanly separate the X-shaped bar/bulge from from a nuclear disk and the small, round (possibly classical) bulge. In the low-resolution and shallower *Spitzer* data of Sani et al. (2011), they are clearly
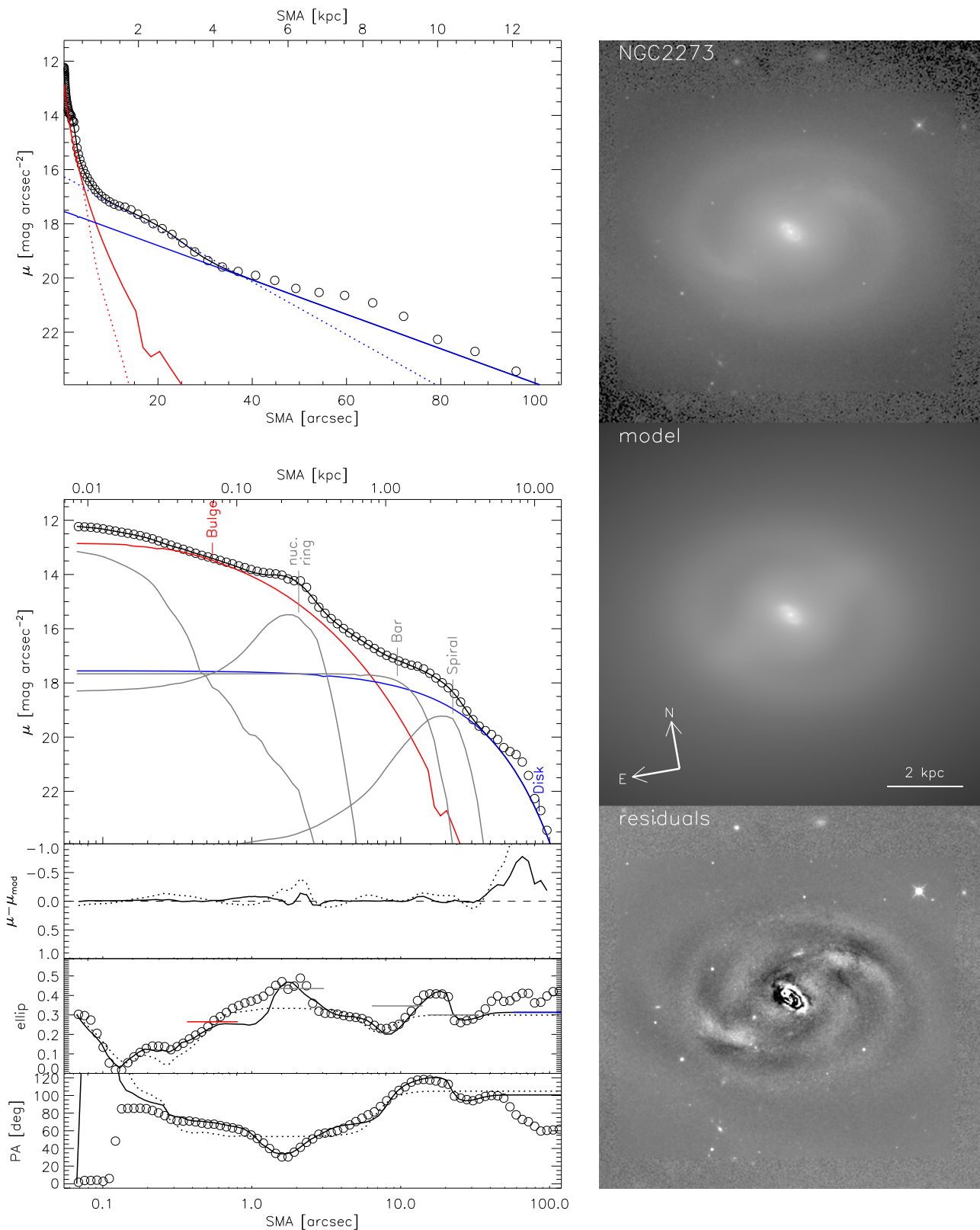
Figure 13. NGC 2273 photometric data and model, with layout as in Figure 9. Left panels: semimajor-axis (SMA) profiles of H-band surface brightness (μ), data-model residuals ($\mu-\mu_{mod}$), ellipticity (ellip), and east-of-north position angle (PA). Open circles: data, solid lines: full model, dashed lines: basic (bulge+disk) model. Thick black: total model image profiles, red: bulge, blue: disk, and thin gray: all other components. Only select profiles are shown in the $\mu-$SMA (top panel) and $\mu-\log$ SMA (second from top) plots (see also Figure 14). Ellipticities of individual components are indicated by horizontal bars. Right panels: images of the data, model, and residuals. The full model traces the data much better than the basic model, in particular regarding ellipticity and PA. It models the spiral arms by a ring with inner truncation, and dispenses with modeling the rotation of the arms as they are too tightly wound for a stable fit. The other prominent features are the bar (Sérsic profile with best fit $n \sim 0.2$) and the nuclear disk and ring, which are both modeled by one component with a Gaussian profile and an inner truncation applied. The outer disk and (faint) spiral structure are not shown on the image area and are not separately modeled as their degeneracy with the main exponential disk is large.
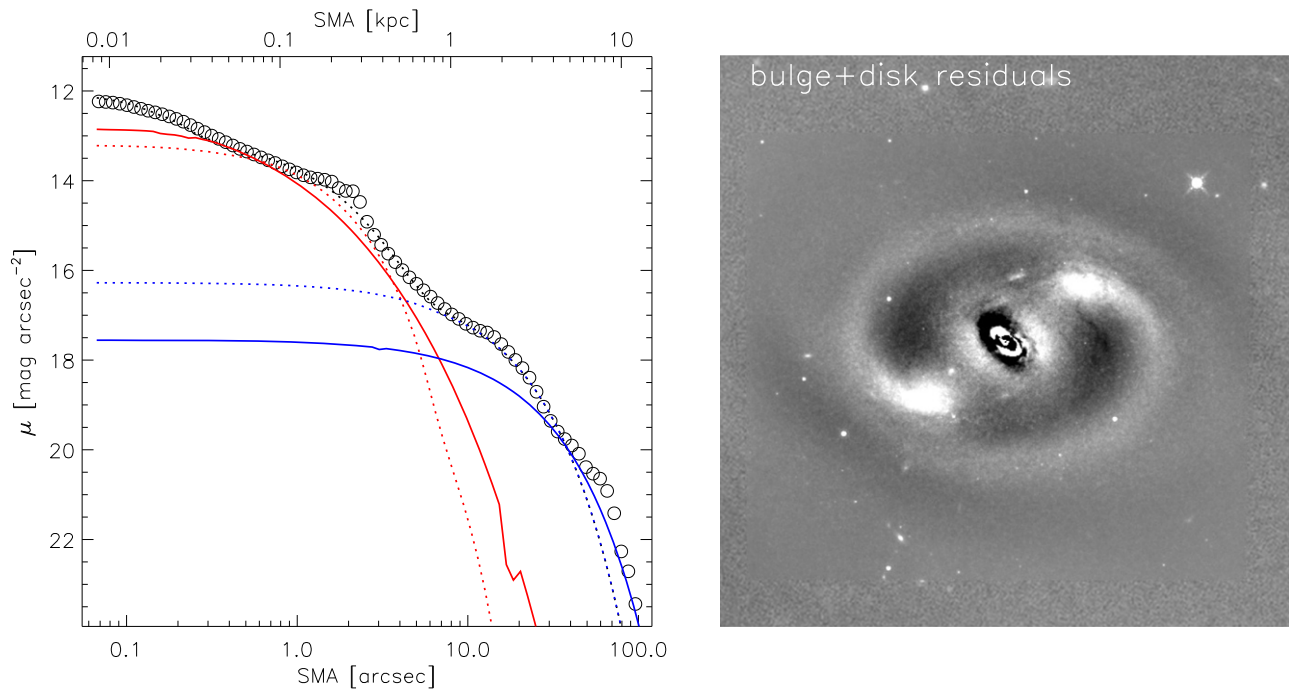
Figure 14. NGC 2273 photometric data and model, continued from Figure 13. Left panel: SMA surface brightness (μ) of the data (open circles), full model (solid lines) and basic bulge+disk model (dashed), separately for total light (black), bulge (red) and disk (blue). Right panel: image of basic model residuals. In both the profiles and residuals it is clear that the basic model cannot account for the nuclear disk (near SMA $\sim 2''$, or ~ 250 pc) and cannot distinguish the extended profile of the main disk from the compact profile of the spiral arms (the "knee" at $\sim 20''/2$ kpc).

fitting the disk and envelope together, since their disk is rounder than their bulge component. Likewise, their bulge component contains multiple components. Overall, they find a B/T of about 0.5, i.e., significantly higher than even the B/T of 0.18 in our basic model.

A.2. NGC 1194

NGC 1194 (Figures 11 and 12) appears to be an S0 seen at relatively high inclination. The innermost region ($\sim 1''$ nucleus) is round, bright, and distinct from the flatter ($q \sim 0.5$) outer regions, which can be visually traced to about $90''$ (20 kpc). The ellipticity profile features a local peak at $\sim 3''$ (~ 0.7 kpc), followed by a trough at $\sim 8''$ (2 kpc). Subtracting the basic bulge+disk model additionally reveals a dust lane that is parallel to the major axis but offset by $\sim 4''$ to the south–west, as well as a minor-axis boxy light excess at $\sim 6''/1.5$ kpc.

Turning to the basic model first, we see that there is no need for an AGN component as the central light is already slightly overestimated by the bulge+disk model. Out to $\sim 1''$, a major-axis excess in residual light may indicate an edge-on nuclear disk, while on larger scales ("$\sim 6''$; Figure 12) we may be seeing the residuals of an end-on bar. There is a local ellipticity peak $\sim 40''$ likely pointing to a disk component. At large radius, the basic model fits the extended light profile with the bulge (leading to a very high Sérsic index $n = 6.8$), but the best-fit bulge is too round to fit the outer component properly and leads to an over-extended profile at large radii compared with the profile in the data.

Our adopted model includes a bar-like component and an "envelope," in addition to a bulge, disk, and point source. The envelope, which has a best-fit Sérsic profile with $n = 2$, reduces the flux excess and axis ratio at the largest scales ($\gtrsim 100''$) compared to the basic bulge+disk model, and reduces the bulge Sérsic index ($n = 3.2$). The envelope is intermediate in

flattening between bulge and disk: $q = 0.5$, versus 0.7 and 0.4, respectively. This outer component is as flattened as the inner disk and carries a large share of the total flux ($\sim 75\%$), so that we surmise that it probably represents a large-scale, thick disk. Supporting this interpretation, there is also a large H I-disk in NGC 1194 (Sun et al. 2013). The bar-like component fits the apparent minor-axis excess on $\sim 10''$ scales. An additional $0.''3(80$ pc)-sized nuclear component can be fit and slightly improves the residuals, but we refrain from including it in our adopted model due to the complicated and dust-obscured center. However, we retain such a model with a nuclear component as an alternative that serves to estimate the systematic modeling errors of the model parameters.

Turning to the systematic errors, we find that the basic bulge is 1.8 mag brighter than the bulge component in our adopted model. If we remove just the envelope from the adopted model, then we obtain a 1.6 mag brighter bulge. Interestingly, if we *add* the putative nuclear component to the adopted model while constraining the envelope Sérsic index to $n = 1$ to reduce degeneracy, we again get a significantly *brighter* bulge than in our adopted model (by 0.8 mag). Conversely, the bulge parameters barely change when we fit the large-scale disk with a Sérsic profile (0.1 mag fainter bulge, and $n_{disk} \rightarrow 0.8$). Finally, we explored whether masking of dust features (central, and particularly the lane parallel to the major axis) alters our results and found virtually no difference in parameters when applying the mask. In summary, these alternative models indicate a systematic bulge magnitude uncertainty of 0.8 mag.

A.3. NGC 2273

NGC 2273 (Figures 13 and 14) is a nearby (26 Mpc) spiral galaxy with several prominent rings and a central disk. Due to the proximity of the galaxy, the inner structure is well-resolved and the galaxy extends $\sim 100''$ on the sky. At the largest radii
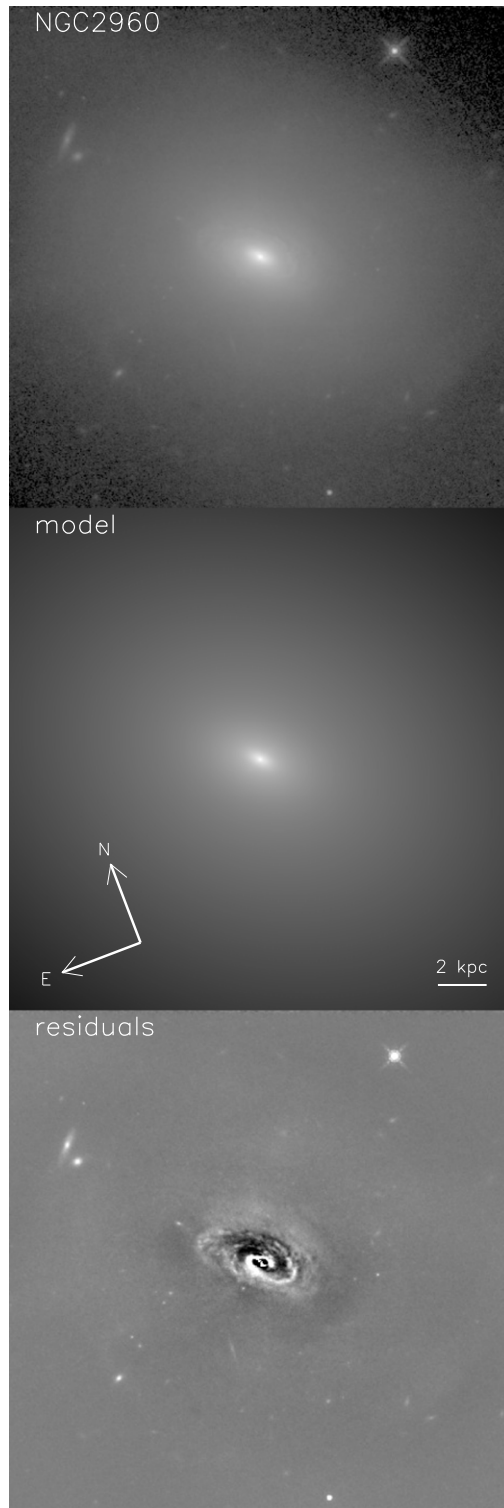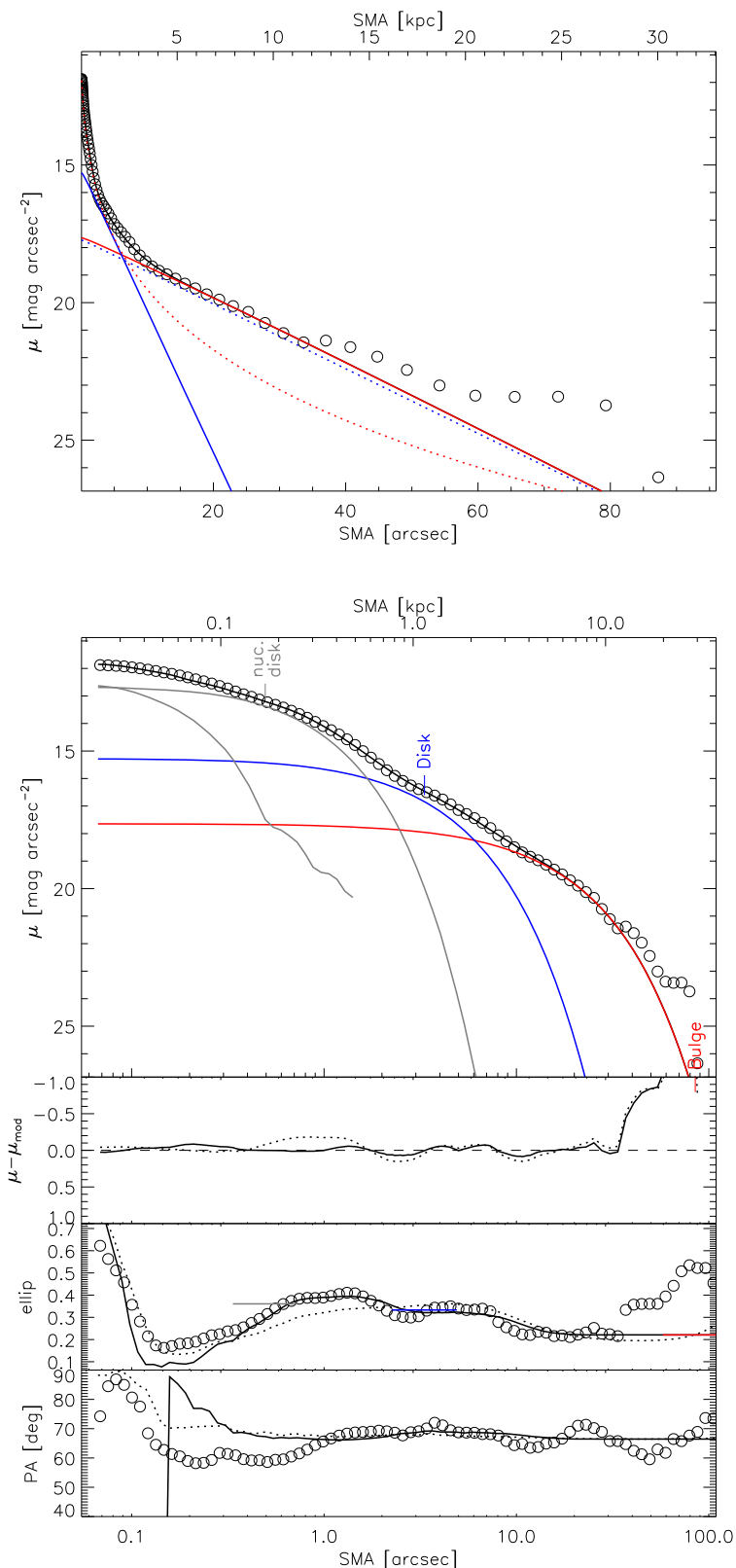
Figure 15. NGC 2960 photometric data and model, with layout as in Figure 9. Left panels: semimajor-axis (SMA) profiles of *H*-band surface brightness (μ), data-model residuals ($\mu-\mu_{mod}$), ellipticity (ellip), and east-of-north position angle (PA). Open circles: data, solid lines: full model, dashed lines: basic (bulge+disk) model. Thick black: total model image profiles, red: bulge, blue: disk, and thin gray: all other components. Only select profiles are shown in the μ−SMA (top panel) and μ−log SMA (second from top) plots (see also Figure 16). Ellipticities of individual components are indicated by horizontal bars. Right panels: images of the data, model and residuals. The steepening of the profile inside ∼13″ (4.5 kpc) apparently signals a bulge, but the increased flattening inside ∼13″ (4.5 kpc), the flocculent spiral arms, the dust lanes and two-part inner profile (inflection at ∼1 kpc) originate in a nuclear (∼100 pc-scale) and kiloparsec-scale star-forming disk that dominate the light in this region. We identify the smooth and round part of the galaxy outside of these two disks as a likely bulge, and surmise that its near-exponential profile (i.e., its relatively low Sérsic index) is a result of a recent merger, which is likely also responsible for the profile distortions and light excess at the largest observable radii (≳50″/6 kpc).
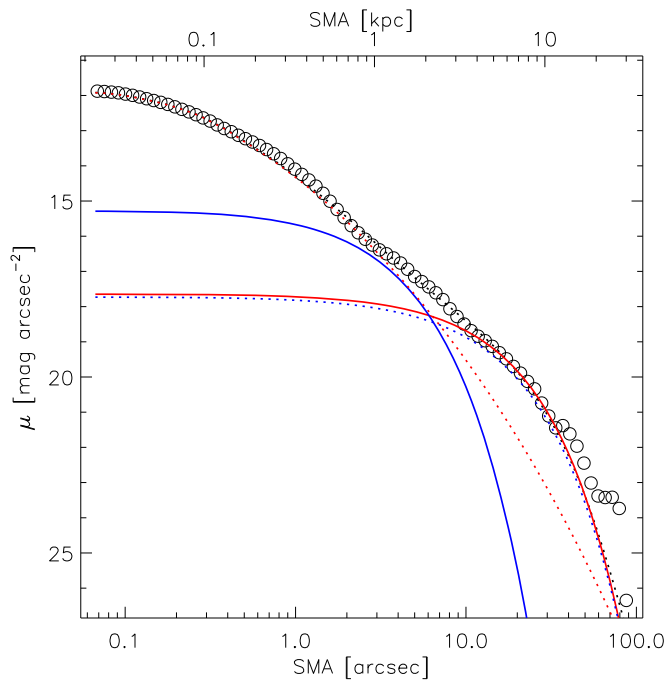
Figure 16. NGC 2960 photometric data and model, continued from Figure 15. Left panel: SMA surface brightness (μ) of the data (open circles), full model (solid lines) and basic bulge+disk model (dashed), separately for total light (black), bulge (red) and disk (blue). Right panel: image of basic model residuals. The nuclear and kiloparsec-scale star-forming disk are clearly evident in the basic model residuals.

(SMA $\gtrsim 60''/7.5$ kpc), the light distribution is flattened ($q \sim 0.6$) with a major-axis PA of about $140°$ E of N. The ends of the spiral arms are also visible. Further inward, the arms dominate the light. They are tightly wound, forming a broad ring at $10''$–$20''$ (1.3–2.5 kpc) along the SMA. The ellipticity of the ring is lower than that of the outer disk, and the PA is misaligned by about $+40°$ from the outer disk. The spiral arms emerge from opposite sides of an apparent bar, which thickens to become lens-like toward the center. Located well inside this bar/bulge region at SMA $= 2''$ (250 pc) is a bright and slightly asymmetric nuclear ring and disk (Mulchaey et al. 1997; Erwin & Sparke 2003; Gu et al. 2003) with PA and axis ratio similar to the outer disk (see also, Petitpas & Wilson 2002; Barbosa et al. 2006; Falcón-Barroso et al. 2006). In the galaxy center, near the resolution limit, the brightness rises steeply. This feature appears round and is $1''$ (130 pc) in diameter. It is either an inner bulge or a barely resolved star cluster.

Starting with a basic bulge+disk+psf model (Figure 1), the best-fit bulge component traces the light of the nuclear ring, while the disk component broadly accounts for the main spiral arms. We improve on the basic model by adding a nuclear ring, bar, and spiral arms (Figure 2). We find a Gaussian profile with inner truncation for the nuclear ring and the spiral component. This choice fits the data better than an exponential and avoids the degeneracy of the more general Sérsic profile in the presence of the simultaneously adjustable truncation parameters. The bar component is a Sérsic with $n \sim 0.2$ and boxy isophotes (Fourier amplitude $a_4 = -0.1$), as expected. The bulge and nuclear disk components are oriented along the (outer) major axis ($\sim 50°$ E of N), while the bar component is rotated by a relative $+80°$. The large-scale disk provides a good fit beyond $\gtrsim 20''$ (2.5 kpc) aside from an additional faint large-scale spiral arm/ring pattern, which cannot be robustly modeled.

We bracket systematic uncertainties in our reference model with three additional models. Replacing the exponential disk by a Sérsic profile leads to a 0.2 mag reduction in the classical bulge light, and the disk index of $n = 1.5$ shows that the corresponding component indeed traces the exponential part of the profile. We test the effect of removing the bar, which was visually confluent with the bulge, and obtain a 0.6 mag increase in bulge flux. In this modification, the classical bulge R_e increases by a factor of two, becomes steeper ($n = 3.8$ versus the reference $n = 2.1$), and effectively accounts for most of the light inside the spiral ring. However, this model without a bar results in strongly increased residuals, and we thus prefer to include the bar. Finally, we test using a Sérsic profile for the nuclear ring and model a nuclear disk instead of the ring. We find virtually unchanged classical bulge parameters, but significantly elevated residuals in the latter case. The resulting low Sérsic index (0.1) of the disk also suggests that an inner truncation is appropriate to model the nuclear disk. In conclusion, we arrive at a conservative systematic uncertainty of 0.4 mag for the classical bulge magnitude of NGC 2273.

A.4. NGC 2960

NGC 2960 (Figures 15 and 16) is a bulge-dominated galaxy with a kiloparsec-scale embedded disk. Its SMA is oriented $150°$ east of north, and the average flattening is rather low, $q \sim 0.7$. The radial SB profile appears to exhibit a bulge-disk structure of a typical lenticular galaxy, with a prominent steepening of the profile inside $\sim 13''$ (4.5 kpc) and an exponential decline outside. However, two salient features distinguish NGC 2960 visually from a simple lenticular: the increase of ellipticity toward the center, and an inner (SMA $\sim 8''/2.7$ kpc) flocculent and dusty disk. The residual image of a basic bulge+disk model (Figure 15) reinforces the impression of a dusty disk and reveals embedded asymmetric spiral structure. The residual image also shows that a highly
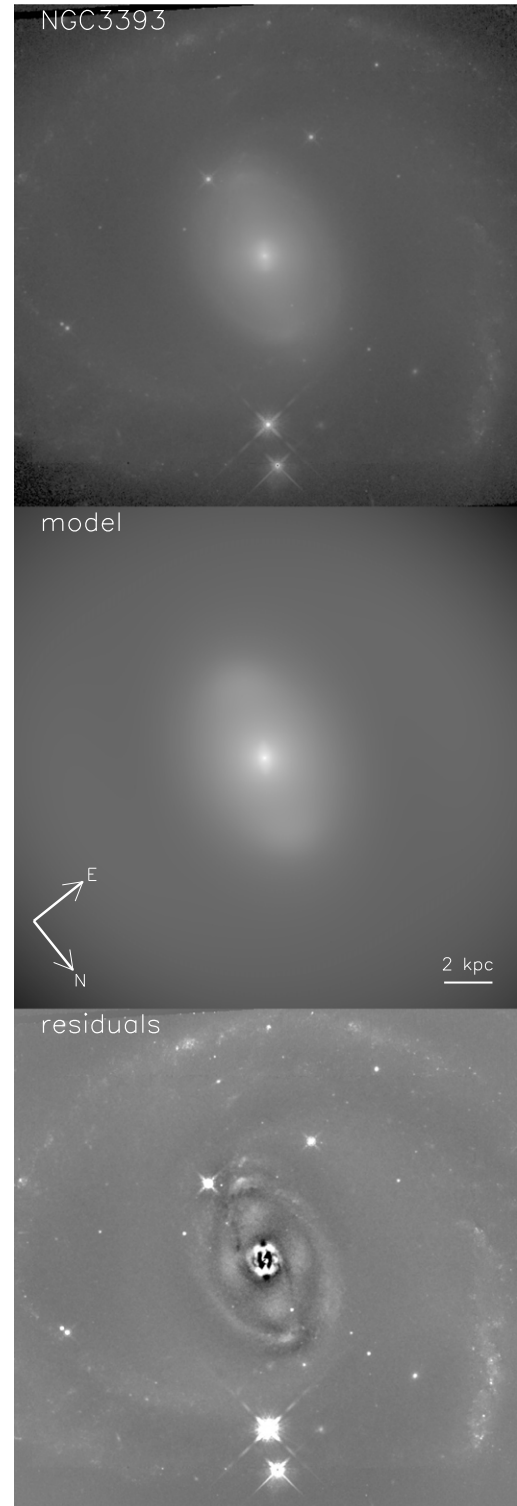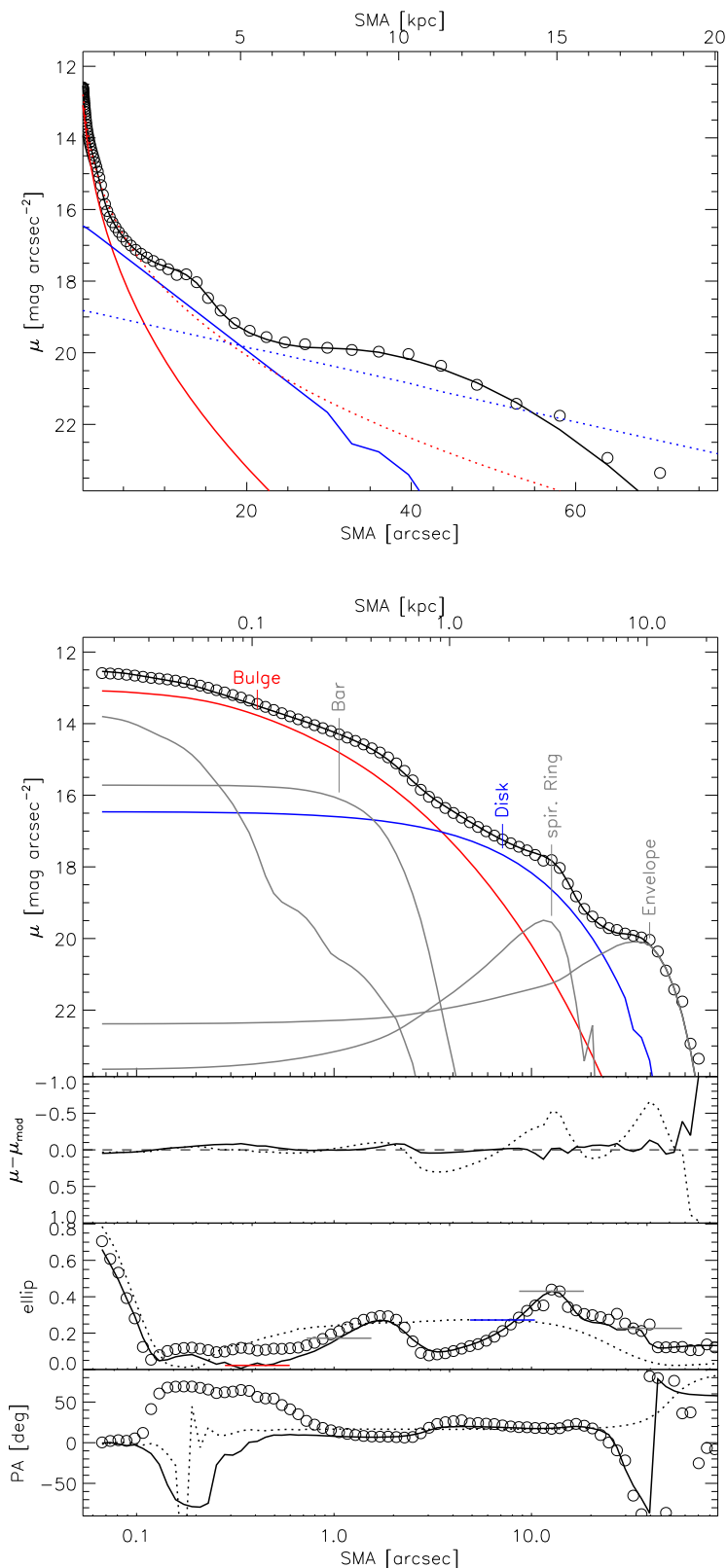
Figure 17. NGC 3393 photometric data and model, with layout as in Figure 9. Left panels: semimajor-axis (SMA) profiles of *H*-band surface brightness (μ), data-model residuals ($\mu - \mu_{mod}$), ellipticity (ellip), and east-of-north position angle (PA). Open circles: data, solid lines: full model, dashed lines: basic (bulge+disk) model. Thick black: total model image profiles, red: bulge, blue: disk, and thin gray: all other components. Only select profiles are shown in the μ–SMA (top panel) and μ–log SMA (second from top) plots (see also Figure 18). Ellipticities of individual components are indicated by horizontal bars. Right panels: images of the data, model and residuals. In addition to bulge, disk and central point source, the full model features all major visible structures: the nuclear bar ($\sim$500 pc scale) oriented $\sim$$-35°$ E of N (roughly vertical on the shown image); the bright elongated ring, which appears to delineate the boundary of a $\sim$3 kpc bar; and an outer round ring (flattening near zero) which appears to consist of weakly defined and tightly wound low-surface brightness spiral arms and marks the boundary of the visible disk (seen in the corners of the field shown here). Both rings have a Gaussian profile and an inner truncation. The residuals suggest an additional nuclear ring that touches the ends nuclear bar, but it is not separately modeled due to ensuing excessive model degeneracy.

29
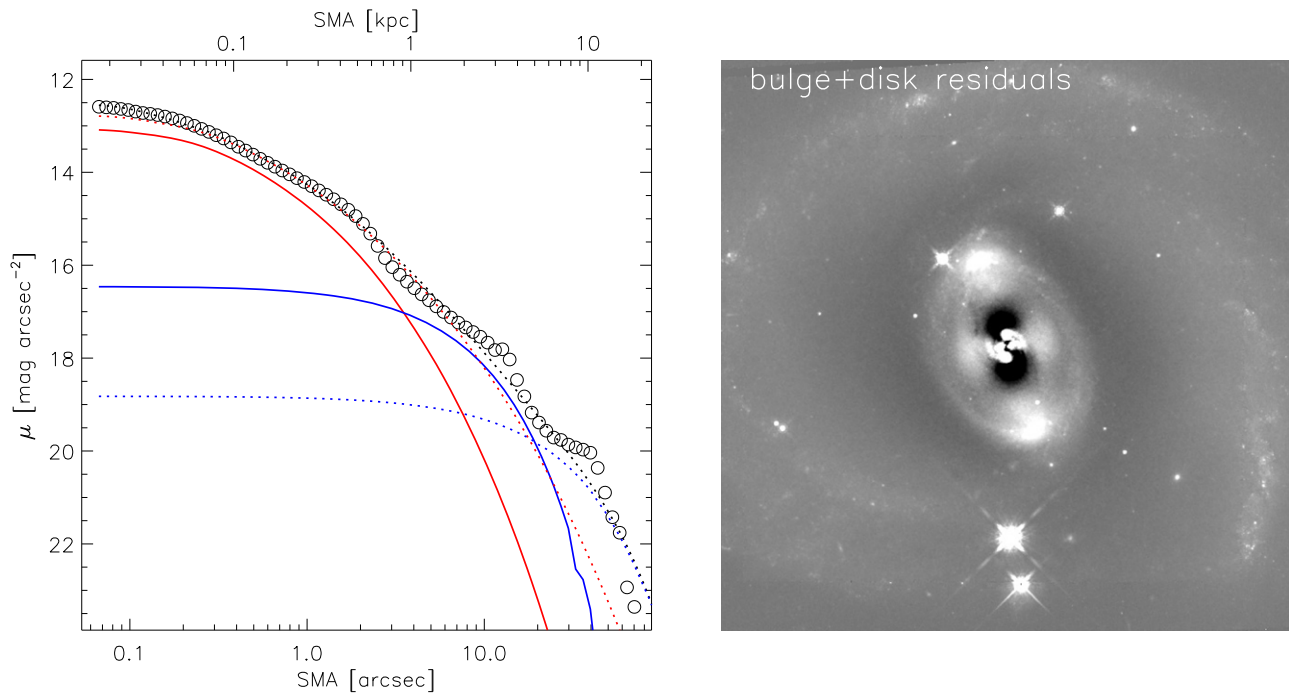
Figure 18. NGC 3393 photometric data and model, continued from Figure 17. Left panel: SMA surface brightness (μ) of the data (open circles), full model (solid lines) and basic bulge+disk model (dashed), separately for total light (black), bulge (red) and disk (blue). Right panel: image of basic model residuals. The inability of the basic model to represent the galaxy light is evident, and the basic model residual image exposes both the intermediate ring (elongated) and the outer ring (round, faint spiral structure). The nuclear bar is not clearly visible here, but indicated still by the central isophotal twist.

inclined nuclear disk (residuals at SMA $\lesssim 1\farcs5/500$ pc) is responsible for the low ellipticity at the smallest radii. Both the nuclear disk and the kiloparsec-scale disk are indicated by separate ellipticity peaks ($e \sim 0.4$ respectively) at radii corresponding to their visual dominance.

By contrast, the dominant large-scale (outermost) component is round ($q \sim 0.8$), smooth, and morphologically resembles an elliptical galaxy. We thus might interpret this large-scale component as the bulge despite its exponential profile. At the largest radii at which the light distribution can be traced, from $80''$ (30 kpc) to $30''$ (10 kpc), the profile again flattens and is marked by tidal or shell-like features that can be seen even in the science frames. These features indicate that NGC 2960 has undergone a recent interaction or merger which may have distorted the radial brightness profile of the bulge, resulting in a mostly exponential shape with a marked upturn only at the largest radii.

The basic bulge+disk model includes a flat "bulge" that over-predicts the central flux. To extract the bulge parameters more reliably, and to account for the disks, we add an additional nuclear component with a Sérsic profile (Figure 15). Both inner components converge to relatively compact profiles ($n = 1.4$ and 0.5). The comparison of this four-component model with the data profile makes it clear that both inner components trace the light of nuclear and kiloparsec-scale disk, and that the inner region is reasonably fit by these two components alone. We have also explored models with an additional central bulge, resulting in five components (including the central point source). However, the residuals barely improve, and the corresponding "bulge" component is still significantly flatter ($q = 0.6$) than the large-scale outer profile. We thus do not include this additional component. We have also accounted for the outermost, very flattened light by a separate component, but find that its inclusion does not affect the parameters of the other components.

Given these many complications, we do not find a clear classical bulge component in NGC 2960; instead, the center is fit by the sum of the two disks. We judge that the third, large-scale component corresponds best to a classical bulge, even with a low best-fit Sérsic $n \sim 1$. For comparison, Vika et al. (2012) have fit a two-component model, and interpreted the inner component as the bulge, which, given its size, presumably fits both the nuclear and the kiloparsec-scale disk simultaneously, and hence is more flattened than the outer component (the "disk" in their interpretation). The Vika et al. (2012) model hence corresponds to our basic model, which does not account for the separation of the two inner components and their clear disk morphology. We speculate that the kiloparsec-scale disk was recently accreted, and thus still contains gas and spiral structure. If we take one or both of the inner disks as the "bulge" instead, then the magnitude drops by 0.4–1.4 mag. Other modifications, like allowing a Sérsic instead of an exponential profile for either disk, or including an envelope, have comparatively minor effects on the bulge parameters. The alternative models provide us with a 0.6 mag estimate of the systematic bulge magnitude uncertainty.

A.5. NGC 3393

NGC 3393 (Figures 17 and 18) is a late-type galaxy that contains two prominent rings. It is probably seen face on based on the round outer disk, which extends to $\sim80''$ (21 kpc). The large-scale disk is slightly lopsided toward $-50°$ E of N, and features two asymmetric spiral arms with prominent star-forming regions. The arms barely connect to the galaxy center and broadly resemble a ring, which is clearly indicated by the
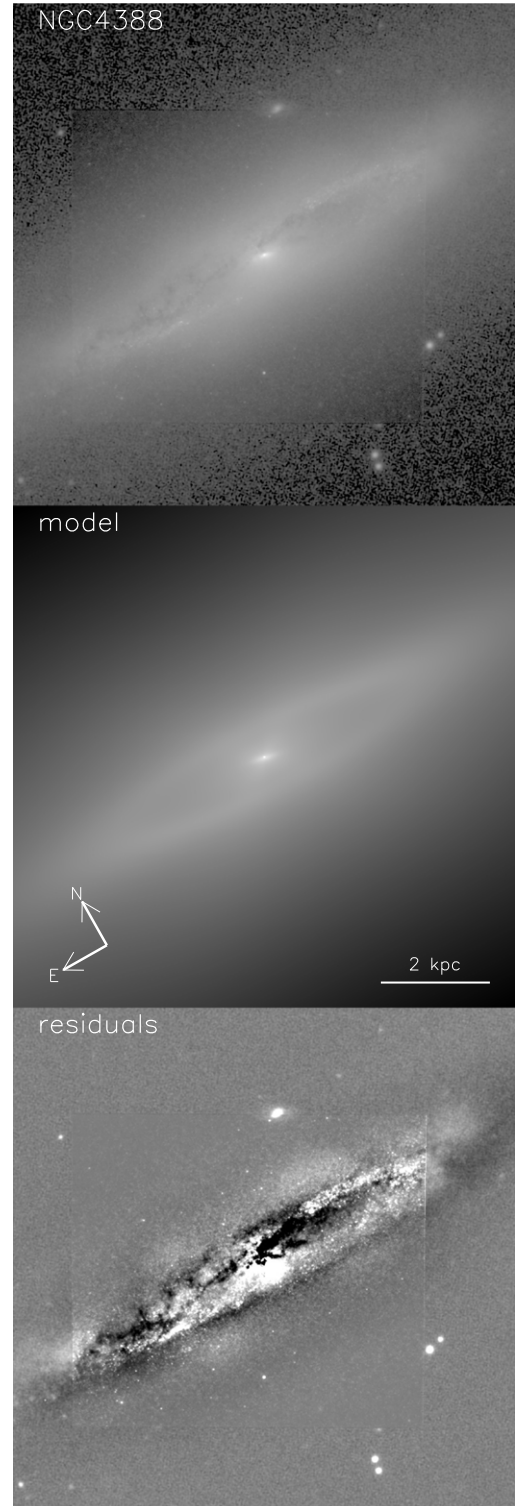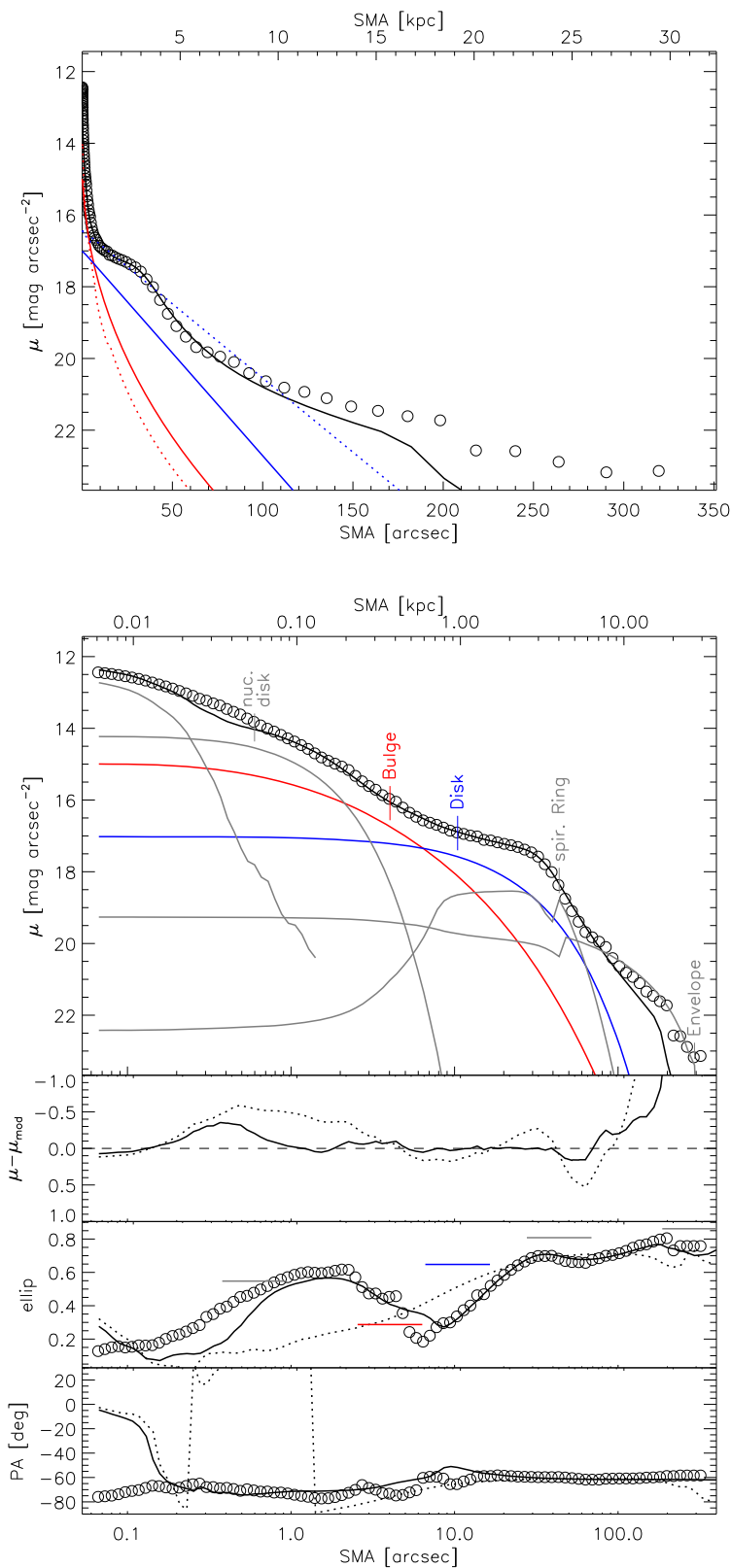
Figure 19. NGC 4388 photometric data and model, with layout as in Figure 9. Left panels: semimajor-axis (SMA) profiles of *H*-band surface brightness (μ), data-model residuals ($\mu-\mu_{mod}$), ellipticity (ellip), and east-of-north position angle (PA). Open circles: data, solid lines: full model, dashed lines: basic (bulge+disk) model. Thick black: total model image profiles, red: bulge, blue: disk, and thin gray: all other components. Only select profiles are shown in the μ–SMA (top panel) and μ–log SMA (second from top) plots (see also Figure 20). Ellipticities of individual components are indicated by horizontal bars. Right panels: Images of the data, model and residuals. The full model accounts for the nuclear disk, spiral arms, and outer disk (envelope) with exponential profiles, where the spiral arms component is modeled as a ring. The innermost profile is partially underpredicted, but corresponding models accounting for it by an additional component proved too degenerate, and dust in the center prevents a more accurate interpretation of the inner structure based on our image.
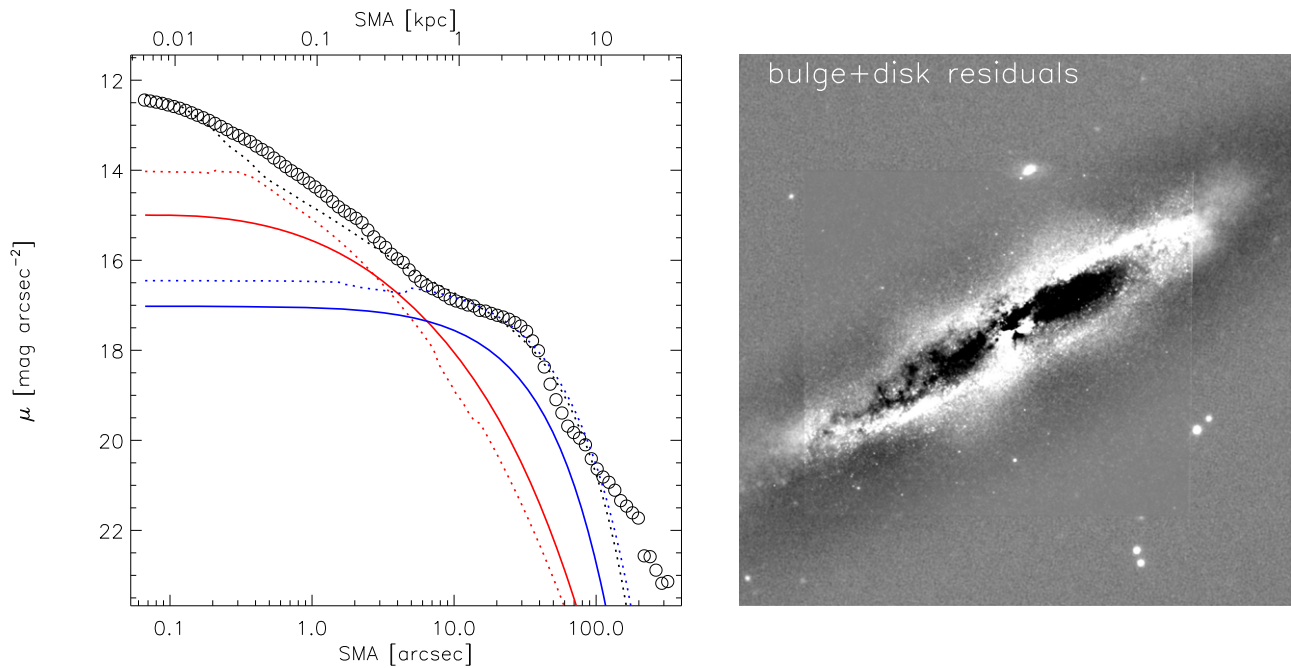
Figure 20. NGC 4388 photometric data and model, continued from Figure 19. Left panel: SMA surface brightness (μ) of the data (open circles), full model (solid lines) and basic bulge+disk model (dashed), separately for total light (black), bulge (red) and disk (blue). Right panel: image of basic model residuals. The basic model residuals clearly expose the spiral arms, which wind tightly to nearly form a ring, as well as the thin (inclined) central nuclear disk and intervening dust lanes at all radii.

peak in the SB profile at $40''/10$ kpc. The inner ring at intermediate radii (SMA $= 13''/3.5$ kpc) is much more elongated and has a lower axis ratio than the outer disk. The ring might be the star-forming boundary of a large-scale bar. The innermost region ($\lesssim 2''/0.5$ kpc) appears to be dominated by the bulge, i.e., a steep increase in the SB and round isophotes. It harbors yet another bar-like light distribution, with a PA $140°$ E of N which is misaligned by $-20°$ from the major axis defined by the inner ring.

Fitting and removing the basic model (bulge+disk+nucleus, see Figure 18) exposes residuals from the bar and each ring. The basic fit yields an extended ($6''.4/1.6$ kpc and $n = 3.5$) "bulge" component that effectively accounts for all of the light at and inside the inner ring and is more flattened ($q = 0.7$) than the outer disk.

We improve the NGC 3393 model by adding separate components for the central bar and both rings. With $n = 0.25$ and $q = 0.4$, the bar is compact and flattened, as expected. We model the rings with Gaussian profiles ($n = 0.5$) but use an inner truncation so that the ring light does not eat away the disk. This, our best-fit model, has classical bulge parameters $m = 11.2$ mag, $R_e = 2''.4$ (0.6 kpc), $n = 2.6$, and $q = 0.97$. This is 1 mag fainter than the bulge in the basic bulge+disk model, and 0.2 mag brighter than for the intermediate model without truncations. We adopt this difference as a rough estimate of the systematic bulge magnitude uncertainty.

A.6. NGC 4388

NGC 4388 (Figures 19 and 20) is a spiral galaxy seen at high inclination (disk $q = 0.35 \rightarrow i \gtrsim 70°$). The tightly wound spiral arms are visually defined between SMA $\sim 30''$ and $50''$ (2.8 and 4.6 kpc). They form a ring that can be identified in the SB and ellipticity profiles. In the center of NGC 4388, there is a bright, central ($\lesssim 2''.5/200$ pc) disk, seen almost edge-on with

very low axis ratio, and at a $\sim -15°$ misalignment from the large scale major axis. The entire region interior to the ring contains several dust lanes. Outside of the spiral/ring, the profile has two nearly exponential parts, with a change to a larger-scale radius (factor of several) and ellipticity (by ~ 0.2) occurring at $\sim 80''$ (7 kpc). We identify the inner exponential as the main disk, while the outer exponential "envelope" is identified as a very extended disk due to its high flattening ($q \sim 0.1$) and $\sim 100''$ (9 kpc) scale radius.

In addition to the bulge, disk, and nucleus (point source), we account for the nuclear disk, spiral arms, and envelope with exponential profiles. The spiral arms are modeled as a ring with an inner truncation. To reduce degeneracy, we chose an exponential instead of a Sérsic profile for the spiral ring, and force the bulge, disk, and envelope to share a common PA. The best-fit bulge of our adopted reference model is very round ($q \sim 0.8$, compared to the disk $q \sim 0.3$), has an intermediate Sérsic index $n = 2.2$, and boxy isophotes. The nuclear disk dominates the SB in the center, and the PA of the model component converges to the observed value, which provides confirmation that this component is suitably accounted for in our adopted model (see also the discussion of the nuclear disk from the kinematics as observed by SINFONI in Greene et al. 2014). The outer envelope also makes a significant difference to the fit in this case, changing the bulge magnitude by -0.5 mag.

Of the various models we fit, we note here the model with a Sérsic profile (instead of exponential) for the nuclear disk, a Sérsic for the main disk, and a model without the envelope component. These result in classical bulge magnitude changes of $+0.7$, -0.3, and -0.5 mag, respectively, and lead to a systematic bulge magnitude uncertainty estimate of 0.5 mag. For reference, the classical bulge in the best-fit bulge+disk +point-source model is 0.3 mag fainter than in our adopted six-component model.
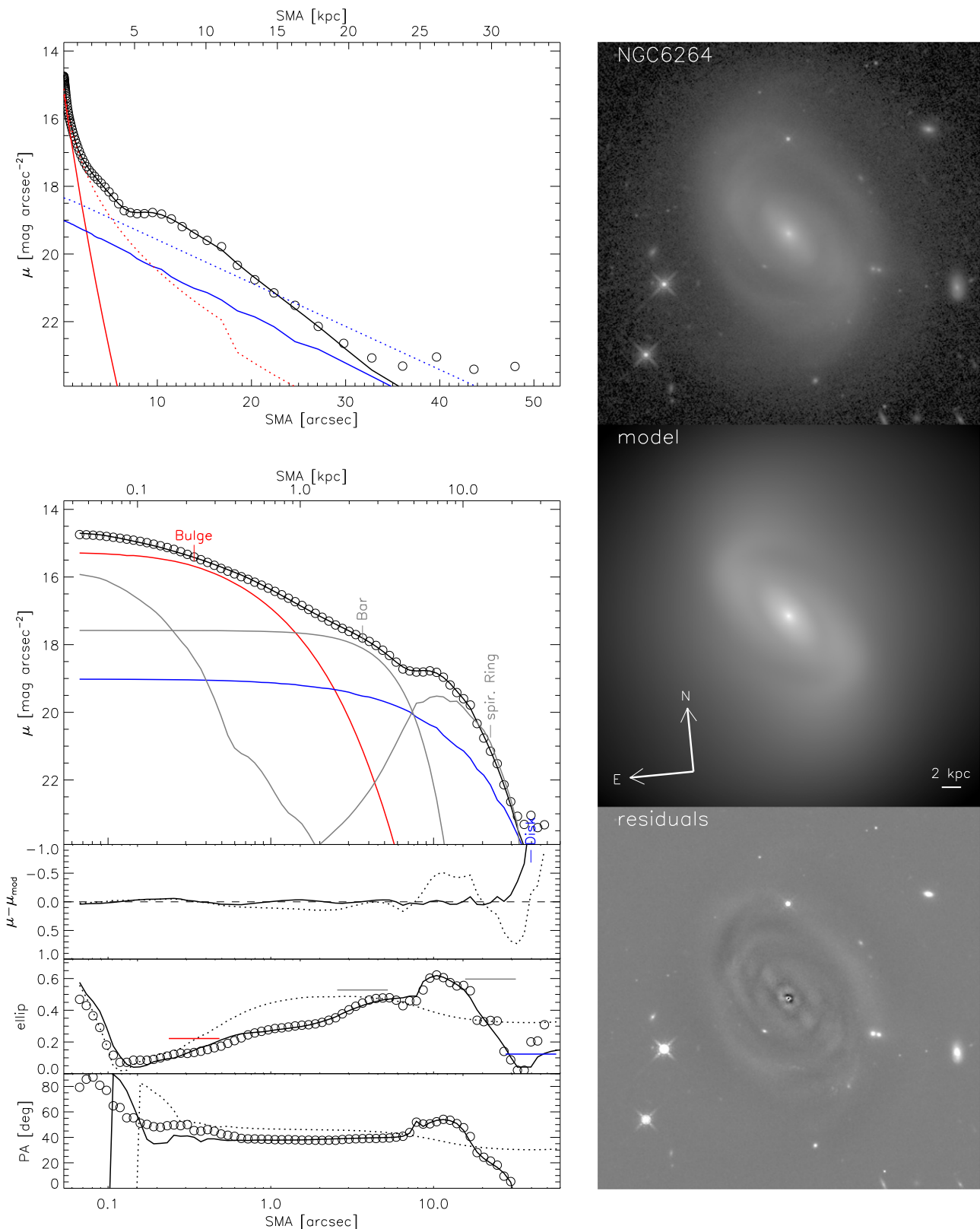
Figure 21. NGC 6264 photometric data and model, with layout as in Figure 9. Left panels: semimajor-axis (SMA) profiles of *H*-band surface brightness (μ), data-model residuals ($\mu-\mu_{mod}$), ellipticity (ellip), and east-of-north position angle (PA). Open circles: data, solid lines: full model, dashed lines: basic (bulge+disk) model. Thick black: total model image profiles, red: bulge, blue: disk, and thin gray: all other components. Only select profiles are shown in the μ–SMA (top panel) and μ–log SMA (second from top) plots (see also Figure 22). Ellipticities of individual components are indicated by horizontal bars. Right panels: Images of the data, model and residuals. The non-axisymmetric structure of NGC 6264 is produced by the bar and spiral arms, which we model by a compact (best fit $n = 0.47$) Sérsic and an exponential profile with both inner truncation and coordinate rotation, respectively. The bulge and bar profiles largely overlap and thus are somewhat degenerate, however their very different axis ratios and the steep profile in the center justify two seperate components here.

33
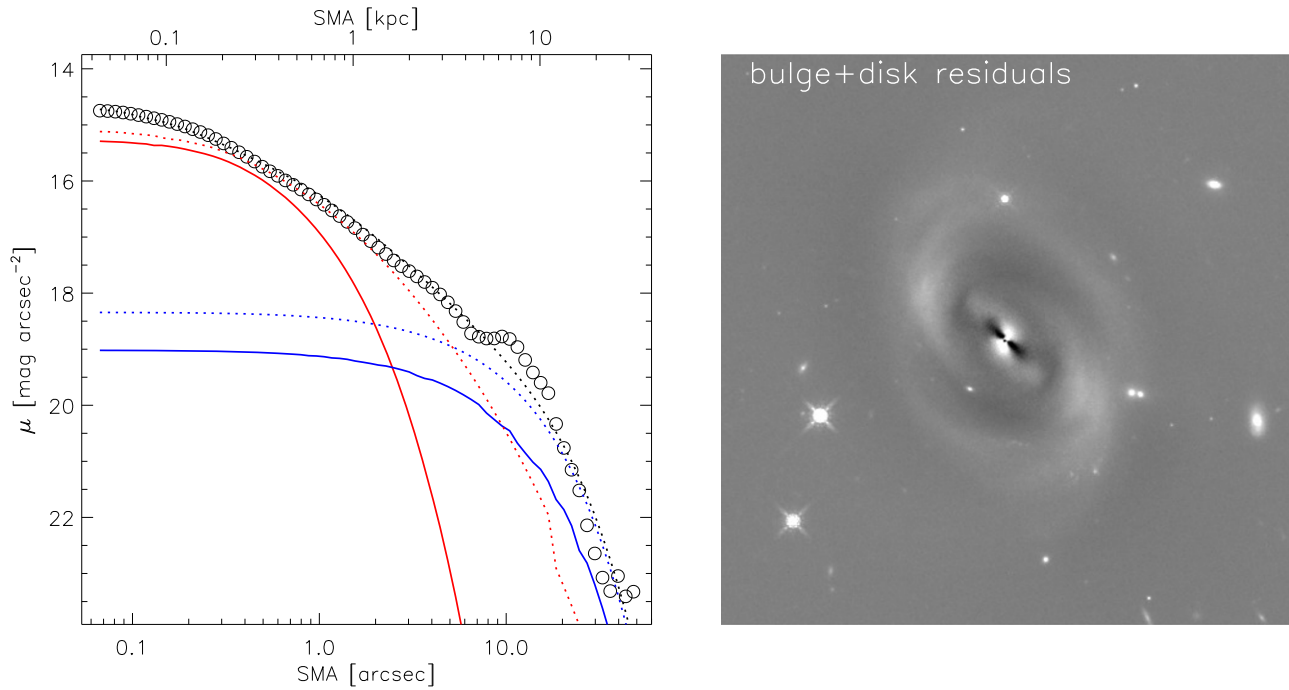
Figure 22. NGC 6264 photometric data and model, continued from Figure 21. Left panel: SMA surface brightness (μ) of the data (open circles), full model (solid lines) and basic bulge+disk model (dashed), separately for total light (black), bulge (red) and disk (blue). Right panel: image of basic model residuals, which clearly exhibits the central bulge as distinct from the bar.

A.7. NGC 6264

NGC 6264 (Figures 21 and 22) is dominated by a bar and a pair of smooth spiral arms. A distinct bulge is not immediately visible, but there is a small ($\sim0\rlap{.}''3/200$ pc) and round central light concentration embedded within the conspicuous bar. The bar is also apparent in the local maximum around $5''$ (3 kpc) in the SB and ellipticity profiles at constant PA. Within $\sim5''$ (350 pc), the PA profile shows a $\sim10°$ step, and grows considerably rounder toward smaller radii, suggesting that we are seeing an underlying bulge.

The spiral arms are smooth and show little signs of star formation, perhaps due to the decreased spatial resolution (~100 pc at the distance of 136 Mpc). The tightly wound spiral arms emerge from the ends of the bar, then become clearly defined at larger radii, and obtain full strength around SMA $\sim10''$ (7 kpc). This region is marked by a local maximum in the SB, ellipticity, and PA profiles, followed by a rapid brightness drop toward larger radii. At $\sim30''$ (20 kpc), the SB profile transitions into a faint (~23 mag arcsec^{-2}) floor that we interpret as an envelope or halo that is traceable out to $50''$ (35 kpc).

When fit with a basic model (bulge, disk, and point source), the "bulge" component is more flattened than the "disk" and appears to predominantly fit the light of the bar. Round residuals near the center expose an underlying rounder light distribution, i.e., the probable bulge. We add another Sérsic component to directly model the bar. The residuals in this second fit are greaty improved and we find a small bulge component ($R_e = 1''/0.7$ kpc, $q = 0.7$), and a larger flat ($R_e = 4''/2.6$ kpc, $q = 0.4$) and compact (Sérsic $n = 0.5$) component, as expected for a bulge and a bar. Using an exponential profile with inner truncation and power-law rotation, we model the spiral arms and the underlying exponential disk component. The adopted $4 + 1$-component

model (bulge, disk, bar, spiral, plus the nuclear point source) is a good fit aside from a possible outer envelope (or halo), which was too faint to be fit robustly. We choose not to account for the latter by another component, as it converges to a very large ($R_s = 100''/70$ kpc) scale, which suggests a degeneracy with the background uncertainty.

We experimented with alternatives to this adopted model and quote the change of bulge magnitude incurred by some of these modifications. Using a Sérsic instead of an exponential profile for the disk, or adding an exponential component for the envelope (halo), results in a 0.4 and 0.2 mag fainter bulge, respectively. Modeling the bar and bulge with only one Sérsic profile, but retaining the spiral component apart from the disk and AGN leads to a much brighter bulge (-1.9 mag) with classical bulge parameters that are close to those of the basic model parameters and differ by -1.4 mag in m_{bul} from the reference model. As a conservative estimate, we thus assign a bulge magnitude uncertainty of 0.7 mag.
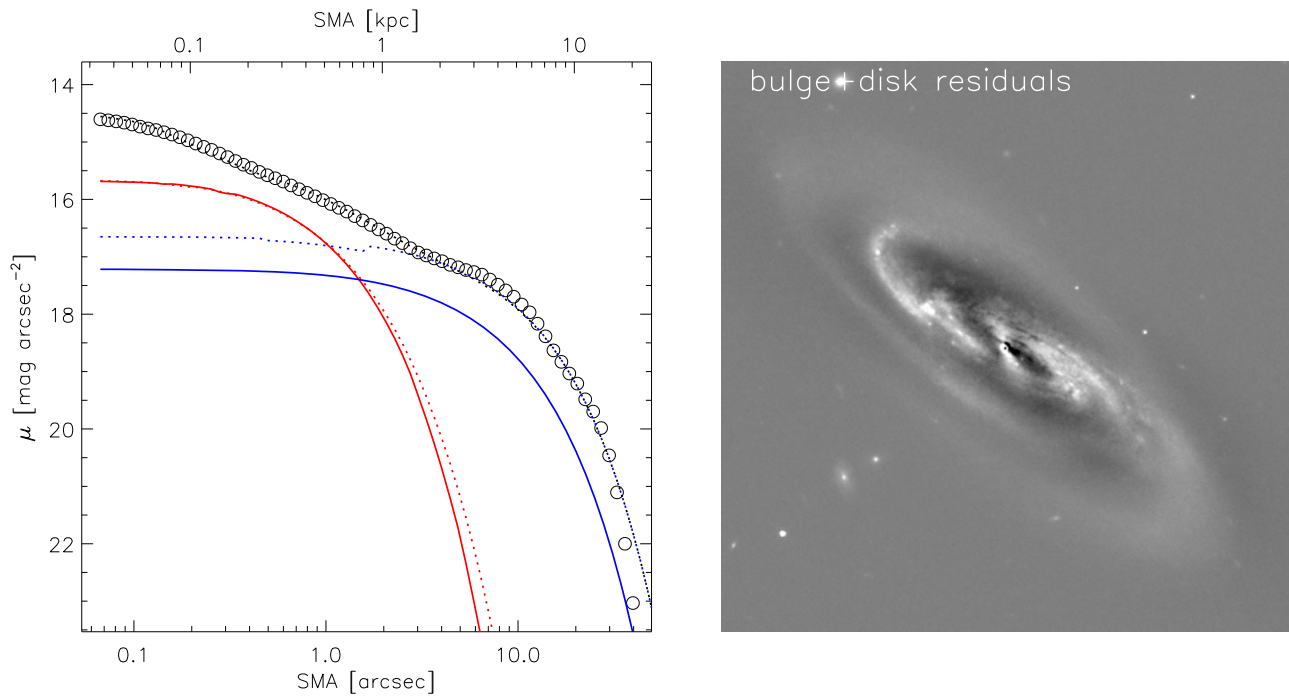
A.8. NGC 6323

NGC 6323 (Figures 23 and 24) is a spiral galaxy at high inclination with an apparent disk axis ratio of ~0.4. There is a ring at SMA $= 8''$ (4 kpc), from which two flocculent and unequal-strength spiral arms emerge and extend to SMA ≈ 10 kpc from the center. The main disk profile exhibits a weak truncation at SMA > 20 kpc that is recognizable in the image as the visible boundary of the disk. An inner (4 kpc) ring is clearly seen in the SB profile, delineating the transition from a low-ellipticity, bulge-dominated inner region to a flatter disk-dominated region. A nucleus or small bulge can be distinguished visually within the inner two arcseconds.

The basic bulge+disk+nucleus model fares surprisingly well when emulating the radial profile. However, significant
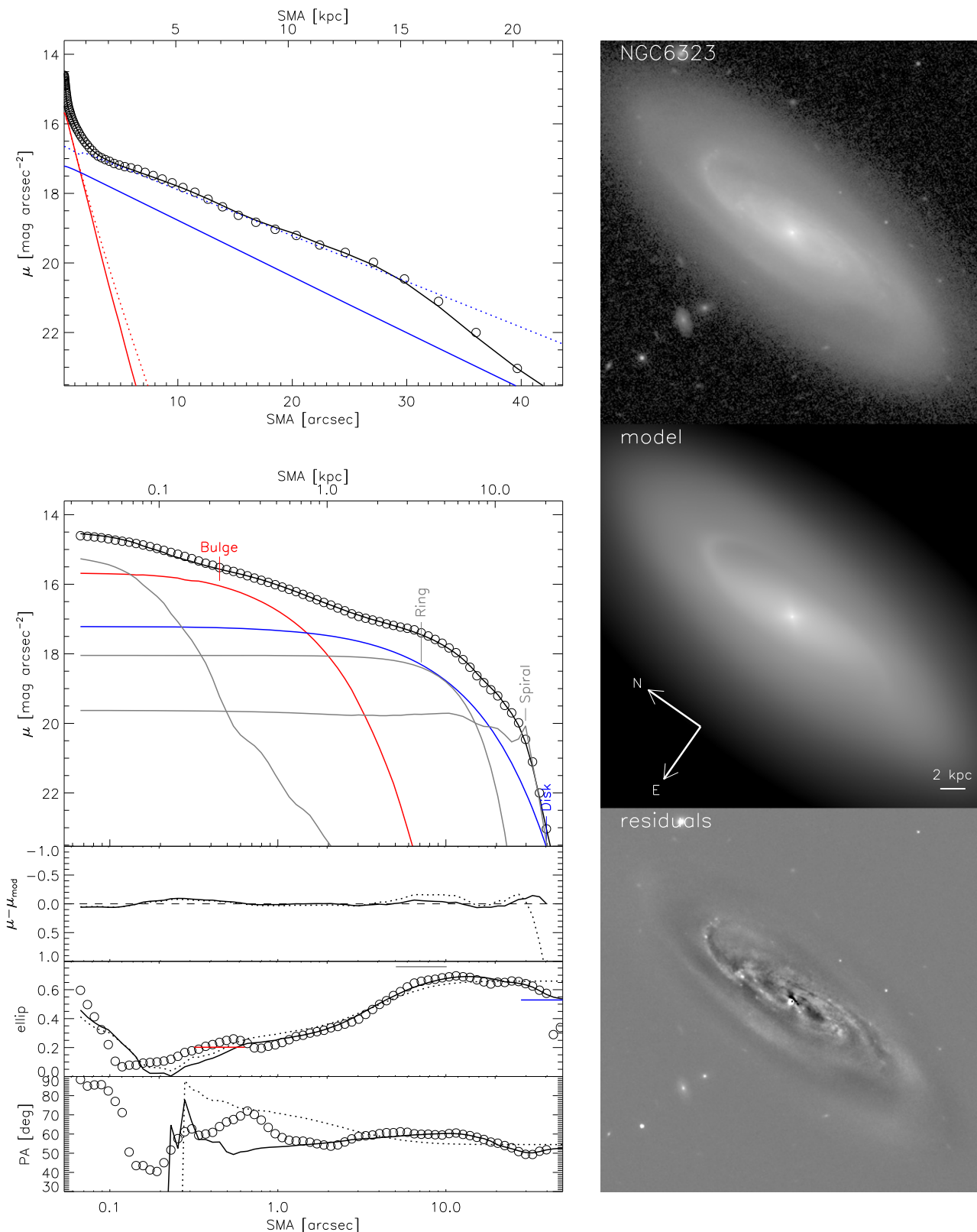
Figure 23. NGC 6323 photometric data and model, with layout as in Figure 9. Left panels: semimajor-axis (SMA) profiles of *H*-band surface brightness (μ), data-model residuals ($\mu-\mu_{mod}$), ellipticity (ellip), and east-of-north position angle (PA). Open circles: data, solid lines: full model, dashed lines: basic (bulge+disk) model. Thick black: total model image profiles, red: bulge, blue: disk, and thin gray: all other components. Only select profiles are shown in the μ–SMA (top panel) and μ–log SMA (second from top) plots (see also Figure 24). Ellipticities of individual components are indicated by horizontal bars. Right panels: Images of the data, model and residuals. The overall structure is simple, dominated by the disk and a clear profile steepening (bulge) in the center. However, spiral arms and varying PA in the inner ~ kpc are also evident, The spiral arms are not strong or sharply defined in the *H*-band; we model them nevertheless by an exponential profile, modified by coordinate rotation and an inner truncation. They appear to emerge from an elongated structure that nearly forms a ring, which likely delineates an inner disk (a putative pseudobulge), but possibly also represents a bar. We model this structure separately by a Sérsic component (best-fit axis ratio $q \sim 0.2$ and $n \sim 0.4$) and thus distinguish it from the very round ($q \sim 0.8$) small ($R_e \sim 0.7$ kpc) classical bulge, for which we allowed a 4th-order isophotal harmonic to account for its boxiness.

Figure 24. NGC 6323 photometric data and model, continued from Figure 23. Left panel: SMA surface brightness (μ) of the data (open circles), full model (solid lines) and basic bulge+disk model (dashed), separately for total light (black), bulge (red) and disk (blue). Right panel: image of basic model residuals, which highlight the spiral arms as well as the inner disk (or bar) from which the spiral arms emerge.

structure remains in the residual image, including spiral arms and a ring from which they appear to emerge, as well as a central misaligned, elongated structure whose ends coincide with the ring. We therefore construct a model that includes a spiral component modified by coordinate rotation and inner truncation, as well as a very compact, low-n Sérsic profile with high flattening that accounts for light between the bulge and the spiral arms and may be interpreted as a large-scale bar. This additional component also effectively removes the ring-like residuals at the onset of the spiral structure. Coincidentally, despite the addition of two components, the best-fit bulge parameters of the reference model are only marginally different from that of the basic model ($m_{\rm bul} = 15.5$ mag instead of 15.4 mag, and similarly for the bulge R_e and n). The bulge is about 2 mag fainter than the disk, $R_e = 1\farcs3$ (0.65 kpc) in size, and has a near-exponential profile. Allowing a fourth-order Fourier mode for the bulge isophotes gives a boxy shape (amplitude $\sim$0.1). The spiral is modified by Fourier modes (fourth order and lower), which enables fitting of the asymmetry in the spiral arms and a better convergence of the rotation function.

We explore multiple alternative models and find that, while formally increasing residuals (χ^2), for some of them the residual images and radial profile mismatches differ only in details. Removing the bar/ring component decreases the bulge brightness by 0.2 mag, and omitting the spiral arm component instead changes $m_{\rm bul}$ by less then 0.1 mag. Testing a model where the disk has a Sérsic profile instead of an exponential gives a 0.2 mag brighter bulge and a disk Sérsic index of 0.9. The lowest change in residuals, but biggest change in $m_{\rm bul}$, occurs when we apply a truncation to the bar/ring instead of the spiral arm component, obtaining a 1 mag brighter and three times larger bulge, with $n = 3.0$ instead of 1.1. Taken together,

these alternatives indicate a systematic $m_{\rm bul}$ uncertainty of 0.5 mag.

A.9. UGC 3789

UGC 3789 (Figures 25 and 26) is a late-type galaxy that is seen nearly face on and dominated by two rings, one close to the center at SMA $= 3\farcs8$ (900 pc), and the second one at SMA $= 23''$ (5.6 kpc). Both rings contain star-forming regions and form the boundary of a disk, respectively, but the larger ring, as in NGC 3393, might as well delineate a large-scale bar. The inner ring is nearly round, while the second ring shows marked flattening and asymmetry. Two short spiral arms emerge at a PA $\approx 170°$ but varies by several degrees from the center outwards. A third, weaker ring is discernible in the μ profile at $\sim$40$''$ (10 kpc) and marks the edge of the visible large-scale disk.

A basic bulge+disk+AGN model is clearly unsuitable to model this galaxy due to the luminous rings and bar. The "bulge" component fitted by the basic model largely fits the inner ring and is therefore very compact ($n \sim 1$). The "disk" in the basic model roughly accounts for the light of the second ring. In our best-fit model, the rings are modeled by Gaussian profiles with inner truncation, except for the outermost (third) ring, which is an untruncated Sérsic profile with low index $\sim$0.1 in the best-fit solution. Finally, the bar component becomes readily fit by a typical geometry ($q \sim 0.3$) and compact profile ($n \sim 0.3$).

The resulting reference model is a vast improvement over the basic model in terms of residuals and interpretation. Coincidentally, the bulge magnitude is almost identical to that of the basic model, but the bulge $R_e = 3''/700$ pc and $n = 3.3$ are $\sim$50% and 300% larger, respectively. Fitting the outer ring proves essential to keep the size of the main disk from growing extremely large. The truncation of the two inner rings improve
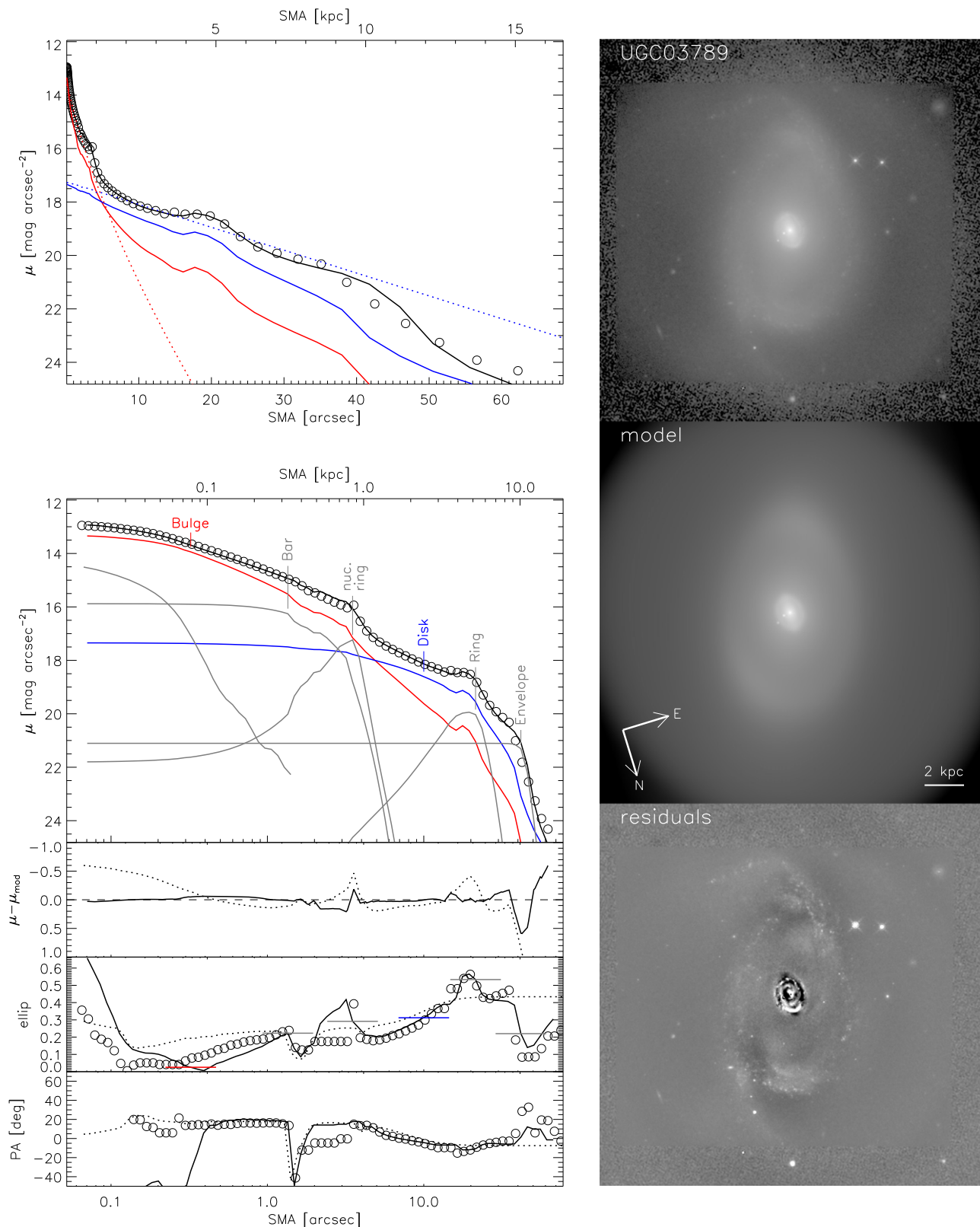
Figure 25. UGC 3789 photometric data and model, with layout as in Figure 9. Left panels: semimajor-axis (SMA) profiles of *H*-band surface brightness (μ), data-model residuals ($\mu-\mu_{mod}$), ellipticity (ellip), and east-of-north position angle (PA). Open circles: data, solid lines: full model, dashed lines: basic (bulge+disk) model. Thick black: total model image profiles, red: bulge, blue: disk, and thin gray: all other components. Only select profiles are shown in the μ–SMA (top panel) and μ–log SMA (second from top) plots (see also Figure 26). Ellipticities of individual components are indicated by horizontal bars. Right panels: Images of the data, model and residuals. The structure of UGC 3789 is similar to NGC 3998, with a large-scale round outer disk on which faint and weakly defined spiral arms and star-forming regions are superposed, a bright large elongated inner disk (or bar) delineated by a bright star-forming ring, and a round nuclear disk/ring with an inset nuclear bar. We model the bar by a Sérsic profile (best fit $n \sim 0.3$), and the rings with Gaussian profiles with an inner truncation (dropping the truncation for the outer ring due to excessive degeneracy). The best-fit model reproduces the profiles accurately compared to the basic model, especially in terms of the steep central ($\lesssim$100 pc) brightness and variations in the ellipticity.
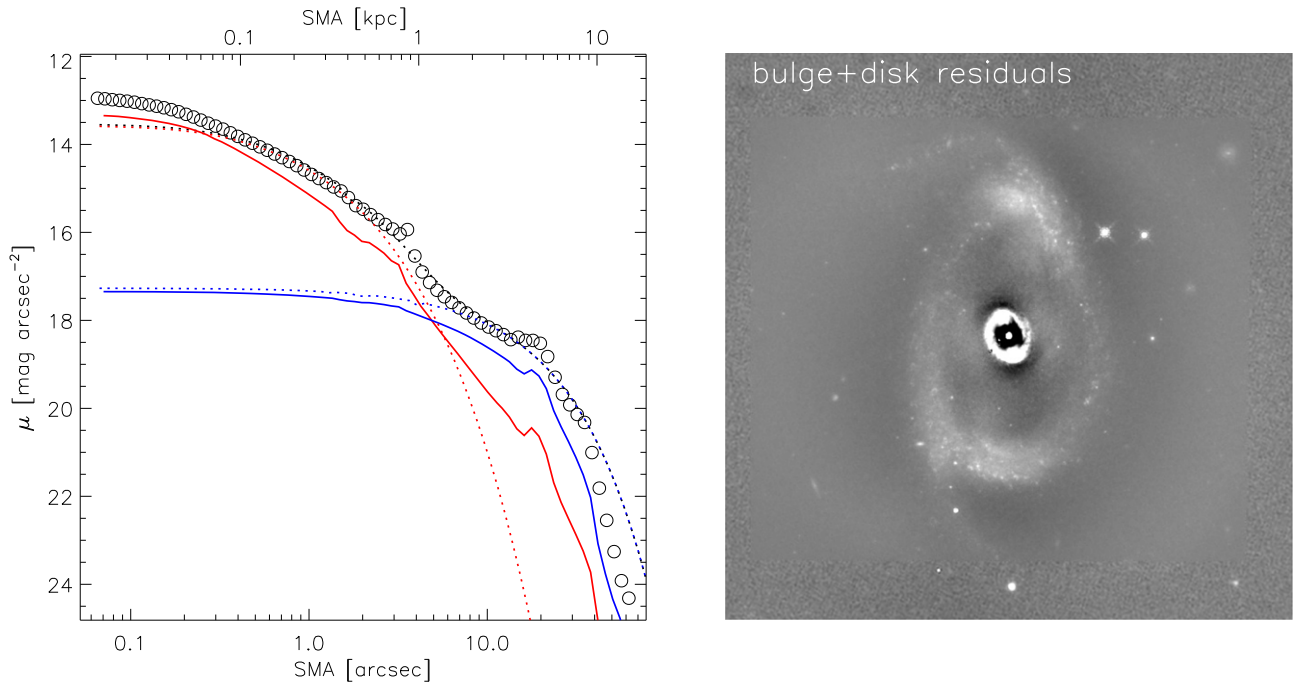
Figure 26. UGC 3789 photometric data and model, continued from Figure 25. Left panel: SMA surface brightness (μ) of the data (open circles), full model (solid lines) and basic bulge+disk model (dashed), separately for total light (black), bulge (red) and disk (blue). Right panel: image of basic model residuals, which exposes the intermediate elongated ring (extending about half the way to the edge of the shown image), as well as the nuclear ring and bar. The basic model bulge is biased by this nuclear ring and bar to a too compact profile, which we avoid in the full model by separate nuclear bar and ring components. The basic model also renders an overprediction for the disk (and hence the total) luminosity due to the influence of the kiloparsec-scale bar/ring that is included as a component in the full model as well.
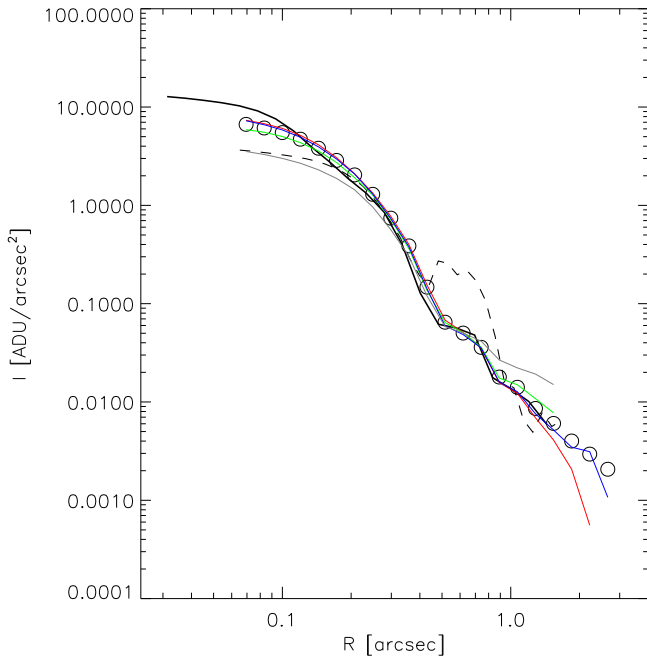
Figure 27. Comparison of our empirical PSF (open circles) with the analytic TinyTim-based profile (dashed curve). The two are quite different in the center and around $0\rlap{.}''5$, and the analytic version causes significant mismatch with observed stars and bright galaxy centers. The profiles of individual stars used to construct the PSF image (thin colored curves) agree well with their sum and with one another, indicating that broadening by centering errors, residual background, contamination, and saturation are minimal. Confirmation of the accuracy of our empirical PSF also comes from comparing it with an independent derivation by the CANDELS collaboration (solid thick black curve), which albeit used upsampling before co-addition (to $0\rlap{.}''06$), and therefore probes closer to the PSF center.

the residuals considerably and allow bulge and disk to account for the central and inter-ring light. The following models are less precise representations of the data, but are still superior to the simple model and acceptable alternatives. When removing the outer ring, or the truncation of the second ring, the classical bulge magnitude differs by -0.8 mag ($+0.2$ mag) from the reference model, respectively. Removing the truncation of the inner ring increases the residuals, but leaves M_{bul} nearly unchanged. Finally, we note that using a Sérsic profile for the main disk also leads to a very similar overall model, as the Sérsic index of the disk is $0.8 \approx 1$ in the best fit. On average, these alternatives provide for a systematic uncertainty estimate of the bulge magnitude of 0.4 mag.

APPENDIX B
ANCILLARY INFORMATION ON GALFIT IMAGE MODELING

B.1. Providing an Accurate PSF

In order to account for the effects of the PSF, GALFIT convolves each model with a PSF image. A scaled version of the PSF image is also used as a model of a point source (an AGN in our case). The accuracy of the PSF image effects the fit results of small-scale components near the galaxy center, including the bulge, and could in principle be important here. A PSF model can be provided by detailed modeling of the optical path and detector properties, as is commonly done for *HST* images. However, we found that the PSF that we obtained from TinyTim (Krist et al. 2010) is not adequate to describe the SB distribution of stars that we observe on our target fields. The problem is large enough to leave characteristic ring-like residuals near the galaxy centers after modeling, and to notably

impact the AGN magnitude and bulge parameters in some of our targets. We therefore empirically derive the PSF using cutout images of non-saturated and isolated stars found on our (co-added) science frames. The co-addition of several such star cutouts improves the S/N and reduces the residual background uncertainty. It has the drawback of potentially broadening the PSF profile near the center due to finite pixel sampling and an unavoidable centering error (we do not resample onto fractional pixels). We tested the broadening incurred in our co-added image and find it to be marginal (see Figure 27).

The PSF image must be large compared to the PSF FWHM to include most of the PSF image flux. We use a 43x43 pixel common cutout area, which is ~27 times the FWHM of $0\rlap{.}''2$ that we measure. Thus, our PSF image includes nearly 100% of the total PSF flux.

B.2. The Sigma Image

An image of the standard deviation of the flux per pixel (noise, or "sigma") is required to compute χ^2. Providing a realistic estimate of the sigma map is necessary to obtain the "true" best-fit solution of a given model. We obtain the sigma image by first computing it on the ground-based and *HST* image stacks separately. This consists of measuring the background noise across the image as a whole (with objects masked) for the ground-based images, and adding in quadrature the Poisson noise from the object flux using the flux itself and the local effective gain. For the *HST* stacks, the noise can be computed since the four exposures are weighted evenly and all background levels are known precisely. Afterward, the two images are scaled and combined, with the *HST* data replacing ground-based data wherever it is available, and the noise maps are scaled accordingly.

B.3. Object Masks

Since we want to model the galaxy light unbiased by foreground and background objects, masks for the latter are indispensable. We create masks based on automatic object detection by SExtractor. We subsequently add masks by hand for stars that are particularly bright, and thus have extended PSF wings, or those that overlap with the galaxy and are hence not recognized by the automatic detection. In one case (UGC 3789), we opt not to mask the two stars near the galaxy center, but include them in our model and thereby avoid masking much of the area containing important constraints on the central profile. None of our fields are particularly crowded.

REFERENCES

Andredakis, Y. C., & Sanders, R. H. 1994, MNRAS, 267, 283
Barbosa, F. K. B., Storchi-Bergmann, T., Cid Fernandes, R., Winge, C., & Schmitt, H. 2006, MNRAS, 371, 170
Batcheldor, D. 2010, ApJL, 711, L108
Beifiori, A., Courteau, S., Corsini, E. M., & Zhu, Y. 2012, MNRAS, 419, 2497
Bell, E. F., McIntosh, D. H., Katz, N., & Weinberg, M. D. 2003, ApJS, 149, 289
Bell, E. F., van der Wel, A., Papovich, C., et al. 2012, ApJ, 753, 167
Bennert, V. N., Auger, M. W., Treu, T., Woo, J.-H., & Malkan, M. A. 2011, ApJ, 742, 107
Bennert, V. N., Treu, T., Woo, J.-H., et al. 2010, ApJ, 708, 1507
Bentz, M. C., Peterson, B. M., Netzer, H., Pogge, R. W., & Vestergaard, M. 2009a, ApJ, 697, 160
Bentz, M. C., Peterson, B. M., Pogge, R. W., & Vestergaard, M. 2009b, ApJL, 694, L166

Blanton, M. R., Kazin, E., Muna, D., Weaver, B. A., & Price-Whelan, A. 2011, AJ, 142, 31
Braatz, J. A., Reid, M. J., Humphreys, E. M. L., et al. 2010, ApJ, 718, 657
Cappellari, M. 2013, ApJL, 778, L2
Carollo, C. M. 1999, ApJ, 523, 566
Carollo, C. M., Stiavelli, M., de Zeeuw, P. T., & Mack, J. 1997, AJ, 114, 2366
Cisternas, M., Jahnke, K., Bongiorno, A., et al. 2011, ApJL, 741, L11
Conroy, C., Gunn, J. E., & White, M. 2009, ApJ, 699, 486
Davis, T. A. 2014, MNRAS, 443, 911
de Vaucouleurs, G., de Vaucouleurs, A., Corwin, H. G., Jr., et al. 1991, Third Reference Catalogue of Bright Galaxies, Vol. I, II, III (New York: Springer)
Debuhr, J., Quataert, E., Ma, C.-P., & Hopkins, P. 2010, MNRAS, 406, L55
den Brok, M., Seth, A. C., Barth, A. J., et al. 2015, arXiv:1507.04358
Djorgovski, S., & Davis, M. 1987, ApJ, 313, 59
Do, T., Wright, S. A., Barth, A. J., et al. 2014, AJ, 147, 93
Dressler, A., Lynden-Bell, D., Burstein, D., et al. 1987, ApJ, 313, 42
Erwin, P., Beckman, J. E., & Pohlen, M. 2005, ApJL, 626, L81
Erwin, P., Beltrán, J. C. V., Graham, A. W., & Beckman, J. E. 2003, ApJ, 597, 929
Erwin, P., Pohlen, M., & Beckman, J. E. 2008, AJ, 135, 20
Erwin, P., Saglia, R. P., Fabricius, M., et al. 2015, MNRAS, 446, 4039
Erwin, P., & Sparke, L. S. 2003, ApJS, 146, 299
Fabian, A. C. 2012, ARA&A, 50, 455
Falcón-Barroso, J., Bacon, R., Bureau, M., et al. 2006, MNRAS, 369, 529
Ferrarese, L., & Ford, H. 2005, SSRv, 116, 523
Fisher, D. B., & Drory, N. 2010, ApJ, 716, 942
Fukugita, M., Ichikawa, T., Gunn, J. E., et al. 1996, AJ, 111, 1748
Gadotti, D. A. 2008, MNRAS, 384, 420
Gadotti, D. A. 2009, MNRAS, 393, 1531
Gao, F., Braatz, J. A., Reid, M. J., et al. 2015, arXiv:1511.08311
Ghez, A. M., Salim, S., Weinberg, N. N., et al. 2008, ApJ, 689, 1044
Gillessen, S., Eisenhauer, F., Trippe, S., et al. 2009, ApJ, 692, 1075
Graham, A. W., & Driver, S. P. 2007, ApJ, 655, 77
Graham, A. W., & Scott, N. 2015, ApJ, 798, 54
Greene, J. E., Ho, L. C., & Barth, A. J. 2008, ApJ, 688, 159
Greene, J. E., Peng, C. Y., Kim, M., et al. 2010, ApJ, 721, 26
Greene, J. E., Seth, A., den Brok, M., et al. 2013, ApJ, 771, 121
Greene, J. E., Seth, A., Lyubenova, M., et al. 2014, ApJ, 788, 145
Greenhill, L. J., Booth, R. S., Ellingsen, S. P., et al. 2003, ApJ, 590, 162
Greenhill, L. J., Gwinn, C. R., Antonucci, R., & Barvainis, R. 1996, ApJL, 472, L21
Gu, Q.-S., Shi, L., Lei, S.-J., Liu, W.-H., & Huang, J.-H. 2003, ChJAA, 3, 203
Gültekin, K., Tremaine, S., Loeb, A., & Richstone, D. O. 2011, ApJ, 738, 17
Häring, N., & Rix, H.-W. 2004, ApJL, 604, L89
Herrnstein, J. R., Moran, J. M., Greenhill, L. J., et al. 1999, Natur, 400, 539
Herrnstein, J. R., Moran, J. M., Greenhill, L. J., & Trotter, A. S. 2005, ApJ, 629, 719
Hu, J. 2008, MNRAS, 386, 2242
Humphreys, E. M. L., Reid, M. J., Moran, J. M., Greenhill, L. J., & Argon, A. L. 2013, ApJ, 775, 13
Jahnke, K., Bongiorno, A., Brusa, M., et al. 2009, ApJL, 706, L215
Jahnke, K., & Macciò, A. V. 2011, ApJ, 734, 92
Kelly, B. C. 2007, ApJ, 665, 1489
Khosroshahi, H. G., Wadadekar, Y., Kembhavi, A., & Mobasher, B. 2000, ApJL, 531, L103
Kondratko, P. T., Greenhill, L. J., & Moran, J. M. 2008, ApJ, 678, 87
Kormendy, J. 1977, ApJ, 218, 333
Kormendy, J., Bender, R., & Cornell, M. E. 2011, Natur, 469, 374
Kormendy, J., & Ho, L. C. 2013, ARA&A, 51, 511
Kormendy, J., & Kennicutt, R. C., Jr. 2004, ARA&A, 42, 603
Kriek, M., Labbé, I., Conroy, C., et al. 2010, ApJL, 722, L64
Krist, J., Hook, R., & Stoehr, F. 2010, Tiny Tim: Simulated Hubble Space Telescope PSFs, Astrophysics Source Code Library, ascl:1010.057
Kuo, C. Y., Braatz, J. A., Condon, J. J., et al. 2011, ApJ, 727, 20
Kuo, C. Y., Braatz, J. A., Lo, K. Y., et al. 2015, ApJ, 800, 26
Kuo, C. Y., Braatz, J. A., Reid, M. J., et al. 2013, ApJ, 767, 155
Lackner, C. N., & Gunn, J. E. 2012, MNRAS, 421, 2277
Läsker, R., Ferrarese, L., & van de Ven, G. 2014a, ApJ, 780, 69
Läsker, R., Ferrarese, L., van de Ven, G., & Shankar, F. 2014b, ApJ, 780, 70
Laurikainen, E., Salo, H., Buta, R., Knapen, J. H., & Comerón, S. 2010, MNRAS, 405, 1089
Lo, K. Y. 2005, ARA&A, 43, 625
Lodato, G., & Bertin, G. 2003, A&A, 398, 517
MacArthur, L. A., Courteau, S., & Holtzman, J. A. 2003, ApJ, 582, 689
Maraston, C. 2005, MNRAS, 362, 799
Marconi, A., & Hunt, L. K. 2003, ApJL, 589, L21

Marigo, P., Girardi, L., Bressan, A., et al. 2008, A&A, 482, 883

Martín-Navarro, I., Barbera, F. L., Vazdekis, A., Falcón-Barroso, J., & Ferreras, I. 2015, MNRAS, 447, 1033

Martini, P., & Weinberg, D. H. 2001, ApJ, 547, 12

McConnell, N. J., Chen, S.-F. S., Ma, C.-P., et al. 2013, ApJL, 768, L21

McConnell, N. J., & Ma, C.-P. 2013, ApJ, 764, 184

Menéndez-Delmestre, K., Sheth, K., Schinnerer, E., Jarrett, T. H., & Scoville, N. Z. 2007, ApJ, 657, 790

Miyoshi, M., Moran, J., Herrnstein, J., et al. 1995, Natur, 373, 127

Mulchaey, J. S., Regan, M. W., & Kundu, A. 1997, ApJS, 110, 299

Nowak, N., Thomas, J., Erwin, P., et al. 2010, MNRAS, 403, 646

Oke, J. B., & Gunn, J. E. 1983, ApJ, 266, 713

Peng, C. Y. 2007, ApJ, 671, 1098

Peng, C. Y., Ho, L. C., Impey, C. D., & Rix, H.-W. 2010, AJ, 139, 2097

Petitpas, G. R., & Wilson, C. D. 2002, ApJ, 575, 814

Pohlen, M., & Trujillo, I. 2006, A&A, 454, 759

Ravindranath, S., Ho, L. C., Peng, C. Y., Filippenko, A. V., & Sargent, W. L. W. 2001, AJ, 122, 653

Reid, M. J., Braatz, J. A., Condon, J. J., et al. 2009, ApJ, 695, 287

Reid, M. J., Braatz, J. A., Condon, J. J., et al. 2013, ApJ, 767, 154

Reines, A. E., & Volonteri, M. 2015, ApJ, 813, 82

Roediger, J. C., & Courteau, S. 2015, arXiv:1507.03016

Saglia, R. P., Opitsch, M., Erwin, P., et al. 2016, arXiv:1601.00974

Sani, E., Marconi, A., Hunt, L. K., & Risaliti, G. 2011, MNRAS, 413, 1479

Schlafly, E. F., & Finkbeiner, D. P. 2011, ApJ, 737, 103

Sérsic, J. L. 1963, BAAA, 6, 41

Seth, A. C., Cappellari, M., Neumayer, N., et al. 2010, ApJ, 714, 713

Seth, A. C., van den Bosch, R., Mieske, S., et al. 2014, Natur, 513, 398

Silk, J., & Rees, M. J. 1998, A&A, 331, L1

Simien, F., & de Vaucouleurs, G. 1986, ApJ, 302, 564

Smee, S. A., Barkhouser, R. H., Scharfstein, G. A., et al. 2011, PASP, 123, 87

Springel, V., Di Matteo, T., & Hernquist, L. 2005, MNRAS, 361, 776

Sun, A.-L., Greene, J. E., Impellizzeri, C. M. V., et al. 2013, ApJ, 778, 47

van den Bosch, R. C. E., & de Zeeuw, P. T. 2010, MNRAS, 401, 1770

van den Bosch, R. C. E., Gebhardt, K., Gültekin, K., et al. 2012, Natur, 491, 729

van den Bosch, R. C. E., Gebhardt, K., Gültekin, K., Yıldırım, A., & Walsh, J. L. 2015, ApJS, 218, 10

van den Bosch, R. C. E., Greene, J. E., Braatz, J. A., Constantin, A., & Kuo, C.-Y. 2016, arXiv:1601.00645

Veilleux, S., Bland-Hawthorn, J., & Cecil, G. 1999, AJ, 118, 2108

Vika, M., Driver, S. P., Cameron, E., Kelvin, L., & Robotham, A. 2012, MNRAS, 419, 2264

Walsh, J. L., van den Bosch, R. C. E., Barth, A. J., & Sarzi, M. 2012, ApJ, 753, 79

Walsh, J. L., van den Bosch, R. C. E., Gebhardt, K., et al. 2015, ApJ, 808, 183

Walsh, J. L., van den Bosch, R. C. E., Gebhardt, K., et al. 2016, ApJ, 817, 2

Weinzirl, T., Jogee, S., Khochfar, S., Burkert, A., & Kormendy, J. 2009, ApJ, 696, 411

Woo, J.-H., Treu, T., Barth, A. J., et al. 2010, ApJ, 716, 269

Yamauchi, A., Nakai, N., Ishihara, Y., Diamond, P., & Sato, N. 2012, PASJ, 64, 103

York, D. G., Adelman, J., Anderson, J. E., Jr., et al. 2000, AJ, 120, 1579

Zibetti, S., Charlot, S., & Rix, H.-W. 2009, MNRAS, 400, 1181

Zibetti, S., Gallazzi, A., Charlot, S., Pierini, D., & Pasquali, A. 2013, MNRAS, 428, 1479